University of Central Florida
STARS

Electronic Theses and Dissertations, 2004-2019

2006

Experimental Techniques For Nonlinear Material Characterization: A Nonlinear Spectrometer Using A White-light Continuum Z-scan

Mihaela Balu
University of Central Florida

Part of the Electromagnetics and Photonics Commons, and the Optics Commons
Find similar works at: https://stars.library.ucf.edu/etd
University of Central Florida Libraries http://library.ucf.edu

This Doctoral Dissertation (Open Access) is brought to you for free and open access by STARS. It has been accepted for inclusion in Electronic Theses and Dissertations, 2004-2019 by an authorized administrator of STARS. For more information, please contact STARS@ucf.edu.

STARS Citation
Balu, Mihaela, "Experimental Techniques For Nonlinear Material Characterization: A Nonlinear Spectrometer Using A White-light Continuum Z-scan" (2006). *Electronic Theses and Dissertations, 2004-2019*. 937.
https://stars.library.ucf.edu/etd/937

EXPERIMENTAL TECHNIQUES FOR NONLINEAR MATERIAL CHARACTERIZATION: A NONLINEAR SPECTROMETER USING A WHITE-LIGHT CONTINUUM Z-SCAN

by

MIHAELA BALU
B.S. University of Bucharest, 1999

A dissertation submitted in partial fulfillment of the requirements
for the degree of Doctor of Philosophy
in the College of Optics and Photonics: CREOL & FPCE
at the University of Central Florida
Orlando, Florida

Summer Term
2006

Major Professors: Eric W. Van Stryland and David J. Hagan

© 2006 Mihaela Balu

ABSTRACT

The main goal of this dissertation is to introduce and demonstrate a new method for the rapid determination of the nonlinear absorption spectra and the dispersion of the nonlinear refraction of optical materials in the visible and near IR spectral regions. However, conventional methods like, white-light continuum pump-probe and Z-scan techniques were used to measure the peak 2PA cross-sections for a number of commercially available photoinitiators.

In the new method mentioned above, a high energy, broadband femtosecond white-light continuum is used to replace the single wavelength source conventionally used in a Z-scan experiment. In a Z-scan experiment, the transmittance of a focused beam through a sample is monitored as the sample travels through the focus, in the Z direction, along the focused beam. Providing the sample exhibits nonlinear absorption and/or refraction, the detector monitors a change in transmittance and/or a change in the beam divergence (if the energy is partially collected through an aperture in front of the detector). Replacing the single wavelength source with a white-light continuum allows for a much faster way of measuring nonlinear absorption/refraction spectra. This could eliminate the need for using other tunable sources (e.g. Optical Parameter Generators/Amplifiers) for nonlinear measurements. These sources made nonlinear spectroscopy using Z-scan experiments a time consuming task. This new source/method allows for rapid and simultaneous measurement of the nonlinear absorption spectrum and the dispersion of the nonlinear refraction.

We have confirmed the functionality of the continuum as a source for nonlinear optical characterization of materials by using it to perform Z-scans on the well characterized semiconductors ZnSe and ZnS and on solutions of organic dyes.

This dissertation is dedicated to my parents and my brother from thousands of miles away

ACKNOWLEDGMENTS

I feel very fortunate I had the opportunity to work as a graduate student in Dr. Eric Van Stryland's and Dr. David Hagan's group. I sincerely thank them for their guidance and for their effort to find time to advise me every time I needed, despite their very busy schedule.

It was a great pleasure to work with my colleagues, graduate and post-doctoral students in the NLO group. I would like to mention first, "the old generation": Raluca, Eloy, Joel, Rich, Will, Vinay. Raluca, who is now a dear friend of mine, gave me the first insights in the lab and I thank her very much. My special thanks go to Joel Hales from whom I learned a lot. His way of explaining complicated concepts in an understandable manner is remarkable. It was him who helped me with my first WLC Z-scan experiment and who encouraged me all these years when I had doubts that it was going to work. Thank you, Joel! Thank you, Rich, for the helpful discussions and for your support, especially when I was going through my toughest period of time during my PhD. Thank you, Eloy, for your interest and encouragements regarding the topic of this work. Thank you all for being good friends.

From the "new generation" my special thanks go to Claudiu who was a great partner for scientific discussions. Very enjoyable and helpful discussions, thank you!

Many thanks to all my fellow graduate students I have worked with during my PhD.

My graduation would have happened months later without Richard Zotti's ability to do his work in the Machine Shop, well and quick. Thank you very much for being so patient with

my tones of requests and for your effort to get things done for me as I would have needed them yesterday.

Thanks to the entire faculty, staff and students at CREOL who make this place a great environment to work in. I am sure I will miss it a lot.

Finally, I would like to thank all my friends and my family, especially my brother who encouraged me into this journey. Their continuous love and support always gave me strength to go through.

TABLE OF CONTENTS

LIST OF FIGURES x

LIST OF TABLES xv

LIST OF ACRONYMS/ABBREVIATIONS xvi

CHAPTER 1 : INTRODUCTION 1

1.1. Background and Motivation 1

1.2. Dissertation Outline 3

CHAPTER 2 : THIRD-ORDER NONLINEARITIES 5

2.1. Introduction 5

2.2. Non-Degenerate Third-Order NLA and NLR 8

2.3. Degenerate Third-Order NLA and NLR 16

CHAPTER 3 : LASER SYSTEM AND PARAMETRIC DEVICES FOR NONLINEAR MATERIAL CHARACTERIZATION 22

3.1. Ti:Sapphire Regeneratively Amplified Laser System 22

3.2. Optical Parametric Generator/Amplifier (OPG/OPA) Systems 28

CHAPTER 4 : Z-SCAN AND PUMP-PROBE TECHNIQUES FOR NONLINEAR MATERIAL CHARACTERIZATION 31

4.1. Single Wavelength Z-Scan for Measuring Degenerate Nonlinearities 31

4.2. White-Light Continuum Pump-Probe for Measuring Non-Degenerate Nonlinearities 43

4.3. 2PA Measurements of Common Photoinitiators 45

CHAPTER 5 : NEW TECHNIQUE FOR NONLINEAR MATERIAL CHARACTERIATION: WHITE-LIGHT CONTINUUM Z-SCAN 52

5.1. Motivation and Important Issues Regarding the Technique 52

5.1.1. WLC generation in condensed media (solids and liquids) 54

5.1.2. WLC generation in hollow fiber filled with noble gases 56

5.1.3. WLC generation in gases (no guiding element) 60

5.2. Experiments 62

5.2.1. WLC Z-scan using WLC generated in distilled water 62

5.2.1.1 Spatial and Temporal Separation of the WLC wavelengths 68

5.2.1.2 Spectral Separation of the WLC wavelengths 73

5.2.2. WLC Z-scan using WLC generated in hollow fiber filled with noble gases 80

5.2.3. WLC Z-scan using WLC generated in noble gases 89

CHAPTER 6 : CONCLUSION 103

6.1. Summary 103

6.2. Future Work 105

LIST OF REFERENCES 107

LIST OF FIGURES

Figure 3-1::Regenerative amplifier cavity. M-mirror; BS-beamsplitter; FR-Faraday rotator; PC-Pockel cell 24

Figure 3-2: Absorption and emission spectra of titanium:sapphire laser amplifier rod 26

Figure 3-3: Far field spatial profile of the 775nm output of the Ti:Sapphire regeneratively amplified system 26

Figure 3-4: Temporal characterization of 775nm output beam of the Ti:Sapphire regeneratively amplified system 27

Figure 3-5: Top view of the TOPAS layout; A-aperture; BS-beamsplitter-L-lens; M-mirror; CL-cylindrical lens; CM-cylindrical mirror; NC-nonlinear crystal; DG-diffraction grating; GP-fused silica plate; TD-time delay; PR-polarization rotator 29

Figure 4-1: Typical 2PA ("open aperture" Z-scan) curve 36

Figure 4-2: Typical NLR ("closed aperture" Z-scan) curves corresponding to a) positive and b) negative nonlinearity 38

Figure 4-3: "Closed aperture" Z-scan curves including 2PA and NLR corresponding to a) positive and b) negative nonlinearity 40

Figure 4-4: Single Wavelength Z-scan Experimental Set-up: L-lens; BS-beamsplitter; A-aperture; D-detector 41

Figure 4-5: WLC Pump-Probe Set-up: M-mirror; L-lens; A-aperture; P-polarizer; PR-polarization rotator; RR-retro-reflector; NBF-dielectric short pass filter for blocking any remaining 1300 nm radiation 44

Figure 4-6: (left) Normalized UV-visible absorption spectra of Irgacure series photoinitiators in MeOH. (right) Normalized UV-visible absorption spectra of the Darocure and CGI series, CD1012, and ITX in MeOH. DPABz shown is in THF. 47

Figure 4-7: 2PA spectra via the WLC method. ITX spectrum has been enlarged (5x) for ease of viewing. Solid lines indicate UV-visible linear absorption spectra for the corresponding compounds. 48

Figure 4-8: 2PA results via the Z-scan method for stationary cell and flow cell geometries. (a) CGI 124. (b) Irgacure 369 51

Figure 5-1: WLC spectrum after passing through the low-pass filter 63

Figure 5-2: WLC Z-scan experimental setup. CPA-2001-femtosecond source; WP-waveplate; P-polarizer; L-lens; GP-glass prism; M-mirror; NBF-narrow band filter; BS-beamsplitter; S-sample; D-detector. A and B denote the positions of additional elements inserted in the set-up. NBF(SW) is used only in the single wavelength configuration discussed in the text with the other two NBF's removed 65

Figure 5-3: Normalized Z-scan transmittances of ZnSe measured at 650nm for a) the WLC configuration and b) the SW configuration. The solid lines represent fittings used to extract β values 67

Figure 5-4: Normalized Z-scan transmittance of ZnSe measured at 670nm with the WLC beam temporally dispersed. The solid lines represent fittings used to extract β values a) WLC configuration, b) SW configuration 69

Figure 5-5: Normalized Z-scan transmittance of ZnSe measured at 670nm with the WLC beam temporally and spatially dispersed. The solid lines represent fittings used to extract β values a) WLC configuration, b) SW configuration 70

Figure 5-6: Normalized Z-scan transmittance of ZnSe measured at different wavelengths with the WLC beam temporally and spatially dispersed. The solid lines represent fittings used to extract β values. Z-scan traces are shifted from their original positions for an easier view 71

Figure 5-7: 2PA coefficient, β, values obtained from theory and from the experimental data fittings 72

Figure 5-8: a) low-pass filter spectra at different position along its length b) high pass filter spectra at different position along its length c) spectra obtained by fastening together a low-pass and high-pass filter taken at different position along its length 73

Figure 5-9: Linear variable filters manufactured by Ocean Optics 74

Figure 5-10: WLC Z-scan experimental setup. CPA-2001-femtosecond laser source; WP-waveplate; P-polarizer; L-lens; LVF-linear variable filter; M-mirror; BS-beamsplitter; S-sample; A-aperture; D-detector..... 75

Figure 5-11: Z-scan data at 580nm and 710nm a) open aperture and b) closed aperture (the result of the division with open aperture). Here each data point is the average of 500 pulses..... 78

Figure 5-12: a) 2PA coefficient and b) nonlinear refractive index coefficient obtained from theory and from the experimental data fittings 79

Figure 5-13: a) WLC generated in 10cm long BaF_2 crystal b) filaments generated by focusing 140 μJ, 775nm beam into the BaF_2 crystal 80

Figure 5-14: Thick wall capillary tubing made by Polymicro Technologies 81

Figure 5-15: a) Stainless steel chamber holding the hollow fiber; b) schematic representation of the hollow glass capillary tubing inside the chamber 81

Figure 5-16: Output spectrum from a hollow fiber filled with a) Ar and b) Kr 82

Figure 5-17: Experimental set-up for Z-scan using a WLC source: WP-waveplate; P-polarizer; A-aperture; L-lens; FW-filter wheel; S-sample; D-detector 84

Figure 5-18: Energies for different wavelengths in the continuum measured after the corresponding narrow band filter 85

Figure 5-19: Beam images and their Gaussian profiles measured by a CCD for different wavelengths 86

Figure 5-20: 2PA coefficients obtained from theory and from the experimental data fittings 86

Figure 5-21: 2PA cross-section spectrum for SD2577 compound obtained from WLC Z-scan experiment and comparison with spectra obtained from Single Wavelength Z-scan and 2PF experiments 87

Figure 5-22: 2PA cross-section spectrum for SJZ316 compound obtained from WLC Z-scan experiment and comparison with spectra obtained from 2PF experiments 88

Figure 5-23: Experimental configuration used for observing ring pattern in the beam profile of wavelengths in the continuum 90

Figure 5-24: Beam profiles corresponding to wavelengths in the continuum for different gases used in the pressurized chamber a) Xe (0.35 atm); b) Ar (5.4 atm); pressures quoted are above atmospheric pressure 91

Figure 5-25: Experimental configuration used for generating a stable, high energy, broadband, good beam profile WLC source 92

Figure 5-26: White-light continuum image 92

Figure 5-27: White-light continuum spectrum 93

Figure 5-28: The transmitted WLC beam through three different narrow band filters 94

Figure 5-29: Beam profiles corresponding to different wavelengths of the continuum 95

Figure 5-30: Pulsewidth measurements results for different wavelengths in the continuum transmitted by NBFs 96

Figure 5-31: WLC Z-scan experimental set-up: L-lens; M-mirror; WP-half-waveplale; P-polorizer; FW-filter wheel; BS-beamsplitter; D-detector; A-aperture; S-sample..... 97

Figure 5-32: Z-scan data at 480nm, 550nm, 750nm and 800nm a) open aperture and b) closed aperture (the result of the division with open aperture)..... 99

Figure 5-33: 2PA and n_2 coefficients of ZnSe obtained from theory and from the experimental data fitting 100

Figure 5-34: Z-scan data at 400nm, 570nm, 620nm, 670nm, 750nm and 800nm a) open aperture b) close aperture (the result of the division with open aperture). The last two graphs do not show open aperture curves as 2PA was not present at those particular wavelengths..... 101

Figure 5-35: 2PA and n_2 coefficients of ZnS obtained from theory and from the experimental data fitting 102

LIST OF TABLES

Table 4-1: Chemical structures of the photoinitiators..... 46

Table 4-2: Peak 2PA cross-sections for photoinitiators using Z-scan and WLC methods..... 49

LIST OF ACRONYMS/ABBREVIATIONS

2PA	Two-Photon Absorption
cm	Centimeter
ESA	Excited-State Absorption
eV	Electron-Volt unit of energy
fs	Femtosecond (10^{-15}s)
FW	Filter Wheel
FWHM	Full Width Half Maximum
GM	Goppert-Mayer unit for the 2PA cross-section
GVD	Group-Velocity Dispersion
kHz	Kilohertz (10^{3} Hz)
LVF	Linear Variable Filter
μJ	Microjoule (10^{-6} J)
μm	Micrometer (10^{-6} m)
NBF	Narrow Band Filter
nJ	Nanojoule (10^{-9} J)
nm	Nanometer (10^{-9}m)
NLA	Nonlinear Absorption
NLR	Nonlinear Refraction
OKG	Optical Kerr Gate
OPA	Optical Parametric Amplifier
OPG	Optical Parametric Generator

pJ	Picojoule (10^{-12} J)
ps	Picosecond (10^{-12} s)
SVEA	Slowly-Varying Amplitude Approximation
SW	Single Wavelength
WLC	White-Light Continuum

CHAPTER 1: INTRODUCTION

1.1. Background and Motivation

In this work, nonlinear optical properties of materials are determined by using either conventional techniques or by using a new technique which will be described (white-light continuum Z-scan, WLC Z-scan). Optical properties of materials are "nonlinear" in the sense that their response (polarization) to an applied optical field depends in a nonlinear manner upon the strength of the electric field. Typically, only laser light is sufficiently intense to nonlinearly modify the optical properties of a material system [1]. Therefore, experimental nonlinear optics needed to wait for the invention of the laser in 1960 [2] to start developing. In 1961, in the same volume of Physics Review Letters, *Franken et al*. published their observations on a 3471Å optical signal generated in a quartz crystal illuminated with a high-power ruby laser at 6942Å (second-harmonic generation) [3] and Kaiser and Garret published their experiments on degenerate (identical photon energies) two-photon absorption (2PA) induced fluorescence in a CaF_2:Eu^{2+} crystal [4]. Kaiser and Garret confirmed by their experiments, M. Göppert Mayer's prediction of 2PA in 1931 [5]. These works are often considered to be at the origin of nonlinear optics.

Although there exists a wide variety of nonlinear optical phenomena, we are interested mainly in nonlinear absorption (NLA) and its associated nonlinear refraction (NLR). NLA is any process by which light changes the optical absorptive properties of a material [6]. In particular, 2PA is the process by which a transition between two real states is made by the simultaneous absorption of two photons, not necessarily at the same frequency. It is associated with the

imaginary part of the third order susceptibility while the nonlinear refractive index is related to the real part of the third order susceptibility [1]. Details about these third-order nonlinear processes will be described in Chapter 2 of this dissertation.

2PA processes are exploited in applications such as two-photon fluorescence imaging [7,8], two-photon microfabrication [9,10] or 3D optical data storage [11]. Two photon absorbers are also needed for optical limiters used in sensor protection [12].

Nonlinear refraction is any process by which light changes the optical refractive properties of a material. Nonlinear refraction due to the bound electrons in materials has a subpicosecond response [13], therefore, the nonlinear refractive index is one of the important parameters for designing ultrafast all-optical switching devices which are expected to play an important role in modern optical communication systems where signals are transmitted at high speed and high-bit-rate [14]. For effective all-optical switches, low switching power is desired which requires a large nonlinear refractive index. Exploring materials which would give large intensity-dependent contributions to the refractive index has been a subject of interest in recent years [15, 16].

The aforementioned applications require nonlinear properties of materials to be known over a broad wavelength range. There are different methods for measuring nonlinearities. Among these, we use white-light continuum (WLC) pump–probe [17], a technique which uses a WLC as a weak probe of nonlinear absorption induced by a separate, strong, single wavelength excitation beam, thus yielding the frequency nondegenerate nonlinearities. However, knowledge of a material's degenerate nonlinearities is often needed for most of the above mentioned applications. We measure degenerate absorption and refraction using single wavelength Z-scan [18]. This is a simple, sensitive technique but obtaining a broad spectral dependence of the

nonlinearity requires wavelength tuning and realignment which are often time consuming processes. Sometimes, it is difficult to distinguish ultrafast nonlinearities such as 2PA, from cumulative nonlinearities of, for example, excited-state absorption (ESA); or to distinguish bound-electronic nonlinear refraction from free-carrier refraction. We need to develop a large and reliable database of nonlinear spectral properties of materials to be able to determine their structure-property trends. We introduce a method for very rapid and simultaneous determination of both the spectrum of the degenerate NLA and dispersion of NLR.

In this method, we replace the single wavelength source conventionally used in the Z-scan technique with an intense broadband WLC source. This method, which we refer to as WLC Z-scan, provides an absolute measurement of the degenerate nonlinearities of the sample under investigation and adds the sensitivity of the normal Z-scan technique as it will be described in Chapter 5 of this dissertation.

1.2. Dissertation Outline

Background information regarding third-order nonlinearities is introduced in Chapter 2. Degenerate and nondegenerate NLA and NLR, 2PA and its associated nonlinear refractive index are discussed in Chapter 2. The laser systems available in our lab and used for nonlinear material characterization are presented in Chapter 3. Chapter 4 describes the two techniques we use for nonlinear material characterization: WLC pump-probe and single wavelength Z-scan. We used these methods for 2PA measurements of several common photoinitiators (molecules which added to a monomer, start a photopolymerization process). The main purpose of this dissertation is to introduce and demonstrate the potential of the new method, WLC Z-scan for rapid

characterization of a material's degenerate nonlinear absorption spectrum and the dispersion of its nonlinear refraction. Chapter 5 introduces the WLC Z-scan. Discussion about different methods for WLC generation used as a source in the new technique and the experimental results confirming the validity of the WLC Z-scan are also presented in Chapter 5. Chapter 6 provides the conclusion of this work and discusses future directions.

CHAPTER 2: THIRD-ORDER NONLINEARITIES

2.1. Introduction

An external electromagnetic field applied to a medium exerts a force on all of the electrons comprising the medium. The radiation field of an ordinary light source is much smaller than the fields that bind the electrons to the atoms. The electron departures from equilibrium are small and consequently Hook's law for restoring force F=-kx is valid. That leads to a linear response [19]. A response of a linear system to an input function is expressed as a convolution of the input function and the transfer function. Therefore, as an electromagnetic field is applied to a medium, the induced polarization in the time domain is expressed as a convolution of the field and the medium's linear susceptibility:

$$P(t) = \varepsilon_0 \chi^{(1)}(t) * E(t) \tag{2.1}$$

The induced polarization, in the frequency domain is written by Fourier transform as:

$$P(\omega) = \varepsilon_0 \chi^{(1)}(\omega) E(\omega) \tag{2.2}$$

where ε_0 is the permittivity of the vacuum, $\chi^{(1)}$ is the first order susceptibility of the medium and E is the incident electromagnetic field. $\chi^{(1)}$ characterizes the linear interaction of light with the medium and describes the linear absorption coefficient and the linear refractive index [19].

If the incident radiation field on the medium is comparable with the atomic fields, the electronic displacements are so large that the Hooks' law, F=-kx, restoring force is no longer exactly true. The polarization response becomes nonlinearly related with the external field applied [20].

To describe the nonlinear effects the polarization response of the medium can be expanded in a power series in E, in the frequency domain [21]:

$$P = \varepsilon_0(\chi^{(1)}E + \chi^{(2)}E^2 + \chi^{(3)}E^3 + ...) = P^{(1)} + P^{(2)} + P^{(3)} + ... \quad (2.3)$$

where $\chi^{(n)}$ represents the n-th order optical susceptibility and ε_0 is the permittivity of the vacuum. For simplicity, frequency arguments have been omitted from Eq. 2.3

Each order of polarization is proportional to the electron displacement to the power of that order. Consequently, the bigger the displacement, the larger the nonlinear optical polarization response.

The first term ($\chi^{(1)}$) in the polarization expansion describes the linear response of the system as expressed by Eq.(2.1).

The second term ($\chi^{(2)}$) in the polarization expansion is responsible for nonlinear effects such as sum and difference frequency generation (SFG and DFG), second harmonic generation (SHG), linear electro-optic effect and optical rectification [21, 22].

The third order term ($\chi^{(3)}$) gives rise to effects such as third harmonic generation (THG), 2PA, NLR, optical Stark effect, stimulated Raman and Brillouin scattering and four-wave mixing.

Strong electromagnetic fields can induce even higher order nonlinear effects like three-photon or four-photon absorption (a$\chi^{(5)}$ and respectively, a $\chi^{(7)}$ process) and their associated nonlinear refraction. Linear and multiphoton absorption effects can induce cumulative effects like free carrier generation and excited state absorption. A key condition for these effects to take

place is having a generation rate sustained for a long time (the shorter the pulse, the larger the irradiance needed).

This work deals with NLA and NLR as third-order effects, i.e. 2PA and its associated nonlinear change in refractive index. 2PA induced free-carrier and excited-states effects are higher order effects (effective $\chi^{(5)}$ processes) which might contribute to the detected nonlinear signal from the pure bound electronic effects [23, 24]. The work presented in this dissertation deals with femtosecond pulses. In many cases these are too short to induce the above mentioned higher order effects.

The third-order polarization is expressed, in the time domain, as a three-dimensional convolution (in a similar way with Eq. 2.1 for the first-order polarization) [21]:

$$P^{(3)}(t) = \varepsilon_0 \int_{-\infty}^{\infty}\int_{-\infty}^{\infty}\int_{-\infty}^{\infty} \chi^{(3)}(t-t_1, t-t_2, t-t_3)\, E(t_1)\, E(t_2)\, E(t_3)\, dt_1 dt_2 dt_3 \qquad (2.4)$$

If we multiply the term under the integral with:

$$1 = e^{j(t-t_1)\omega_1 + i(t-t_2)\omega_2 + i(t-t_3)\omega_3} e^{-j(t-t_1)\omega_1 - i(t-t_2)\omega_2 - i(t-t_3)\omega_3}$$

and write E(t) as the Fourier transform of E(ω): $E(t) = \int_{-\infty}^{\infty} E(\omega) e^{-i\omega t} d\omega$, Eq. (2.4) will become:

$$P^{(3)}(t) = \varepsilon_0 \int_{-\infty}^{\infty}\int_{-\infty}^{\infty}\int_{-\infty}^{\infty} \chi^{(3)}(-\omega; \omega_1, \omega_2, \omega_3) E(\omega_1) E(\omega_2) E(\omega_3) e^{-j(\omega_1+\omega_2+\omega_3)t} d\omega_1 d\omega_2 d\omega_3 \qquad (2.5)$$

As we are interested in the dispersion of the nonlinear effects, we need to write the polarization term in the frequency domain. We can do that by Fourier transforming the time domain polarization term given by Eq. (2.5):

$$P^{(3)}(\omega) = \frac{1}{2\pi}\int_{-\infty}^{\infty} P^{(3)}(t)e^{j\omega t}dt$$
$$= \varepsilon_0 \int_{-\infty}^{\infty}\int_{-\infty}^{\infty}\int_{-\infty}^{\infty} \chi^{(3)}(-\omega;\omega_1,\omega_2,\omega_3)E(\omega_1)E(\omega_2)E(\omega_3)\delta[\omega-(\omega_1+\omega_2+\omega_3)]d\omega_1 d\omega_2 d\omega_3 \tag{2.6}$$

where the equality: $\frac{1}{2\pi}\int_{-\infty}^{\infty} e^{j[\omega-(\omega_1+\omega_2+\omega_3)]t}dt = \delta[\omega-(\omega_1+\omega_2+\omega_3)]$ was used.

2.2. Non-Degenerate Third-Order NLA and NLR

Nonlinear absorption and refraction may be measured using pump-probe experiments (which we will describe later in this work) where the pump and probe pulses may have different wavelengths. In this case the nonlinear absorption imposed on the probe by the pump is called "nondegenerate" NLA. So, it will be useful to know how the polarization term in Eq. (2.6) looks for the nondegenerate case. We will consider only the parallel polarization case as this is what we use in our pump-probe experiment [17]. (we use parallel polarizations because we found, for most of the materials, the nonlinear signal corresponding to parallel polarizations is larger than the one corresponding to perpendicular polarizations [22]). For unequal frequencies and parallel polarizations, the input fields in Eq. (2.6) will be expressed as [22]:

$$E(\omega_i) = \frac{1}{2}\left[E_0(\omega_a)\delta(\omega_i-\omega_a) + E_0^*(\omega_a)\delta(\omega_i+\omega_a) + E_0(\omega_b)\delta(\omega_i-\omega_b) + E_0^*(\omega_b)\delta(\omega_i+\omega_b)\right] \tag{2.7}$$

where i=1,2,3 and ω_a, ω_b are the frequencies of the two input beams.

Plugging the field expression given by (2.7) into Eq. (2.6), the induced polarization will be a sum of products of fields, containing the following terms [22]:

(1) $E_0^3(\omega_a)$ and $E_0^3(\omega_b)$ terms responsible for the *THG* at $\omega = \omega_a$ and $\omega = \omega_b$

(2) $|E_0(\omega_a)|^2 E_0(\omega_b)$ and $|E_0(\omega_b)|^2 E_0(\omega_a)$ terms responsible for *intensity-dependent effects* (nondegenerate 2PA and NLR) at $\omega = \omega_b$ and $\omega = \omega_a$ respectively

(3) $|E_0(\omega_a)|^2 E_0(\omega_a)$ and $|E_0(\omega_b)|^2 E_0(\omega_b)$ terms responsible for *self-action intensity-dependent effects* (degenerate 2PA and its associated nonlinear refractive index n_2) at $\omega = \omega_a$ and $\omega = \omega_b$, respectively

(4) $E_0^2(\omega_a) E_0(\omega_b)$ and $E_0^2(\omega_b) E_0(\omega_a)$ ($\omega = 2\omega_a + \omega_b$ and $\omega = 2\omega_b + \omega_a$)

(5) $E_0^2(\omega_a) E_0^*(\omega_b)$ and $E_0^2(\omega_b) E_0^*(\omega_a)$ ($\omega = 2\omega_a - \omega_b$ and $\omega = 2\omega_b - \omega_a$)

The nonlinear effects the terms in (4) and (5) are responsible for are *Coherent Anti-Stokes Raman Scattering* (if $\omega_b > \omega_a$) and *Coherent Stokes Raman Scattering* (if $\omega_a > \omega_b$).

We are interested further in the nonlinear terms responsible for the intensity-dependent effects (2) and (3).

The polarization corresponding to these terms has the following form:

$$P^{(3)}(\omega_a) = \frac{3}{4}\varepsilon_0 \chi^{(3)}(-\omega_a;\omega_a,-\omega_a,\omega_a)\left|E_0(\omega_a)\right|^2 E_0(\omega_a) + \frac{6}{4}\varepsilon_0 \chi^{(3)}(-\omega_a;\omega_a,-\omega_b,\omega_b)\left|E_0(\omega_b)\right|^2 E_0(\omega_a) \tag{2.8}$$

and

$$P^{(3)}(\omega_b) = \frac{3}{4}\varepsilon_0 \chi^{(3)}(-\omega_b;\omega_b,-\omega_b,\omega_b)\left|E_0(\omega_b)\right|^2 E_0(\omega_b) + \frac{6}{4}\varepsilon_0 \chi^{(3)}(-\omega_b;\omega_b,-\omega_a,\omega_a)\left|E_0(\omega_a)\right|^2 E_0(\omega_b) \tag{2.9}$$

Consider the fields $E_0(\omega_a)$ and $E_0(\omega_b)$ have the form:

$$E_0(\omega_a) = \frac{1}{2}[A_a(z)e^{j\Phi_a(z)}e^{j(k_a z-\omega_a t)}] + c.c. \tag{2.10}$$

$$E_0(\omega_b) = \frac{1}{2}[A_b(z)e^{j\Phi_b(z)}e^{j(k_b z-\omega_b t)}] + c.c. \tag{2.11}$$

The evolution of the fields with propagation is derived from Maxwell's equations [22]:

$$\frac{\partial^2 E_0(\omega_a)}{\partial z^2} - \frac{n_0}{c^2}\frac{\partial^2 E_0(\omega_a)}{\partial t^2} = \mu_0 \frac{\partial^2 P^{(3)}(\omega_a)}{\partial t^2} \tag{2.12}$$

$$\frac{\partial^2 E_0(\omega_b)}{\partial z^2} - \frac{n_0}{c^2}\frac{\partial^2 E_0(\omega_b)}{\partial t^2} = \mu_0 \frac{\partial^2 P^{(3)}(\omega_b)}{\partial t^2} \tag{2.13}$$

These derivatives have the following form:

$$\begin{aligned}\frac{\partial^2 E_0(\omega_i)}{\partial z^2} = \frac{1}{2}e^{j\Phi_i(z)}e^{j(k_i z-\omega_i t)}\{&\frac{\partial^2 A_i(z)}{\partial z^2} - A_i(z)[\frac{\partial \Phi_i(z)}{\partial z}]^2 - 2k_i A_i(z)\frac{\partial \Phi_i(z)}{\partial z} - k_i^{\,2} A_i(z) + \\ &j[A_i(z)\frac{\partial^2 \Phi_i(z)}{\partial z^2} + 2\frac{\partial A_i(z)}{\partial z}\frac{\partial \Phi_i(z)}{\partial z} + 2k_i\frac{\partial A_i(z)}{\partial z}]\} + c.c.\end{aligned} \tag{2.14}$$

$$\frac{\partial^2 E_0(\omega_i)}{\partial t^2} = -\frac{1}{2}A_i(z)e^{j\Phi_i(z)}e^{j(k_i z-\omega_i t)}\omega_i^{\,2} + c.c. \tag{2.15}$$

where i=a,b.

$$\begin{aligned}\frac{\partial^2 P^{(3)}(\omega_a)}{\partial t^2} = -\frac{1}{2}e^{j(k_a z-\omega_a t)}\varepsilon_0\omega_a^{\,2}[&\frac{3}{4}\chi^{(3)}(-\omega_a;\omega_a,-\omega_a,\omega_a)\left|E_0(\omega_a)\right|^2 A_a(z)e^{j\Phi_a(z)} + \\ &\frac{6}{4}\chi^{(3)}(-\omega_a;\omega_a,-\omega_b,\omega_b)\left|E_0(\omega_b)\right|^2 A_a(z)e^{j\Phi_a(z)}] + c.c.\end{aligned} \tag{2.16}$$

$$\frac{\partial^2 P^{(3)}(\omega_b)}{\partial t^2} = -\frac{1}{2} e^{j(k_b z - \omega_b t)} \varepsilon_0 \omega_b{}^2 [\frac{3}{4} \chi^{(3)}(-\omega_b;\omega_b,-\omega_b,\omega_b) \left|E_0(\omega_b)\right|^2 A_b(z) e^{j\Phi_b(z)} + \frac{6}{4} \chi^{(3)}(-\omega_b;\omega_b,-\omega_a,\omega_a) \left|E_0(\omega_a)\right|^2 A_b(z) e^{j\Phi_b(z)}] + c.c. \tag{2.17}$$

Plugging the derivatives given by the relations (2.14)-(2.17) into the equations (2.12) and (2.13), we get:

$$\left[\frac{\partial^2 A_a(z)}{\partial z^2} - A_a(z)\left(\frac{\partial \Phi_a(z)}{\partial z}\right)^2 - 2k_a A_a(z)\frac{\partial \Phi_a(z)}{\partial z}\right] + j\left[A_a(z)\frac{\partial^2 \Phi_a(z)}{\partial z^2} + 2\frac{\partial A_a(z)}{\partial z}\frac{\partial \Phi_a(z)}{\partial z} + 2k_a \frac{\partial A_a(z)}{\partial z}\right] = -\varepsilon_0 \mu_0 \omega_a{}^2 \left[\frac{3}{4}\chi^{(3)}(-\omega_a;\omega_a,-\omega_a,\omega_a)\left|E_0(\omega_a)\right|^2 A_a(z) + \frac{6}{4}\chi^{(3)}(-\omega_a;\omega_a,-\omega_b,\omega_b)\left|E_0(\omega_b)\right|^2 A_a(z)\right] \tag{2.18}$$

$$\left[\frac{\partial^2 A_b(z)}{\partial z^2} - A_b(z)\left(\frac{\partial \Phi_b(z)}{\partial z}\right)^2 - 2k_b A_b(z)\frac{\partial \Phi_b(z)}{\partial z}\right] + j\left[A_b(z)\frac{\partial^2 \Phi_b(z)}{\partial z^2} + 2\frac{\partial A_b(z)}{\partial z}\frac{\partial \Phi_b(z)}{\partial z} + 2k_b \frac{\partial A_b(z)}{\partial z}\right] = -\varepsilon_0 \mu_0 \omega_b{}^2 \left[\frac{3}{4}\chi^{(3)}(-\omega_b;\omega_b,-\omega_b,\omega_b)\left|E_0(\omega_b)\right|^2 A_b(z) + \frac{6}{4}\chi^{(3)}(-\omega_b;\omega_b,-\omega_a,\omega_a)\left|E_0(\omega_a)\right|^2 A_b(z)\right] \tag{2.19}$$

If changes in the field amplitude E(z) are small over length scales on the order of λ, the Slowly Varying Envelope Approximation (SVEA) can be applied [20]:

$$\left|\frac{\partial^2 E(z)}{\partial z^2}\right| << 2k\left|\frac{\partial E(z)}{\partial z}\right| \qquad . \tag{2.20}$$

In our case, the amplitude is a complex one and has the form $A_i(z)e^{j\Phi_i(z)}$ (i=a,b for the two input fields). The SVEA $A_i(z)e^{j\Phi_i(z)}$ writes as follows:

$$\left|\frac{\partial^2 (A_i(z)e^{j\Phi_i(z)})}{\partial z^2}\right| = \frac{\partial^2 A_i(z)}{\partial z^2} - A_i(z)\left(\frac{\partial \Phi_i(z)}{\partial z}\right)^2 + j\left(A_i(z)\frac{\partial^2 \Phi_i(z)}{\partial z^2} + 2\frac{\partial A_i(z)}{\partial z}\frac{\partial \Phi_i(z)}{\partial z}\right) \tag{2.21}$$

$$\left|\frac{\partial (A_i(z)e^{j\Phi_i(z)}}{\partial z^2}\right| = \frac{\partial A_i(z)}{\partial z} + jA_i(z)\frac{\partial \Phi_i(z)}{\partial z} \tag{2.22}$$

$$\rightarrow \qquad \frac{\partial^2 A_i(z)}{\partial z^2} - A_i(z)\left(\frac{\partial \Phi_i(z)}{\partial z}\right)^2 << \frac{\partial A_i(z)}{\partial z} \tag{2.23}$$

$$A_i(z)\frac{\partial^2 \Phi_i(z)}{\partial z^2} + 2\frac{\partial A_i(z)}{\partial z}\frac{\partial \Phi_i(z)}{\partial z} << A_i(z)\frac{\partial \Phi_i(z)}{\partial z} \tag{2.24}$$

Taking into account the SVEA approximation given by (2.23) and (2.24) the equations for field propagation (2.18) and (2.19) are simplified and get the form:

$$\begin{aligned} &-2k_a A_a(z)\frac{\partial \Phi_a(z)}{\partial z} + j2k_a\frac{\partial A_a(z)}{\partial z} = \\ &-\varepsilon_0\mu_0\omega_a{}^2\left[\frac{3}{4}\chi^{(3)}(-\omega_a;\omega_a,-\omega_a,\omega_a)\left|E_0(\omega_a)\right|^2 A_a(z) + \frac{6}{4}\chi^{(3)}(-\omega_a;\omega_a,-\omega_b,\omega_b)\left|E_0(\omega_b)\right|^2 A_a(z)\right] \end{aligned} \tag{2.25}$$

$$\begin{aligned} &-2k_b A_b(z)\frac{\partial \Phi_b(z)}{\partial z} + j2k_b\frac{\partial A_b(z)}{\partial z} = \\ &-\varepsilon_0\mu_0\omega_b{}^2\left[\frac{3}{4}\chi^{(3)}(-\omega_b;\omega_b,-\omega_b,\omega_b)\left|E_0(\omega_b)\right|^2 A_b(z) + \frac{6}{4}\chi^{(3)}(-\omega_b;\omega_b,-\omega_a,\omega_a)\left|E_0(\omega_a)\right|^2 A_b(z)\right] \end{aligned}$$

(2.26)

As a complex quantity $\chi^{(3)}$ can be written as [22]:

$$\chi^{(3)} = \chi_r^{(3)} + j\chi_i^{(3)} \tag{2.27}$$

Separating real and imaginary parts for the two equations given by (2.25) and (2.26) we can get the propagation equations for the amplitude and the phase:

$$\begin{cases} \dfrac{\partial A_a(z)}{\partial z} = -\dfrac{3\omega_a}{8n_a c}\left[\chi_i^{(3)}(-\omega_a;\omega_a,-\omega_a,\omega_a)A_a^{\,3}(z) + 2\chi_i^{(3)}(-\omega_a;\omega_a,-\omega_b,\omega_b)A_b^{\,2}A_a(z)\right] \\ \dfrac{\partial A_b(z)}{\partial z} = -\dfrac{3\omega_b}{8n_b c}\left[\chi_i^{(3)}(-\omega_b;\omega_b,-\omega_b,\omega_b)A_b^{\,3}(z) + 2\chi_i^{(3)}(-\omega_b;\omega_b,-\omega_a,\omega_a)A_a^{\,2}A_b(z)\right] \end{cases} \tag{2.28}$$

$$\begin{cases} \dfrac{\partial \Phi_a(z)}{\partial z} = \dfrac{3\omega_a}{8n_a c}\left[\chi_r^{(3)}(-\omega_a;\omega_a,-\omega_a,\omega_a)A_a^{\,2}(z) + 2\chi_r^{(3)}(-\omega_a;\omega_a,-\omega_b,\omega_b)A_b^{\,2}(z)\right] \\ \dfrac{\partial \Phi_b(z)}{\partial z} = \dfrac{3\omega_b}{8n_b c}\left[\chi_r^{(3)}(-\omega_b;\omega_b,-\omega_b,\omega_b)A_b^{\,2}(z) + 2\chi_r^{(3)}(-\omega_b;\omega_b,-\omega_a,\omega_a)A_a^{\,2}(z)\right] \end{cases} \tag{2.29}$$

where n_a, n_b are the linear refractive indices of the medium corresponding to ω_a and ω_b.

We usually need these equations in terms of irradiance [22]:

$$I(z) = \frac{n_0 \varepsilon_0 c}{2} A^2(z) \tag{2.30}$$

Non-degenerate 2PA:

Using the relation (2.30), the equations (2.28) yield:

$$\begin{cases} \dfrac{d}{dz} I_a(z) = -\beta_{aa} I_a^2(z) - 2\beta_{ab} I_a(z) I_b(z) \\ \dfrac{d}{dz} I_b(z) = -\beta_{bb} I_b^2(z) - 2\beta_{ba} I_a(z) I_b(z) \end{cases} \tag{2.31}$$

where $\begin{cases} \beta_{aa} = \dfrac{3\omega_a}{2n_a{}^2c^2\varepsilon_0}\chi_i{}^{(3)}(-\omega_a;\omega_a,-\omega_a,\omega_a) \\ \beta_{ab} = \dfrac{3\omega_a}{2n_an_bc^2\varepsilon_0}\chi_i{}^{(3)}(-\omega_a;\omega_a,-\omega_b,\omega_b) \\ \beta_{bb} = \dfrac{3\omega_b}{2n_b{}^2c^2\varepsilon_0}\chi_i{}^{(3)}(-\omega_b;\omega_b,-\omega_b,\omega_b) \\ \beta_{ba} = \dfrac{3\omega_b}{2n_an_bc^2\varepsilon_0}\chi_i{}^{(3)}(-\omega_b;\omega_b,-\omega_a,\omega_a) \end{cases}$ are the 2PA coefficients

(2.32)

They can be measured by performing a pump-probe experiment, in which a strong beam (pump) is overlapped in time and space with a weak beam (probe) in the sample [17]. Consider I_b (the pump irradiance)>>I_a (the probe irradiance). Solving the system of equations (2.31) for the two beams, we get:

$$\begin{cases} \dfrac{d}{dz}I_a(z) = -2\beta_{ab}I_a(z)I_b(z) \\ \dfrac{d}{dz}I_b(z) = -\beta_{bb}I_b^2(z) \end{cases} \tag{2.33}$$

$$\rightarrow \qquad \begin{cases} I_b(L) = \dfrac{I_b(0)}{1+\beta_{bb}I_b(0)L} \\ I_a(L) = \dfrac{I_a(0)}{\left[1+\beta_{bb}I_b(0)L\right]^{\frac{2\beta_{ab}}{\beta_{bb}}}} \end{cases} \tag{2.34}$$

For the pump-probe degenerate case, $\omega_a = \omega_b$ and $\beta_{aa} = \beta_{ab} = \beta_{ba} = \beta_{bb} = \beta$,. The solution (2.34) will have the following form:

$$I_a(L) = \frac{I_a(0)}{\left[1+\beta I_b(0)L\right]^2} \tag{2.35}$$

This equation will be later compared with the one obtained for a single beam propagation.

Non-degenerate third-order NLR:

Using the relation (2.30), the equations (2.28) yield:

$$\begin{cases} \dfrac{\partial \Phi_a(z)}{\partial z} = \dfrac{3\omega_a}{4n_a{}^2\varepsilon_0 c^2}\left[\chi_r{}^{(3)}(-\omega_a;\omega_a,-\omega_a,\omega_a)I_a(z) + 2\chi_r{}^{(3)}(-\omega_a;\omega_a,-\omega_b,\omega_b)I_b(z)\right] \\ \dfrac{\partial \Phi_b(z)}{\partial z} = \dfrac{3\omega_a}{4n_a{}^2\varepsilon_0 c^2}\left[\chi_r{}^{(3)}(-\omega_b;\omega_b,-\omega_b,\omega_b)I_b(z) + 2\chi_r{}^{(3)}(-\omega_b;\omega_b,-\omega_a,\omega_a)I_a(z)\right] \end{cases} \tag{2.36}$$

These equations can be written as:

$$\begin{cases} \dfrac{\partial \Phi_a(z)}{\partial z} = n_{2aa}k_0 I_a(z) + n_{2ab}k_0 I_b(z) \\ \dfrac{\partial \Phi_b(z)}{\partial z} = n_{2bb}k_0 I_b(z) + n_{2ba}k_0 I_a(z) \end{cases}$$ the equations for the phase propagation of the two beams

(2.37)

where, $$\begin{cases} n_{2aa} = \dfrac{3}{4n_a{}^2\varepsilon_0 c}\chi_r{}^{(3)}(-\omega_a;\omega_a,-\omega_a,\omega_a) \\ n_{2ab} = \dfrac{3}{2n_a{}^2\varepsilon_0 c}\chi_r{}^{(3)}(-\omega_a;\omega_a,-\omega_b,\omega_b) \\ n_{2ba} = \dfrac{3}{2n_a{}^2\varepsilon_0 c}\chi_r{}^{(3)}(-\omega_b;\omega_b,-\omega_a,\omega_a) \\ n_{2bb} = \dfrac{3}{4n_b{}^2\varepsilon_0 c}\chi_r{}^{(3)}(-\omega_b;\omega_b,-\omega_b,\omega_b) \end{cases} \tag{2.38}$$

are the non-degenerate third-order nonlinear refractive indices.

They can be evaluated from Kramers-Krönig relations if the non-degenerate 2PA spectrum is measured [25]:

$$\Delta n(\omega_p;\omega_e) = \frac{c}{\pi}\int_0^\infty \frac{\Delta\alpha(\Omega;\omega_e)}{\Omega^2 - \omega_p{}^2} d\Omega \tag{2.39}$$

where the left term represents the change in the refractive index due to the nonlinear contribution while the numerator on the right side expresses the change in nonlinear absorption; ω_p, ω_e-are the frequencies of the probe and of the excite (pump) beam respectively.

2.3. Degenerate Third-Order NLA and NLR

For a single beam input, the field substituted in Eq. (2.6) can be written as [22]:

$$E(\omega_i) = \frac{1}{2}\left[E_0(\omega_0)\delta(\omega_i - \omega_0) + E_0^*(\omega_0)\delta(\omega_i + \omega_0)\right] \tag{2.40}$$

and the expression of the corresponding induced polarization will have the form:

$$\begin{aligned} P^{(3)} = {} & \frac{1}{4}\varepsilon_0[\chi^{(3)}(-3\omega_0;\omega_0,\omega_0,\omega_0)E_0^3(\omega_0) + \chi^{(3)*}(-3\omega_0;\omega_0,\omega_0,\omega_0)E_0^{*3}(\omega_0)] + \\ & \frac{3}{4}\varepsilon_0[\chi^{(3)}(-\omega_0;\omega_0,-\omega_0,\omega_0)\left|E_0(\omega_0)\right|^2 E_0(\omega_0) + \chi^{(3)*}(-\omega_0;\omega_0,-\omega_0,\omega_0)\left|E_0(\omega_0)\right|^2 E_0^*(\omega_0)] \end{aligned} \tag{2.41}$$

The first two terms are responsible for THG and the last ones correspond to the self-action intensity-dependent effects (3rd order NLR and 2PA). Degenerate 2PA and the 3rd order NLR effects will be of our interest in the following discussion.

Similarly with the non-degenerate case, the field describing a single beam and its corresponding induced polarization of the medium:

$$E_0(\omega_0) = \frac{1}{2}\left[A(z)e^{j\Phi(z)}e^{j(kz-\omega_0 t)}\right] + c.c. \tag{2.42}$$

$$P^{(3)}(\omega_0) = \frac{3}{4}\varepsilon_0 \chi^{(3)}(-\omega_0;\omega_0,-\omega_0,\omega_0)\left|E_0(\omega_0)\right|^2 E_0(\omega_0) \tag{2.43}$$

are used in the Maxwell's wave eq. (2.12) which, after applying the SVEA, becomes:

$$-\frac{\partial\Phi(z)}{\partial z}A(z) + j\frac{\partial A(z)}{\partial z} = -\frac{3\omega_0}{8n_0 c}\chi^{(3)}(-\omega_0;\omega_0,-\omega_0,\omega_0)A^3(z) \tag{2.44}$$

Setting $\chi^{(3)}(-\omega_0;\omega_0,-\omega_0,\omega_0) = \chi_r^{(3)}(-\omega_0;\omega_0,-\omega_0,\omega_0) + j\chi_i^{(3)}(-\omega_0;\omega_0,-\omega_0,\omega_0)$ the real and the imaginary parts can be separated in Eq. (2.44) above, as follow:

$$\begin{cases} \dfrac{\partial A(z)}{\partial z} = -\dfrac{3\omega_0}{8n_0 c}\chi_i^{(3)}(-\omega_0;\omega_0,-\omega_0,\omega_0)A^3(z) \\ \dfrac{\partial\Phi(z)}{\partial z} = \dfrac{3\omega_0}{8n_0 c}\chi_r^{(3)}(-\omega_0;\omega_0,-\omega_0,\omega_0)A^2(z) \end{cases} \tag{2.45}$$

Degenerate 2PA

Using Eq. (2.30), the equation for the amplitude propagation (2.45) yields:

$$\frac{dI(z)}{dz} = -\frac{3\omega_0}{2n_0^2 c^2 \varepsilon_0}\chi_i^{(3)}(-\omega_0;\omega_0,-\omega_0,\omega_0)I^2(z) \tag{2.46}$$

Defining $\beta = \dfrac{3\omega_0}{2n_0^2 c^2 \varepsilon_0}\chi_i^{(3)}(-\omega_0;\omega_0,-\omega_0,\omega_0)$ the 2PA coefficient, the above equation is written as:

$$\frac{dI(z)}{dz} = -\beta I^2(z) \tag{2.47}$$

and its solution, considering a uniform illumination and square pulse in time, has the form:

$$I(L) = \frac{I(0)}{1 + \beta I(0) L} \tag{2.48}$$

which represents the evolution of the irradiance after propagation a distance L in the medium (sample). Comparing this expression for the irradiance corresponding to a single beam propagating through a nonlinear medium with the one corresponding to a degenerate pump-probe experiment (2.35), one should notice the evolution of the irradiance differs by a factor of 2 in the denominator.

N.B. Expression (2.47) for *I(L)* was derived by assuming the SVEA holds and also by neglecting the transverse coordinates of the amplitude (i.e. the diffraction term in the wave equation was neglected). Anticipating, the last condition will be expressed in the Z-scan theory for measurements of degenerate nonlinearities by the "thin sample approximation" [18].

If the linear absorption of the medium is taken into account, equation (2.47) is written [20]:

$$\frac{dI(z)}{dz} = -\alpha I(z) - \beta I^2(z) \tag{2.49}$$

where α is the linear absorption coefficient. Eq. (2.49) has the following solution:

$$I(L) = \frac{I(0)}{e^{\alpha L} + \beta I(0) \dfrac{e^{\alpha L} - 1}{\alpha}} \tag{2.50}$$

or, if an effective length is defined as: $L_{eff} = \dfrac{e^{\alpha L} - 1}{\alpha}$:

$$I(L) = \frac{I(0) e^{-\alpha L}}{1 + \beta e^{-\alpha L} I(0) L_{eff}} \tag{2.51}$$

It is important to note that z=0 refers to the position just inside the surface of the sample, so that I(0) includes any surface losses [26]. If I(0) is considered to be the irradiance measured in front

of the sample, the reflection of the entrance surface has to be taken into account and therefore, in the Eq. (2.51), I(0) has to be replaced by (1-R)I(0), where R is the reflectivity which depends on the linear refractive index n, as $R=(n-1)^2/(n+1)^2$. Eq. (2.51) will be written [27]:

$$I(L) = (1-R)\frac{(1-R)I(0)e^{-\alpha L}}{1+\beta e^{-\alpha L}(1-R)I(0)L_{eff}} \tag{2.52}$$

where the reflection was taken into account on the exit surface also. Thus, I(L) represents the irradiance just after the surface of the sample.

A useful expression can be obtained if the inverse of the transmission is considered:

$$T^{-1} = \frac{I(0)}{I(L)} = \frac{1}{(1-R)^2 e^{-\alpha L}} + \beta\frac{1}{1-R}I(0)L_{eff} \tag{2.53}$$

A plot of T^{-1} versus I_0 will have the form of a straight line with:

$$\text{intercept} \qquad \frac{1}{(1-R)^2 e^{-\alpha L}} \quad \text{and slope} \qquad \beta\frac{1}{1-R}L_{eff} \tag{2.54}$$

It is important to remember the expression (2.53) above was derived by considering square pulses [26]. If Gaussian pulses in space and time are considered, the expression for T^{-1} has a more complex form. Nevertheless, in the limit of a small nonlinear absorption and/or the incident irradiance, the expression for T^{-1} simplifies to [26]:

$$T^{-1} = \frac{I(0)}{I(L)} = \frac{1}{(1-R)^2 e^{-\alpha L}}\left[1-\frac{1}{2\sqrt{2}}\beta(1-R)I_0\frac{L_{eff}}{e^{\alpha L}}\right]^{-1} \tag{2.55}$$

This case, a plot of T^{-1} versus I_0 is not a straight line any more but for small nonlinear transmittance changes can be approximated as being a line with:

$$\text{an intercept of } \frac{1}{(1-R)^2 e^{-\alpha L}} \quad \text{and a slope of} \quad \frac{1}{2\sqrt{2}}\beta\frac{1}{1-R}L_{eff} \tag{2.56}$$

The slope was derived from the 1st binomial expansion of 1/(1-x) in Eq. (2.55). This expression gives a slope different from the slope corresponding to a uniform illumination (square pulses) by a factor of $1/(2\sqrt{2})$. The complete derivation of the expression (2.55) can be found in ref [26]. The expression above shows that one can get a direct access to the 2PA coefficient by measuring the attenuation of a focused beam with varying irradiance. However, such irradiance ramping experiments have limited accuracy because of the small nonlinear absorption and/or the incident irradiance limit imposed to derive the simplified expression for the transmission given by (2.55). Another source of inaccuracy might be the difficulty in estimating the beam waist leading to uncertainty in the irradiance [26].

The Z-scan technique was introduced by Sheik-Bahae *et.al.*[18] for accurate and sensitive measurements of nonlinear absorption and refraction by translating a sample along the optical axis of a focused Gaussian beam. This method will be described in the next chapter of this work.

Degenerate third- order NLR

Using Eq. (2.30), the equation for the phase propagation (2.45) yields:

$$\frac{d\Phi(z)}{dz} = -\frac{3\omega_0}{4n_0{}^2c^2\varepsilon_0}\chi_r{}^{(3)}(-\omega_0;\omega_0,-\omega_0,\omega_0)I(z) \tag{2.57}$$

or:

$$\frac{d\Phi(z)}{dz} = n_2 k_0 I(z) \tag{2.58}$$

where $n_2 = \frac{3}{4n_0^{\ 2}\varepsilon_0 c}\chi_r^{(3)}(-\omega;\omega,-\omega,\omega)$ is the 3-rd order nonlinear refractive index. n_2 has units of m^2/W as it was defined as $\Delta n = n_0 + n_2 I$, Δn-the change in refractive index, n_0-the linear refractive index .

If a thin sample is assumed such that changes of the beam diameter due to nonlinear refraction or diffraction do not take place in the sample [18], the phase accumulated in the sample can be calculated by inserting the irradiance distribution through the sample (2.50) in Eq. (2.58).

$$\rightarrow \qquad \frac{d\Phi(z)}{dz} = \gamma k_0 \frac{I(0)e^{-\alpha z}}{1+\beta e^{-\alpha z} I(0)\frac{e^{\alpha z}-1}{\alpha}} \tag{2.59}$$

After propagating a distance L in the sample, the accumulated phase will be given by:

$$\Delta\Phi(L) = \frac{k\gamma}{\beta}\ln\left[1+\frac{\beta}{\alpha}I(0)(1-e^{-\alpha L})\right] \tag{2.60}$$

As mentioned, above, the absolute value of the 3rd order nonlinear refractive index coefficient n_2, and consequently, the accumulated phase through the sample can be measured by a Z-scan [18] experiment as will be explained in Chapter 4 of this work.

CHAPTER 3: LASER SYSTEM AND PARAMETRIC DEVICES FOR NONLINEAR MATERIAL CHARACTERIZATION

High intensity sources need to be used for nonlinear effects studies. High intensities are obtained by using pulsed laser systems with either high energy per pulse (limited however by the optical components' damage threshold) or, short pulse duration.

The laser system used for our experiments was a regeneratively-amplified, femtosecond Ti:Sapphire laser system manufactured by Clark MXR, Inc. As our work involves nonlinear spectroscopy studies, a tunable source, besides a powerful one, is necessary. This task was fulfilled by two optical parametric generator/amplifier systems.

The aforementioned laser systems are described in the next paragraphs of this chapter.

3.1. Ti:Sapphire Regeneratively Amplified Laser System

Our model CPA-2001/2010 Ti:Sapphire regeneratively amplified laser system operates at 775nm, 1kHz repetition rate, 145 fs and ~850μJ per pulse.

Principle of operation

Depending on the characteristics of the input and the gain media, a system may require a one-pass amplifier, a several-pass amplifier, or a regenerative amplifier. For Ti:Sapphire (Ti:Al_2O_3-titanium doped aluminum oxide crystal) several passes are not enough to reach saturation so, the crystal is placed in a cavity in which the pulse from the laser oscillator performs multiple passes through the Ti:sapphire crystal. An electro-optic modulator is used to allow a single pulse from the oscillator to enter the amplifier cavity. This pulse then makes tens of passes through the Ti:sapphire crystal, which is pumped by a Q-switched, frequency-doubled Nd:YAG laser. Once most of the pump energy has been extracted from the crystal, the same electro-optic modulator switches to deflect the pulse out of the cavity. The energy level in the cavity after the multiple passes through the Ti:Sapphire approaches the milijoule level which for femtosecond pulses results in a peak power high enough to damage the Ti:sapphire crystal. To avoid damaging the crystal the pulses from the oscillator are stretched temporally, then amplified and finally re-compressed. This method is called Chirped Pulse Amplification (CPA) and it was introduced by Strickland and Mourou in 1985 [28].

How does the regenerative amplifier of our Ti:Sappire cavity work?

The layout of the regenerative amplifier of our Ti:Sapphire laser is presented in Fig. 3-1.

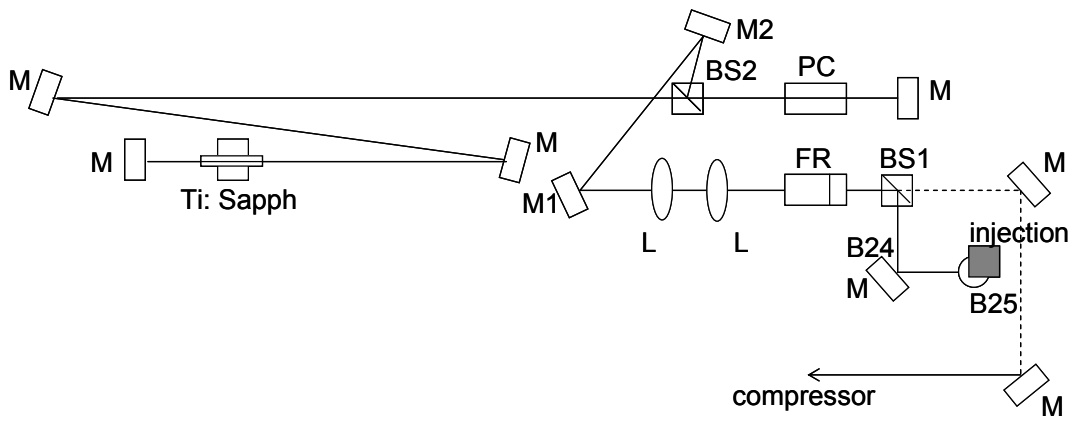

Figure 3-1::Regenerative amplifier cavity. M-mirror; BS-beamsplitter; FR-Faraday rotator; PC-Pockel cell

The pulse from the oscillator, after passing through the stretcher, is directed (seeded) into the amplifier cavity by the injection mirror B25. The seed beam enters the cavity vertically polarized. It gets reflected by BS1 (which reflects vertical polarization and transmits horizontal polarization) into the Faraday rotator. The Faraday rotator rotates the polarization with 45^0. The beam polarized at 45^0 gets reflected by M1, M2 and by BS2 into the Pockel cell.

When the voltage on the Pockel cell is off, nothing happens to the beam polarization. The beam is reflected back unchanged on BS2 which sends it back on M2 and M1. From M1 it goes into

the Faraday rotator which adds another 45^0, the beam becomes horizontally polarized and the reflection back to the injection mirror is blocked.

When the voltage on the Pockel cell turns on, the beam polarization is rotated such that the beam is transmitted by BS2. The voltage on the Pockel cell switches off allowing the beam to make multiple passes through the Ti:Sapphire (which reached a maximum gain) to get amplified. When the Pockel is turned back on, the beam polarization is rotated such that the beam is reflected out of the cavity by BS2. The beam is reflected by the mirrors M2 and M1 into the Faraday rotator. The FR rotates the beam 45^0, the polarization becomes horizontal and gets transmitted by BS1. The amplified beam goes then into the compressor.

The laser system is arranged in a bi-level optical layout design. The oscillator and the stretcher lay on the bottom level. The oscillator is an erbium doped fiber ring laser, invented by Ippen's and Haus' group at MIT [29]. It is pumped by a laser diode operating at approximately 980nm. The output of the oscillator passes a PPLN (periodically poled lithium niobate) crystal after which its wavelength is centered on 775nm. The seed is sent to the pulse stretcher. After the pulse is temporally broadened it gets directed in the upper level into the amplifier cavity. The upper level houses the Ti:Sappire amplifier cavity, the Ti:Sapphire pump laser, in our case a frequency-doubled Nd:YAG Q-switched laser (ORC) and the compressor. The pump laser operates at 532 nm, 1kHz repetition rate and an output power of 8W. Frequency-doubled Nd:YAG or NdYLF lasers are usually used for the pulsed Ti: Sapphire lasers as their output overlap the absorption spectrum of Ti:Sappire crystals which covers the range from less than 400nm to just beyond 630nm with a peak around 490nm as can be seen in Fig. 3-2 [30].

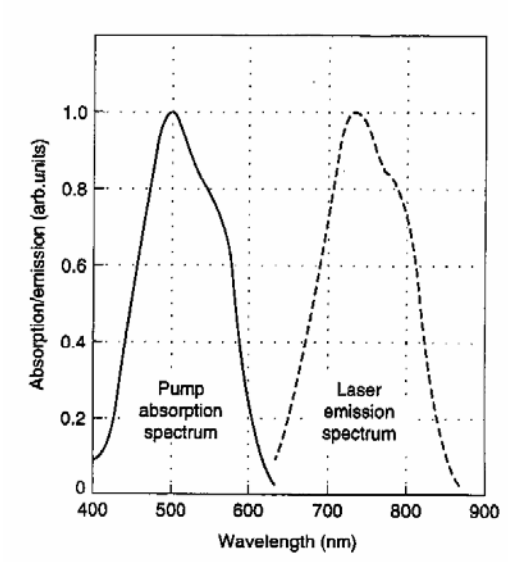

Figure 3-2: Absorption and emission spectra of titanium:sapphire laser amplifier rod

As explained above, after the seed pulse (775nm) gets amplified it is sent to the compressor where is temporally compressed to ~140fs. The timing of the Pockels cell can be adjusted so that a specific single pulse gets switched out of the regenerative amplifier.

A spatial profile of the laser beam taken at 2m away from the exit aperture of the laser using a CCD camera is shown in Fig. 3-3.

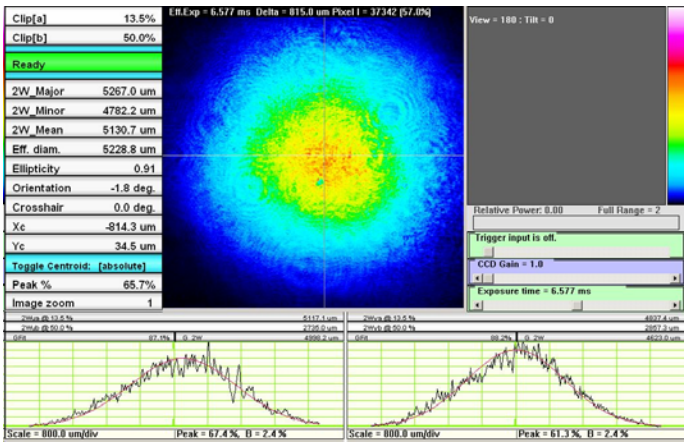

Figure 3-3: Far field spatial profile of the 775nm output of the Ti:Sapphire regeneratively amplified system

As noticed, the spatial distribution of our beam intensity is very close to a Gaussian one.

The temporal characterization of the 775nm output of our Ti:Sapphire laser system using a commercial Grenouille set-up [31] is presented in Fig. 3-4.

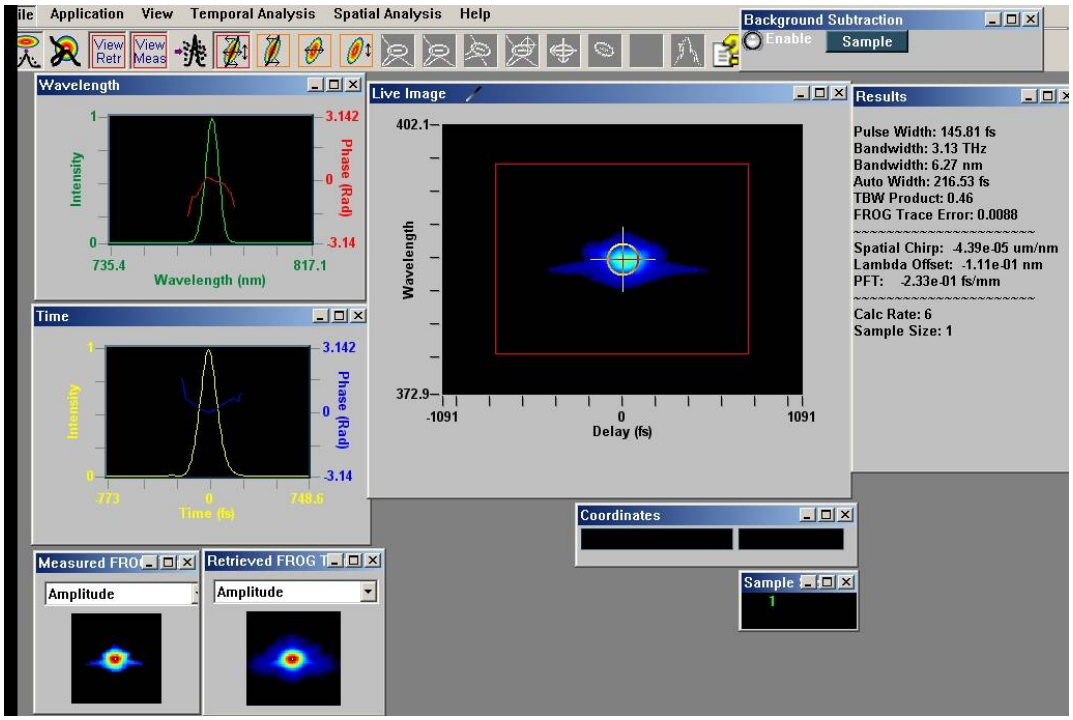

Figure 3-4: Temporal characterization of 775nm output beam of the Ti:Sapphire regeneratively amplified system

The pulse duration is measured to be 145fs (FWHM of irradiance) which for a measured spectral bandwidth of 6.27nm yield a time-bandwidth product of 0.46, 4.5% larger than 0.44 corresponding to a transform-limited pulse.

The additional information the Grenouille trace provides, regards the temporal/spatial chirp and the pulse front-tilt. Spatial chirp would be indicated by a tilt in the otherwise symmetrical Grenouille trace while an off-center trace would be an indication of pulse-front tilt [31]. The

Grenouille trace above shows these beam distortions are negligible. The temporal chirp is not revealed by the Grenouille trace but the software does give us information about the temporal phase as shown in a left panel. Its slightly quadratical shape infers the presence of some linear chirp. The time-bandwidth product close to the one corresponding to a transform-limited pulse shows the temporal chirp should not be significant.

The spatial and temporal beam profile of the Ti:Sapphire laser play an important role as its output is used to pump the optical parametric generator/amplifier systems in our lab.

3.2. Optical Parametric Generator/Amplifier (OPG/OPA) Systems

Two OPG/OPA systems available in our lab have been used in the experiments presented in this work. These are TOPAS (Traveling-wave Optical Parametric Amplifier of Superfluorescence) systems manufactured by Light Conversion, Ltd., Lithuania.

Principle of operation

In the *parametric generation* process, a photon (pump) is split into two photons of lesser energy (signal and idler) as a result of a parametric interaction, a second order nonlinear process inside a crystal (a discussion about parametric vs non-parametric processes can be found in Reference 17).

In the *parametric amplification* process, the pump photons are converted into signal and idler photons by beginning with above-noise levels of signal and idler.

Inside the TOPAS, a combination OPG/OPA system, the incoming pump beam (provided by the Ti:Sapphire laser) is split into three components by two beamsplitters (see Fig.3-5). A first component makes a total of three passes through the nonlinear crystal (BBO-Beta Barium Borate-β-BaB_2O_4). In the first pass, a parametric superfluorescence (SFL) signal is generated. Two stages of pre-amplification follows in the next two passes of the SFL signal through the crystal. The SFL signal, spread in spectrum in the plane of the nonlinear crystal, serves a seed beam in the next to amplification stages. The second component provided by the incoming pump beam makes a fourth pass through the crystal and ends the pre-amplification stage as it overlaps the SFL signal in the crystal. The last amplification stage (fifth pass through nonlinear crystal), which is pumped by the third component provided by the incoming pump, boosts the energy of the parametric pulse.

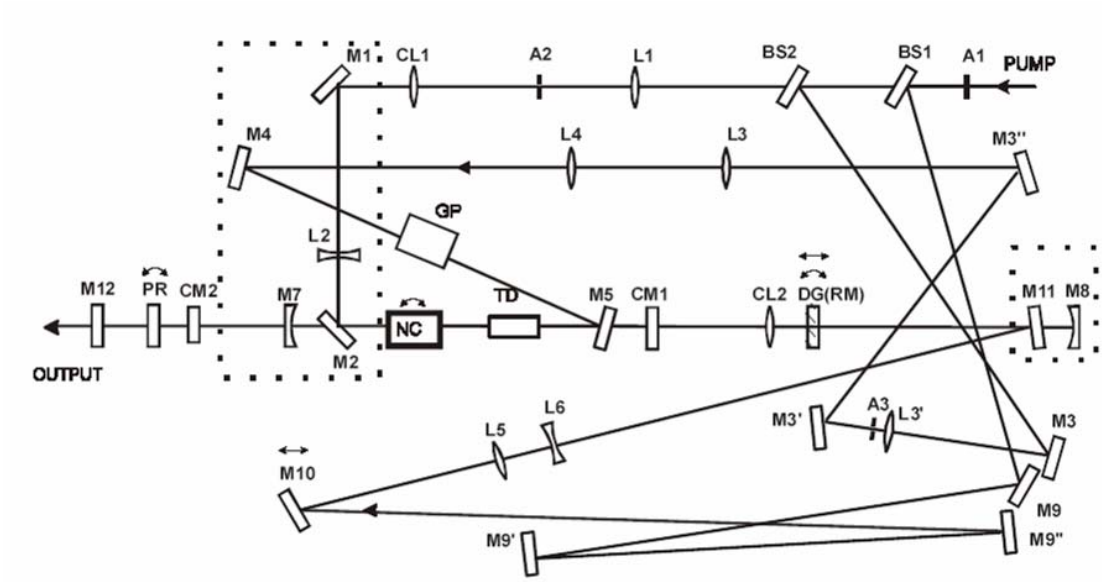

Figure 3-5: Top view of the TOPAS layout; A-aperture; BS-beamsplitter-L-lens; M-mirror; CL-cylindrical lens; CM-cylindrical mirror; NC-nonlinear crystal; DG-diffraction grating; GP-fused silica plate; TD-time delay; PR-polarization rotator

Wavelength tuning in the TOPAS is performed by the nonlinear crystal rotation. A change of the crystal orientation changes the indices of refraction of the crystal which reflects in the change of the photon momentum. The signal and idler wavelengths will vary such that both conservation of photon energy and momentum hold (phase-matching condition) [22]. The wavelength range covered by the signal and the idler is between 1150nm and 2200nm. We use further frequency mixers in order to achieve shorter wavelengths in the visible or near infrared by sum frequency of the pump and the idler (500nm-600nm), second harmonic of the signal (575nm-820nm) or second harmonic of the idler (735nm-1100nm). The TOPAS operation is computer-controlled after initial alignment and calibration.

Because type II phase-matching is used in the BBO crystal for generation of the parametric radiation, the signal and idler have perpendicular polarizations and therefore, they are easy to separate at the exit of the OPA. However, tuning the OPA on a broad range (for spectroscopy measurements), requires replacing of several polarization separators at the exit of the OPA which results in beam shifting and therefore, need of realignment, a time consuming process.

To make our experiments faster, we started using femtosecond WLC as tunable source. We have been already using it as a weak source in a pump-probe experiment [17] for non-degenerate nonlinearity measurements (the method is presented in the next chapter). This method still uses the OPA's, one to provide the pump wavelength, the other one to be used for continuum generation but there is no need to tune them during the experiment. A new technique introduced in Chapter 5 uses the Ti:Sapphire system only, to generate a high energy femtosecond WLC to be used as a tunable source for degenerate nonlinearity measurements.

CHAPTER 4: Z-SCAN AND PUMP-PROBE TECHNIQUES FOR NONLINEAR MATERIAL CHARACTERIZATION

The next two sections describe two of the techniques we use for nonlinear material characterization: Z-scan and WLC pump-probe. We used these methods for 2PA measurements of several common photoinitiators. These results are presented in the third section of this chapter.

4.1. Single Wavelength Z-Scan for Measuring Degenerate Nonlinearities

The Z-scan is a technique for measuring degenerate nonlinearities introduced by *M. Sheik-Bahae et al*. in 1990 [18]. In this technique, the transmittance through a nonlinear medium (sample) is measured as the sample travels through the focus of a Gaussian beam. Information on NLA will be obtained by collecting all the transmitted energy while the information about NLR is yielded by collecting the transmitted energy through an aperture centered on the beam in the far field. The Z-scan is a popular technique because of its simplicity, sensitivity, accuracy and ease of separation of NLA and NLR. These characteristics will be explained in this chapter.

The field of a Gaussian beam with no spatio-temporal distortions (e.g. pulse-front tilt which involves coupling between space and time domain [33]), traveling in the z direction can be written as:

$$E(z,r,t) = E_0(t)E(z,r) \tag{4.1}$$

where z is the distance from the focal point, r is the transverse coordinate and t is time.

$$E_0(t) = E_0 \exp\left(-\frac{t^2}{2\tau_0{}^2}\right) \tag{4.2}$$

describes the temporal field distribution at the focus, containing the temporal envelope of the laser Gaussian pulse (τ_0 –the pulse duration defined this way as HW1/eM of irradiance).

$$E(z,r) = \frac{w_0}{w(z)} \exp\left[-r^2 \left(\frac{1}{w^2(z)} + j\frac{k}{2R(z)} \right) - j\Phi(z,t) \right] \tag{4.3}$$

describes the spatial distribution of a focused Gaussian beam and satisfies the wave equation [34] where:

- w_0 is the beam waist defined as HW1/e^{2}M of irradiance
- $w(z) = w_0 \sqrt{1 + \frac{z^2}{z_0^2}}$ is the beam radius at a distance z away from the focus
- $z_0 = \frac{k w_0^2}{2}$ is the diffraction length; $k = \frac{2\pi}{\lambda}$ is the wave vector; λ-wavelength
- $R(z) = z\left(1 + \frac{z_0^2}{z^2}\right)$ is the radius of curvature of the wavefront; all defined in free space.
- $\Phi(z,t)$ denotes the field phase.

Consider the interaction of a focused Gaussian beam as the one defined by (4.1)-(4.3) with a nonlinear medium. Due to the nonlinear interaction, both the properties of the medium and the incident beam experience changes. We will discuss further the theory behind the Z-scan technique for the case where the interaction leads to third-order NLA (2PA) and NLR. For Z-scan measurements of higher order nonlinear effects, the reader should consult Reference [35].

The evolution of a field inducing 2PA and 3rd order NLR in a nonlinear medium was discussed in the Section 2.3 of Chapter 2. It was shown that if changes in the field amplitude are small over length scales similar to a wavelength (so the SVEA can apply) and if the transverse

coordinates of the field amplitude due to diffraction can be neglected then, the equations for amplitude/irradiance and phase propagation can be separated and written as:

$$\begin{cases} I(L) = \dfrac{I(0)e^{-\alpha L}}{1+\beta I(0)L_{eff}} \\ \Delta\Phi(L) = \dfrac{k\gamma}{\beta}\ln\left[1+\beta I(0)L_{eff}\right] \end{cases} \tag{4.4}$$

where L is the length of the sample, α – the linear absorption coefficient, β – the 2PA coefficient, λ – the wavelength in free space, $k=2\pi/\lambda$, $L_{eff} = \dfrac{1-e^{-\alpha L}}{\alpha}$ and $I(0)$ – the irradiance in front of the sample, $I(L)$ – the irradiance at the exit surface of the sample, $\Delta\Phi(L)$ – the phase accumulated after propagating a distance L in the sample. For simplicity, the reflection losses from the sample surfaces were neglected.

A sufficiently thin sample needs to be used for the diffraction or nonlinear refraction to have a negligible effect on the transverse field distribution during propagation within the sample. The medium of thickness L is regarded as "thin" provided that $L \ll n_0 z_0$ so that changes in beam diameter due to linear diffraction are negligible and additionally that $L \ll n_0 z_0/\Delta\Phi(0)$ so that changes due to diffraction resulting from nonlinear refraction may also be neglected. This condition is referred to as the "*thin sample approximation*". The Z-scan method was extended for thick samples also [36] but, this is not a subject of this work as "thin sample" conditions were fulfilled in all the experiments reported here.

In the Z-scan technique, the sample is translated through the focus of the Gaussian beam in the z direction so, the irradiance at the exit surface is different for different z positions with respect to the focus. As a result, the equations (4.4) are written as follows:

$$\begin{cases} I_e(z,r,t) = \dfrac{I(z,r,t)e^{-\alpha L}}{1+q(z,r,t)} \\ \Delta\Phi_e(z,r,t) = \dfrac{k\gamma}{\beta}\ln\left[1+q(z,r,t)\right] \end{cases} \tag{4.5}$$

where $q(z,r,t)=\beta I(z,r,t)L_{eff}$ (z – the sample position); e stands for exit and denotes the fact that the irradiance $I_e(z,r,t)$ and $\Delta\Phi$ (z,r,t) and the accumulated phase are at the exit surface of the sample. The variables r and t were included as the transverse distribution of the irradiance (and consequently of the phase) is different for different z positions and at different times. This should not be confused with the assumption regarding the neglecting of the field transversal component in the sample. The variable r is different for different z positions but is not changed by the beam diffraction in the sample.

The complex field amplitude at the exit of the sample contains a magnitude affected by 2PA and a term including the accumulated nonlinear phase after propagation through the sample:

$$E_e(z,r,t) = \sqrt{I_e(z,r,t)}e^{j\Delta\Phi_e} = E(z,r,t)e^{-\frac{\alpha L}{2}}\left[1+q(z,r,t)\right]^{\left(j\frac{k\gamma}{\beta}-\frac{1}{2}\right)} \tag{4.6}$$

Pure 2PA

We notice from the expression above, if all the energy transmitted through the sample is detected, the information about the change in phase, and consequently about the nonlinear refraction, is lost. By collecting all the energy one can get information about the 2PA only. The total transmitted power can be obtained by integrating the first equation of the (4.5) system at z over r:

$$P(z,t) = P_0(t)e^{-\alpha L}\frac{\ln\left[1+q_0(z,t)\right]}{q_0(z,t)} \tag{4.7}$$

where $P_0(t) = I_0(t)\frac{\pi w_0^{\ 2}}{2}$, $I_0(t)$ – the on-axis irradiance at focus (i.e. z=0), $q_0(z,t) = \beta I_0(t) L_{eff} /(1 + z^2 / z_0^{\ 2})$. The total energy detected at distance z is obtained by integrating (4.7) for a temporally Gaussian pulse:

$$
\begin{aligned}
E(z) &= \int_{-\infty}^{\infty} I_0(0) e^{-\frac{t^2}{\tau_0^{\ 2}}} \frac{\pi w_0^{\ 2}}{2} e^{-\alpha L} \frac{\ln[1 + q_0(z,0) e^{-\frac{t^2}{\tau_0^{\ 2}}}]}{q_0(z,0) e^{-\frac{t^2}{\tau_0^{\ 2}}}} dt \\
&= \int_{-\infty}^{\infty} \frac{2E_0}{\pi^{3/2} w_0^{\ 2} \tau_0} e^{-\frac{t^2}{\tau_0^{\ 2}}} \frac{\pi w_0^{\ 2}}{2} e^{-\alpha L} \frac{\ln[1 + q_0(z,0) e^{-\frac{t^2}{\tau_0^{\ 2}}}]}{q_0(z,0) e^{-\frac{t^2}{\tau_0^{\ 2}}}} dt \qquad (4.8) \\
&= E_0 e^{-\alpha L} \int_{-\infty}^{\infty} \frac{\ln[1 + q_0(z,0) e^{-t^2}]}{\sqrt{\pi} q_0(z,0)} dt
\end{aligned}
$$

where $I_0(t) = I_0(0) e^{-t^2}$

and $I_0(0) = \frac{2E_0}{\pi^{3/2} w_o^{\ 2} \tau}$; E_0 - the input energy;

The last equality in Eq. (4.8) was obtained by a change of variable $t/t_0 \rightarrow t$.

The normalized energy transmittance will be given by:

$$
T(z) = \frac{1}{\sqrt{\pi} q_0(z,0)} \int_{-\infty}^{\infty} \ln[1 + q_0(z,0) e^{-t^2}] dt \qquad (4.9)
$$

A typical 2PA transmittance curve is presented in Fig. 4-1 .

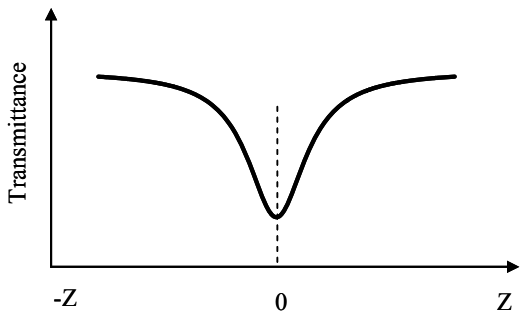

Figure 4-1: Typical 2PA ("open aperture" Z-scan) curve

The transmittance curve shown above is a result of what it is called an "*open aperture*" Z-scan because all the transmitted energy is collected as the sample travels through the focus of the Gaussian beam.

Pure NLR

Since the phase distortion is transformed to an amplitude distortion during propagation from the sample to the far field, placing an aperture centered on the beam in the far field in front of a detector causes the detector to be sensitive to the phase distortion. This experiment is referred to as "*closed aperture*" Z-scan. As the sample moves from a distance far from the focus (negative z) towards the focus the irradiance increases, leading to self-lensing in the sample. Positive/negative self-lensing prior to focus will tend to broaden/narrow the beam at the aperture, which results in a decrease/increase in the measured transmittance. As the sample passes the focal plane to the right (positive z) the same self-focusing/defocusing decreases/increases the beam divergence, leading to beam narrowing/broadening at the aperture and thus an increase/decrease in the measured transmittance. Therefore, a pre-focal transmittance maximum (peak) followed by a post-focal transmittance minimum (valley) is the Z-scan signature of a

negative refractive nonlinearity while a positive refractive nonlinearity will correspond to a reversed (valley-peak) Z-scan signature [18]. The nonlinearity sign is determined in this way.

Eq. (2.57), derived in Chapter 2: $\frac{d\Phi(z)}{dz} = \gamma k_0 I(z)$, describes the phase evolution through a sample exhibiting third-order nonlinear refraction and/or 2PA contained in the irradiance term. If 2PA is negligible, eq. (2.57) is solved to give the phase shift ΔΦ(t) at the exit surface of the sample.

$$\Delta\Phi(t) = \gamma k_0 I_0(t) L_{eff} \tag{4.10}$$

where $I_0(t)$ – is the on-axis irradiance at focus, as defined above. The phase shift varies as it propagates in the z direction and follows the radial variation of the incident irradiance at a given position z of the sample:

$$\Delta\Phi(z,r,t) = \frac{\Delta\Phi_0(t)}{1+z^2/z_0^{\,2}} \exp\left(-\frac{2r^2}{w^2(z)}\right) \tag{4.11}$$

The electric field exiting the sample will contain the nonlinear phase distortion:

$$E_e(z,r,t) = E(z,r,t)e^{-\alpha L/2} e^{j\Delta\Phi(z,r,t)} \tag{4.12}$$

$E_e(z,r,t)$ will be propagated to the aperture by applying the "Gaussian decomposition" method [37] in which the complex electric field at the exit plane is decomposed into a summation of Gaussian beams through a Taylor series expansion of the nonlinear phase term $e^{j\Delta\Phi(z,r,t)}$ in (4.12) [18]. The expansion is made around $j\Delta\Phi(z,r,t)$ and is valid if $|\Delta\Phi(z,r,t)|<1$.

$$e^{j\Delta\Phi(z,r,t)} = \sum_{m=0}^{\infty} \frac{\left[j\Delta\Phi(z,t)\right]^m}{m!} e^{-2mr^2/w^2(z)} \tag{4.13}$$

Each Gaussian beam can be propagated (after Eq. (4.3) description) to the aperture plane where they are resumed to reconstruct the beam. A spatially integration of the reconstructed field up to the aperture radius r_a will give the transmitted power through the aperture:

$$P_T(\Delta\Phi(t)) = c\varepsilon_0 n_0 \pi \int_0^{r_a} \left|E_a(r,t)\right|^2 r dr \tag{4.14}$$

The normalized energy transmittance is obtained by temporal integration over the pulse duration of the above expression and of the instantaneous input power $P_0(t)$ defined above in this discussion.

$$T(z) = \frac{\int_{-\infty}^{\infty} P_T(\Delta\Phi_0(t))dt}{S\int_{-\infty}^{\infty} P_0(t)dt} \tag{4.15}$$

where S is the aperture linear transmittance.

Typical "closed aperture" Z-scan curves corresponding to positive/negative nonlinearities are showed in Fig.4-2.

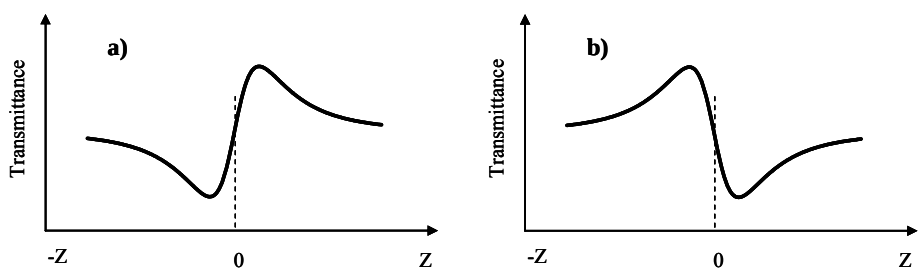

Figure 4-2: Typical NLR ("closed aperture" Z-scan) curves corresponding to a) positive and b) negative nonlinearity

The peak and valley occur at the same distance with respect to focus, ≈ $0.86z_0$ [18]. Therefore, the separation between peak and valley

$$\Delta Z_{p\text{-}v} \approx 1.7 z_0 \tag{4.16}$$

gives a quick evaluation of the z_0 value.

Both 2PA and NLR present

If 2PA and NLR are both present, the nonlinear phase given by the second equation (4.5) will be involved in the Gaussian decomposition in Eq. (4.6) of the field at the exit surface of the sample affected by 2PA and NLR. In Eq. (4.6) :

$$E_e(z,r,t) = \sqrt{I_e(z,r,t)}e^{j\Delta\Phi_e} = E(z,r,t)e^{-\frac{\alpha L}{2}}\left[1+q(z,r,t)\right]^{\left(j\frac{k\gamma}{\beta}-\frac{1}{2}\right)}$$

The term $\left[1+q(z,r,t)\right]^{\left(j\frac{k\gamma}{\beta}-\frac{1}{2}\right)}$ will be expanded by Taylor series around q(z,r,t) (if |q|<1)and the resulted field at the exit of the sample will be written as:

$$E_e(z,r,t) = E(z,r,t)e^{-\frac{\alpha L}{2}}\sum_{m=0}^{\infty}\frac{q(z,r,t)^m}{m!}\left[\prod_{n=0}\left(jk\gamma/\beta - 1/2 - n + 1\right)\right] \tag{4.17}$$

The complex field at the aperture plane can be represented by using the propagation equation (4.3), following the same procedure as the one described before for pure NLR.

It can be noticed the Gaussian decomposition method is a good approach for finding an analytical solution for small phase variations and/or small βIL values. This is a requirement easily met most of the times by using low irradiances but, sometimes, for instance, small NLR coefficient measurements require high irradiances which, for a large β, imply large βIL values. Consequently, the Gaussian decomposition method does not apply for a case like this and an analytical formula describing the normalized energy transmittance as the sample travel through the focused beam is not easy to be obtained. A numerical solution would solve this problem.

Examples of Z-scan curves generated by using a Matlab code [38] including both 2PA and NLR are shown in Fig.4-3.

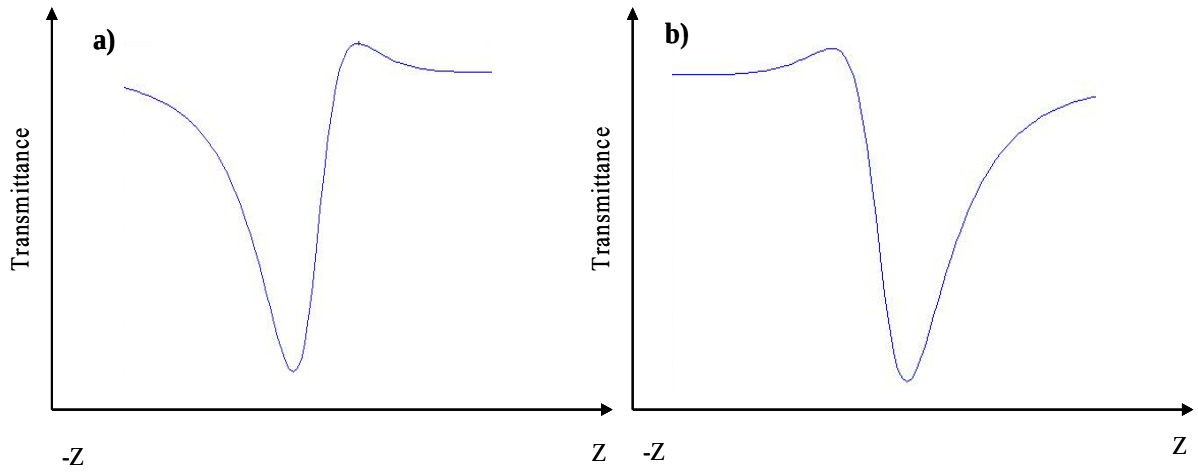

Figure 4-3: "Closed aperture" Z-scan curves including 2PA and NLR corresponding to a) positive and b) negative nonlinearity

It was shown [18] that for $q_0(0,0) \leq 1$ (condition met by adjusting the irradiance) and $\beta/2k\gamma \leq 1$ (valid in general, especially for a semiconductor), a division of the closed aperture Z-scan including both 2PA and NLR by the Z-scan curve including 2PA only will generate a Z-scan curve corresponding to a pure refractive index one. Again, this is very useful for small βIL values. For $\beta IL > 1$ the division does not work, therefore instead of the analytical solution given by Eq. (4.15) one should use the numerical code to fit the experimental "closed aperture" Z-scan curves which would include both 2PA and NLR.

A typical Z-scan set-up is presented in Fig.4-4.

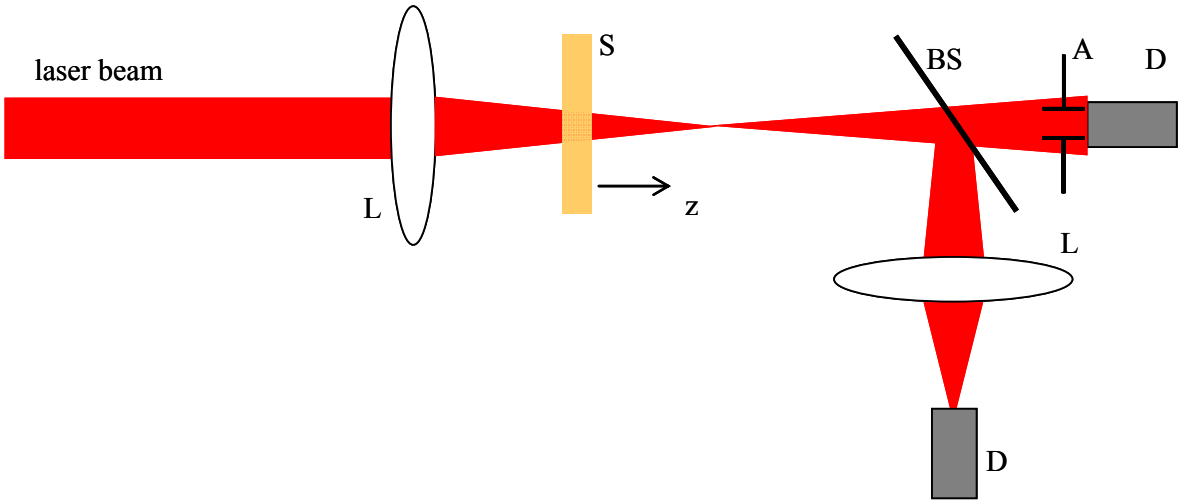

Figure 4-4: Single Wavelength Z-scan Experimental Set-up: L-lens; BS-beamsplitter; A-aperture; D-detector

Advantages of using the Z-scan

- As noticed in Fig. 4.4, a Z-scan *set-up* is a *simple* one.
- It gives the *absolute values of NLA and NLR* coefficients and also the *sign of the nonlinearity.*
- It is a *sensitive* technique. The shot-to-shot fluctuations of the laser source used determine the minimum measurable signal which can be distinguished from noise. In our case, average on a few hundred pulses and energy window on the detected signal allow us detecting measurable signals of ~1%. This way, in the thin sample approximation limit, a value of ~0.03 can be measured for βIL and ~0.016π (λ/125) for $\Delta\Phi_0$.
- Also, a *quick evaluation of the beam size* can be obtained from a "closed aperture" Z-scan by using the expression (4.16).

Disadvantages of using the Z-scan

- Care needs to be taken for distinguishing between different nonlinear processes. For example, the Z-scan cannot tell the difference between ESA from linear absorption and 2PA – or for 5th order, 3PA and 2PA + ESA. It also gets increasingly difficult to differentiate higher order responses like 5th and 7th. However, knowing the pump wavelength, the beam waist, the linear absorption spectrum of the measured sample and repeating Z-scan experiment for different energies and/or different pulsewidths one can differentiate between these effects. This would require also changing the equations for the field amplitude and phase propagation to include the excited state effects to properly analyze the experimental data [23, 24]. However, this was not an issue for the experiments presented in this work, as 2PA induced higher order effects did not occur in our experiments using femtosecond pulses (as explained in Chapter 2).
- A *high optical quality* sample is required for a Z-scan experiment. It has been shown [18] that the "parasitic" effects induced in a Z-scan transmittance curve by a poor quality sample can be reduced by subtracting a low-irradiance background Z-scan from a high-irradiance Z-scan.
- Mapping the entire degenerate 2PA/dispersion spectrum requires OPA wavelength tuning and realignment which are *time consuming* processes. WLC Z-scan introduced in the next chapter overcomes this disadvantage.

4.2. White-Light Continuum Pump-Probe for Measuring Non-Degenerate Nonlinearities

In this method a broadband, weak WLC pulse is used to probe a medium that is subjected to an intense pump pulse [17, 32]. The WLC pulse is generated in 2mm thick window of CaF, by focusing tightly 3-4μJ of 1300nm femtosecond pulses. We use two OPA's for this experiment, each of them a TOPAS as described in Chapter 3. The output of one of them, 1300nm is used for WLC generation while the output of the second one is used as a pump (strong) beam. The 2PA process requires simultaneous absorption of one photon from the pump and one from the probe beam. This implies both spatial and temporal overlapping of the two beams, pump and probe. Besides, the 2PA experienced by the pump or the probe needs to be avoided. Therefore, the pump wavelength is chosen to be outside the 2PA band edge of the measured sample while the probe irradiance is too small to induce 2PA. There are two important features of this interaction:

1) Generation of the WLC imposes chirp on the probe beam so that different probe frequencies arrive at the nonlinear sample at different time delays.

2) Probe and pump pulses travel with different velocities (group velocity mismatch) [17].

For these two reasons, the pump and the probe need to be delayed in time to get them overlapped in the sample. As the time delay is varied, the pump beam overlaps in time with a narrow spectral band of the continuum. The maximum of the 2PA signal in the spectral domain will identify the wavelength that has zero delay with respect to the pump. Data analysis will give the non-degenerate 2PA spectrum of the sample. The experimental set-up is shown in Fig.4-5.

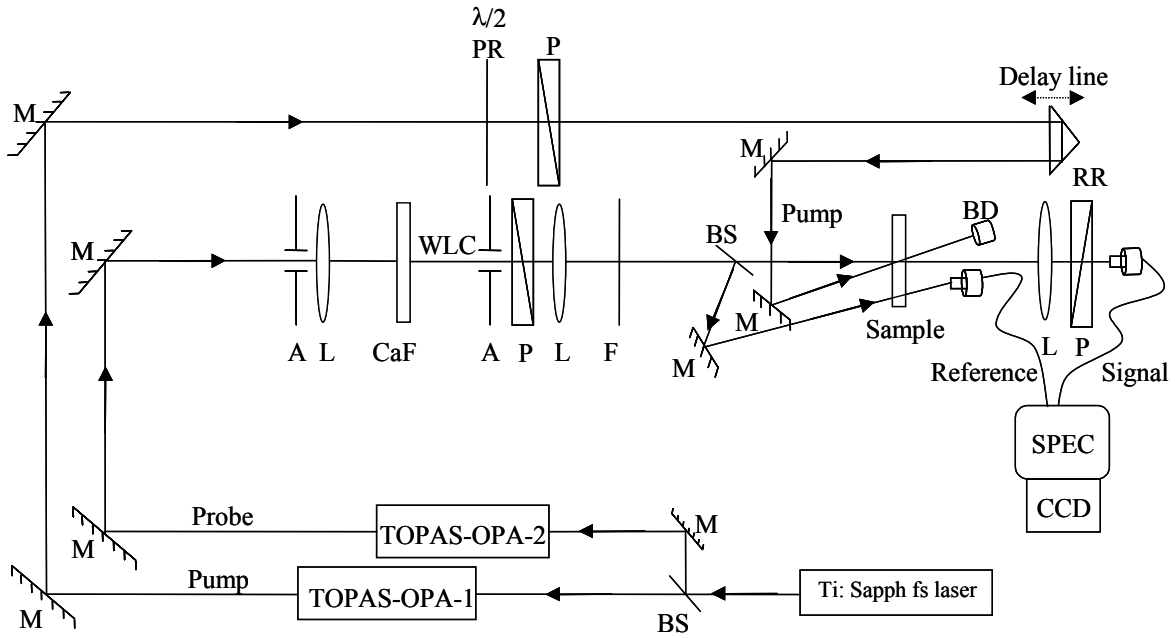

Figure 4-5: WLC Pump-Probe Set-up: M-mirror; L-lens; A-aperture; P-polarizer; PR-polarization rotator; RR-retro-reflector; NBF-dielectric short pass filter for blocking any remaining 1300 nm radiation

An example of using single-wavelength Z-scan and WLC pump probe for complete characterization of the 2PA spectra of materials is presented in the next section.

4.3. 2PA Measurements of Common Photoinitiators

The 2PA process, applied to photopolymerization, is a method used in applications such as the production of three-dimensional (3D) microstructures [9, 10] or optical data storage [11].

We have studied the 2PA properties of several common, commercially available photoinitiators using two nonlinear transmission spectroscopic methods, WLC pump-probe and Single Wavelength Z-scan [39]. Prior to this work, δ values on a limited number of conventional photoinitiators on the order of $<10 \times 10^{-50} cm^4$ sec per photon were reported [40]. Despite the low two-photon absorptivities, the general utility of a wide variety of conventional photoinitiators for the 2PA polymerization of acrylates and epoxide monomers [41,42] was demonstrated. As these initiators are in current and continual use, information on their 2PA properties may facilitate optimization of 2PA induced polymerization conditions.

The structures and the linear UV-visible absorption spectra (in MeOH) of all the photoinitiators studied are shown in Table 4-1 and Figure 4-6 respectively.

Table 4-1: Chemical structures of the photoinitiators

Irgacure Series		
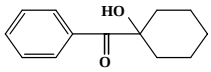 184	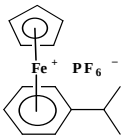 261	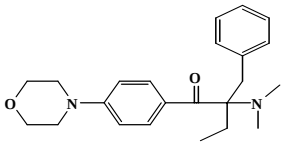 369
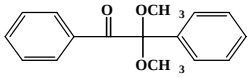 651	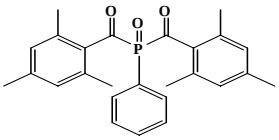 819	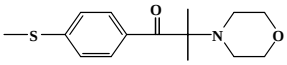 907
Darocure Series		
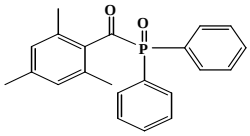 TPO	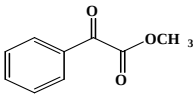 MBF	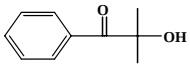 1173
CGI Series		
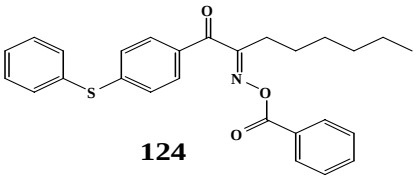 124	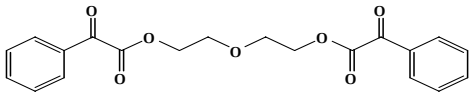 754	
Others		
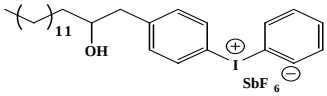 CD1012	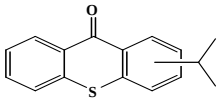 ITX	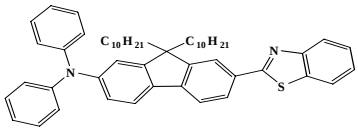 DPABz

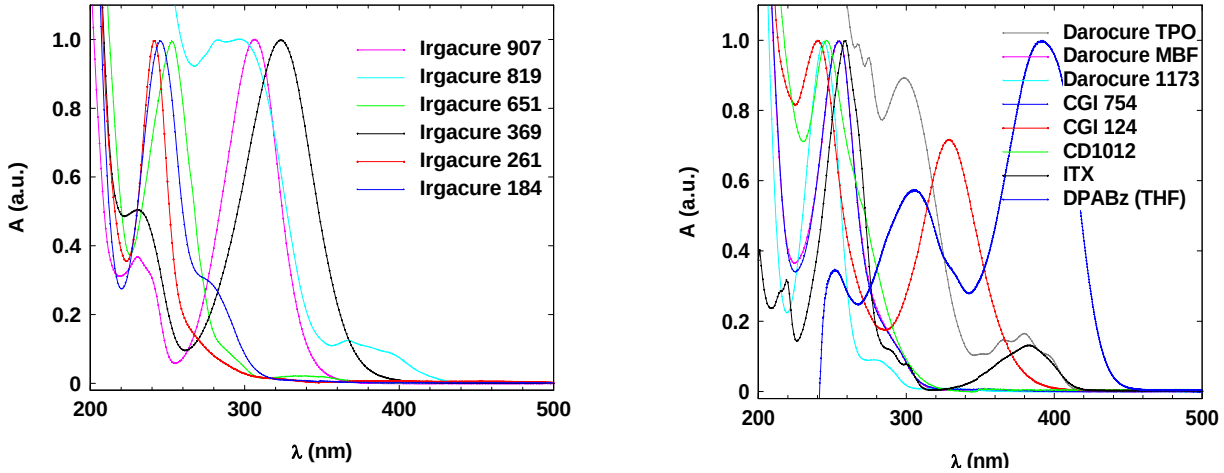

Figure 4-6: (left) Normalized UV-visible absorption spectra of Irgacure series photoinitiators in MeOH. (right) Normalized UV-visible absorption spectra of the Darocure and CGI series, CD1012, and ITX in MeOH. DPABz shown is in THF.

In this work [39], we used WLC pump-probe (measurements performed by Joel Hales in our group) and single wavelength Z-scan techniques to measure the 2PA cross-sections of the photoinitiators. We needed to use both techniques to be able to extract more information about these samples. On one hand, the lowest measurable cross-section corresponding to the WLC method is larger than that of the Z-scan method. Therefore, the samples for which the nonlinear signal was below a measurable threshold using the WLC method, were investigated using the Z-scan technique, a more sensitive method. On the other hand, the WLC pump-probe is a faster method than Z-scan. It was a great benefit that we found the nonlinear spectra (measured by WLC pump-probe) were nearly coincident with the linear spectra for each of the investigated compounds. This was not so surprising giving the asymmetry of the molecules; they must have also been asymmetric in charge density. This coincidence permitted us to use the Z-scan technique to measure only the peak 2PA cross-section for each of the compounds since

measuring the full degenerate 2PA spectrum via Z-scan can be quite time consuming. Measurements in the Z-scan geometry were performed to determine if the peak 2PA cross section was indeed a local maximum, and this turned out to be accurate in every case.

Figure 4-7 shows experimental 2PA spectra collected for three of the compounds (ITX, Irgacure 369, CGI 124) using the WLC and the aforementioned coincidence of the 2PA and the linear spectra which permitted us to use the Z-scan technique to measure only the peak 2PA cross-section for each of the compounds. The 2PA cross-sections (symbols) are given in Goppert-Mayer (GM) units, where 1 GM = 10^{-50} cm^4 sec/photon. These cross-sections were plotted versus the sum of the energies of the two photons involved in the non-degenerate process.

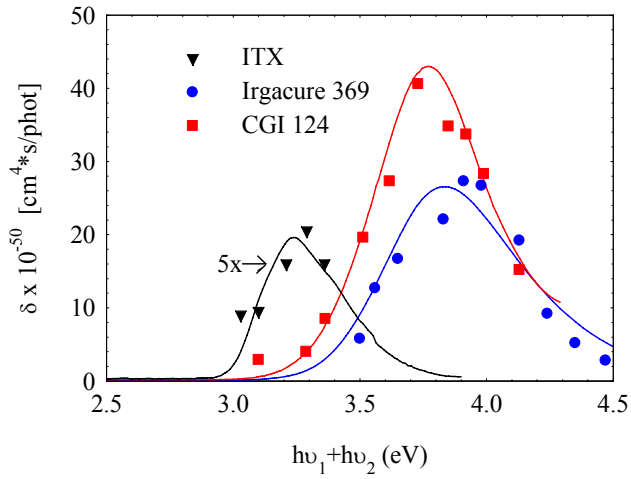

Figure 4-7: 2PA spectra via the WLC method. ITX spectrum has been enlarged (5x) for ease of viewing. Solid lines indicate UV-visible linear absorption spectra for the corresponding compounds.

The full results of the nonlinear characterization of the photoinitiators are summarized in Table 4-2. The first column denotes the peak wavelength (nm) of the linear absorption for each compound. The following two columns reflect the Z-scan results. $\lambda^{(2)}_{meas}$ is given by half the wavelength (nm) of the excitation light and δ_{meas} is the measured absorption cross-section given

in GM units. The WLC data is presented in the final two columns. $\lambda^{(2)}_{max}$ is the sum of the energies of the two photons involved in the WLC process expressed in wavelength (nm), i.e. $c/(\nu_1+\nu_2)$. δ_{max} is the peak 2PA cross-section measured by this method.

Table 4-2: Peak 2PA cross-sections for photoinitiators using Z-scan and WLC methods

		Z-Scan		**WLC-2PA**	
Compound	λ_{max}	$\lambda^{(2)}_{max}$	δ_{meas}	$\lambda^{(2)}_{max}$	δ_{meas}
Irgacure 184	246	265	23	250	<20
Irgacure 261	242	265	<20	250	<20
Irgacure 369	324	335	7.1[8.1]	318	27.3
Irgacure 651	254	265	28	250	<20
Irgacure 819	295	300	<4	300	<5
Irgacure 907	306	300	4.1	300	<5
Darocure TPO	299	300	<4	300	<5
Darocure MBF	255	265	27.5	250	<20
Darocure 1173	244	265	<20	250	<20
CGI 124	328	330	7.5[31]	330	38.5
CGI 754	253	265	21	250	9.9
CD1012	247	265	16	273	13.8
ITX	382	380	5	377	4.1
DPABz	390	-	-	388	120 (THF)

For the cases where the nonlinear signal is below the measurable threshold, an upper limit to the possible cross-section (i.e. <20 GM) is indicated. In the case of the Z-scan technique, just four of the compounds were not measurable (the lowest measurable cross-section corresponding to the Z-scan method is ~ four times smaller than that of the WLC pump-probe method). The error bars associated with the measured cross-sections for both methods range from 15-20%. Taking into account these error bars, as well as the lower limits imposed on some of the compounds, a good agreement between the two methods can be noticed. However, there were two samples for which discrepancies in the results were observed, Irgacure 369 and CGI 124.

Since 2PA is involved in the photoinitiating process investigated, it was a concern that during the measurement of the absorption cross-section, the molecule could photodegrade, which would in turn affect the observed cross-section. This should be more prevalent in the Z-scan technique where higher irradiances are used (50-400 GW/cm^2) compared to those used in the WLC method (<50 GW/cm^2). Furthermore, in the WLC method, the monitored change in the weak probe transmittance guarantees that the population promoted into the excited state is small compared to the Z-scan technique where the strong pump places a larger population in the excited state. Since the number of electrons promoted into the excited state dictates the amount of possible photoreaction, the Z-scan technique is more invasive than the WLC method. To investigate the effect of this potential photodegradation, Z-scan measurements were performed on solutions in an enclosed 1 mm path length cuvette as well as in a flow cell with a 1 mm path length. In the flow cell geometry the cell volume was approximately 300 μL and the flow rate was approximately 1.5 mL/sec. A sampling of these results is presented in Figure 4-8 where the symbols represent experimental data and the solid lines are their theoretical fittings.

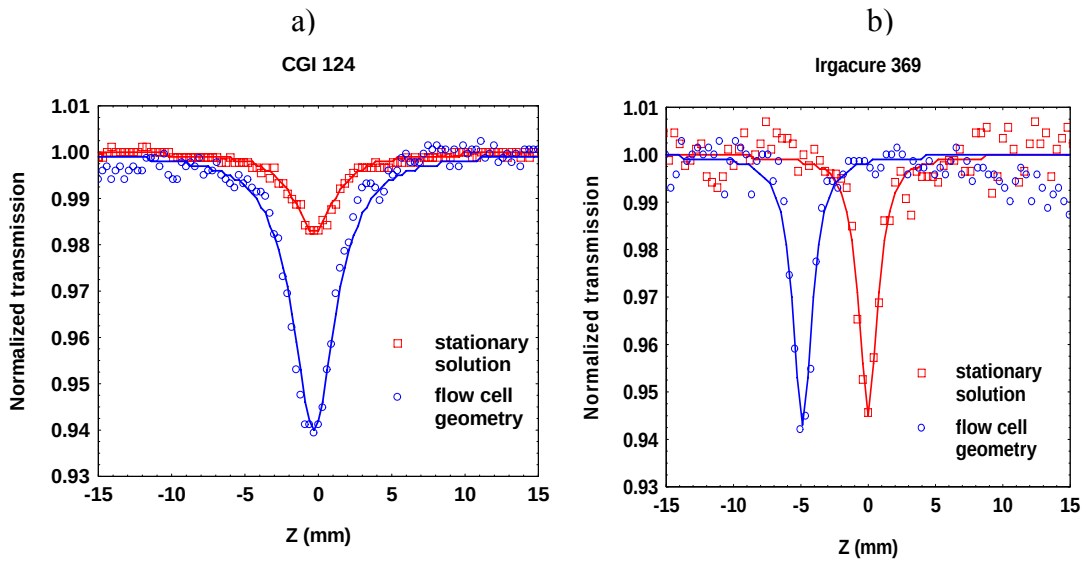

Figure 4-8: 2PA results via the Z-scan method for stationary cell and flow cell geometries. (a) CGI 124. (b) Irgacure 369

Figure 4-8(a) shows that the nonlinear signal from the flow cell geometry for CGI 124 was 3.5 times larger than the stationary solution. This implied that flowing the initiated sample out of the focal region allowed us to measure a fresh volume of solution during every shot. The flow cell data are the results presented in Table 4.2. Figure 4-8(b) indicates that data for the Irgacure 369 sample where the two curves are displaced for ease of viewing. It is apparent here that employing the flow cell geometry does not have a significant effect on the nonlinear signal. Therefore the remaining discrepancy between the WLC data and the Z-scan data for Irgacure 369 may point to a faster photodecomposition rate that we were not able to compensate for in our flow cell geometry. The flow cell results for CGI 124 and Iragure 369 are shown in parentheses above the initial results in Table 4-2.

CHAPTER 5: NEW TECHNIQUE FOR NONLINEAR MATERIAL CHARACTERIATION: WHITE-LIGHT CONTINUUM Z-SCAN

5.1. Motivation and Important Issues Regarding the Technique

Propagation of ultrashort laser pulses in transparent media can generate pulses whose spectral frequencies can range from the UV to the IR, a phenomenon known as *white-light continuum (WLC) generation* [43]. The resultant beam appears to the eye as a white spot surrounded by a colorful ring pattern or a blue rim depending on the power and irradiance of the input laser pulses [44]. Alfano and Shapiro were the first to report WLC generation by focusing powerful picosecond pulses in glass samples in 1970 [43]. The continuum they observed was extending from 400 to 700nm. A lot of work has been done since then in an effort to explain the WLC generation mechanisms and to generate and characterize different WLC sources for specific applications. A discussion regarding WLC generation and its use for nonlinear optical characterization will be given in the next paragraphs.

He et. al. were the first to demonstrate that, using only an intense WLC pulse, degenerate 2PA may be rapidly determined over a broad spectral range [45]. This was accomplished by monitoring the nonlinear transmission of the WLC through a chromophore solution. This produces a relative spectral curve which is subsequently converted to an absolute scale by calibration with an additional nonlinear transmission experiment performed using a separate single wavelength source. The WLC was spatially dispersed by using a glass prism to avoid the possibility of nondegenerate nonlinearities which will be discussed later in this dissertation. While this method is relatively rapid, it requires significant transmittance losses (low signal to

noise otherwise) and requires a separate reference to get an absolute calibration**.** In 2004, at nearly the same time as we introduced the WLC Z-scan (see below), the authors of reference [46] (one of them, Cleber Mendonça was a former postdoc in our group) introduced a similar technique that required a separate calibration but ignored the contributions of nondegenerate nonlinearities which we determined to be strong.

In the experimental technique we propose, the single wavelength source that is conventionally used in a Z-scan experiment is replaced with a WLC source. We refer to this method as WLC Z-scan. The well-established single wavelength Z-scan [18] as described previously in paragraph 4.1, is a popular technique because of its simplicity, sensitivity, accuracy and ease of separation of NLA and NLR. It is a rapid method to determine nonlinear coefficients for a particular wavelength, but obtaining a broad spectral dependence of the nonlinearity requires wavelength tuning and realignment which are often time consuming processes. Our new WLC Z-scan technique provides a rapid measurement of the degenerate nonlinearities of the sample under investigation and keeps the sensitivity of the conventional Z-scan.

There were two main issues we needed to address in doing this experiment:

1. *evaluation of the contribution of nondegenerate nonlinear effects*

Given that in this experiment a WLC source replaces the single wavelength source used in the conventional Z-scan technique, care has to be taken to check on the existence of nondegenerate contributions to the nonlinear response, i.e. from two different wavelengths. If this is significant, dispersive elements need to be used for minimizing the nondegenerate absorption/refraction processes. We will discuss this matter in detail in the next paragraph of this chapter where the experimental results are presented.

2. *generation of an intense, good spatial quality, broadband WLC*

WLC can be generated by using picosecond [43] or femtosecond pulses [47] in transparent media as solids [43], liquids [44], gases [48] and different types of waveguide structures such as silica optical fibers [49] and hollow optical waveguides [50]. Depending on the application for which one needs to use the WLC source, different pulsewidths and different transparent media can be used.

As far as our application is concerned, we needed to use the femtosecond pulses provided by our Ti:Sapphire laser system (described in Chapter 3) to generate an intense, good spatial quality, broadband WLC. This requires a proper transparent medium to be used for continuum generation. The next paragraphs of this chapter discuss the advantages and disadvantages of WLC generated in different nonlinear media and also review different mechanisms proposed so far to explain the WLC generation.

5.1.1. WLC generation in condensed media (solids and liquids)

A complete theory explaining the WLC generation in different transparent media is still lacking. Different mechanisms have been suggested so far. When, Alfano and Saphiro observed the continuum for the first time by focusing picosecond pulses into BK7 glass, they attributed the spectral broadening to a four-wave mixing process [43]. The same, Alfano and Saphiro observed self-modulation of the broadened spectra in their next experiments of WLC generation in calcite crystals which led them to identify the broadening mechanism as electronic self-phase modulation (SPM) [51]. SPM following self-focusing was believed to be the dominant mechanism for super-broadening [52] until Fork et al. obtained superbroadening by propagating

80fs pulses through 500μm liquid jets [47]. In their case, self-focusing was absent. Yang and Shen explained the result through self-steepening-enhanced SPM [53]. Brodeur and Chin considered that this model had a shortcoming by predicting a broader continuum in media with higher nonlinearity, a trend that is not observed [54] (for example continuum generated in water is among the broadest observed despite the low Kerr nonlinearity of water). SPM alone or self-steppening enhanced SPM can explain the broadening for particular cases like in the thin liquid jet experiment mentioned above or gas filled hollow fiber which will be discussed in Section 5.1.2 but in general, for extended media, a more complex mechanism for the continuum generation has been proposed and demonstrated by Brodeur and Chin [55,56]. They made a detailed investigation of femtosecond white-light continuum generation in transparent condensed media [55] and found that the continuum is triggered by self-focusing which at the critical power leads to a drastic increase in irradiance which enhances SPM. In their theory, the self-focusing is limited by free electrons generated by multiphoton excitation (MPE). Free electrons induce a negative change in the index of refraction which for a certain value of the electron density cancels the change in the Kerr refractive index and the self-focusing stops. For femtosecond pulses, self-focusing can also be stopped by group velocity dispersion (GVD) [57,58] by temporal stretching of the pulse. As a result of self-focusing counteracted by the free electrons generated through MPE and/or by the GVD, the beam is confined spatially, a behavior that is termed "filamentation". If the power of the focused beam is just above the WLC threshold power, only one filament with a Gaussian beam profile at all wavelengths is observed [59]. If higher powers are used, the beam breaks up into multiple filaments due to small-scale self-focusing [44].

As far as our WLC Z-scan experiment is concerned, we need to stay in the one filament regime as we need the WLC beam to have a good spatial profile quality. The condition of the single filament regime will impose a limit on the input power and thus, on the energy available in the continuum source. To make our technique useful, the method has to be able to measure the nonlinear properties of materials with small as well as large nonlinearities, which requires high spectral energy densities (or spectral irradiance) for the WLC.

A promising possibility investigated next is to use a WLC generated in hollow fibers filled with noble gases which appears to exhibit both high spectral energy densities and good spatial properties [60].

5.1.2. WLC generation in hollow fiber filled with noble gases

A hollow fiber is defined in the most general terms as a small diameter glass capillary tube. There are several advantages of using a noble gas confined by a hollow fiber as a nonlinear medium for WLC generation instead of a bulk medium [61].

- the same spot size can be maintained along the entire fiber length, thereby enhancing the nonlinear effects. In a bulk material, a tight focusing necessary to obtain high irradiance would limit the interaction length.
- a hollow fiber can handle higher energy pulses than a bulk material. If the irradiance is too high in a bulk material avalanche ionization occurs which leads to damage and destroys the transmission and spatial beam quality.
- it has been shown [62] that by proper mode matching between the input beam at the fiber entrance and the capillary radius, single mode propagation through the fiber can be obtained.

Thus, a hollow fiber combines the good spatial properties of guided (single mode) beam propagation with the capability to handle high energy pulses [60]. This is true only for very straight fibers, i.e. no bends.

In addition, the use of noble gases as the nonlinear medium in a hollow fiber offers several important advantages compared to bulk materials and optical fibers [61]:

-noble gases exhibit a high threshold irradiance for multiphoton/avalanche ionization especially for femtosecond pulses compared to bulk material

-the third-order nonlinearity is purely electronic if the pressure is not too high (thus, the Raman effect is not significant in hollow core fibers)

-the strength of the nonlinearity can be controlled by changing the gas type and its pressure.

Propagation along hollow fibers can be thought of as occurring through grazing incidence reflections at the dielectric inner surface. It was shown [62] that by proper mode matching (i.e., $w_0/a \approx 2/3$, where w_0 is the spot size at the fiber entrance and a is the capillary radius), 98% of the incident energy is contained in the fundamental EH_{11} hybrid mode, whose intensity profile as a function of the radial coordinate r is given by $I(r) = I_0 J_0^2 (2.405r/a)$, where I_0 is the peak irradiance, and J_0 is the zero-order Bessel function. For the same mode, the real (β-phase constant) and imaginary (α/2 ~field attenuation constant) parts of the propagation constant are given by [50]:

$$\beta = \frac{2\pi}{\lambda}\left[1 - \frac{1}{2}\left(\frac{2.405\lambda}{2\pi a}\right)^2\right]$$
$$\frac{\alpha}{2} = \left(\frac{2.405}{2\pi}\right)^2 \frac{\lambda^2}{2a^3}\frac{\upsilon^2+1}{\sqrt{\upsilon^2-1}} \tag{5.1}$$

where λ is the laser wavelength in the gas medium and υ is the ratio between the refractive indices of the external (fused silica) and internal (gas) media.

To maintain the propagation of the fundamental mode along the hollow fiber, the incident peak power needs to be kept below the critical power around which the self-focusing becomes significant. The reason is that in the mode picture the effects of self-focusing manifest as a radiation exchange between the eigenmodes [63]. This condition will impose an upper limit on the gas pressure of [64]:

$$p_{\max} = 0.15\frac{\lambda^2}{\kappa_2 P_0} \tag{5.2}$$

where P_0 is the pulse peak power and $\kappa_2 = n_2/p$ is a pressure independent gas characteristic constant (n_2-the nonlinear refractive index of the gas, p-the gas pressure).

In the absence of dispersion and self-focusing the maximum broadening δ_{max} after a length l, for Gaussian pulses, is given by [65]:

$$\delta\omega_{\max} = 0.86\gamma P_0 z_{eff} / \tau_0 \tag{5.3}$$

where τ_0-the pulsewidth (HW1/eM in irradiance), $z_{eff}=[1-\exp(-\alpha l)]/\alpha$ (α given by Eq. 5.1 above), $\gamma=n_2\omega_0/cA_{eff}$, ω_0-the laser central frequency, A_{eff}-the effective mode area.

As it will be shown in the paragraph describing the experimental results, our experimental spectral broadening is a few times smaller than that theoretically predicted. *Nisoli et. al.,* who observed the same discrepancy, attributed it to the uncertainty of the quoted n_2 values for different gases, especially for femtosecond pulses [50].

In Reference 64, the authors make a detailed analysis of the parameters needed to be varied to optimize the spectral broadening of WLC pulses obtained by propagation of femtosecond pulses through a hollow fiber. They show that the spectral broadening is limited by an upper limit imposed on the input peak power (an increase of the input peak power would produce multiphoton/avalanche ionization at the entrance of the fiber) and on the gas pressure (to avoid self focusing and light coupling into higher modes as the relation (5.2) also shows). The authors propose the use of two hollow fibers, separated by a temporal compression stage (cascading hollow fibers) to be able to increase the spectral broadening of the WLC pulse.

We did not try in our experiments the cascaded hollow fiber solution for the WLC spectral broadening increase. Instead, we removed the hollow fiber and generated the continuum in a chamber filled with noble gas with no guiding element as it has been reported that a beam above a certain critical power level may be trapped into a single filament instead of spreading by diffraction [66-69]. This worked well as discussed below.

5.1.3. WLC generation in gases (no guiding element)

Corkum and Rolland were the first to report on continuum generation from gases [48, 70]. They propagated 70fs and 2ps pulses into a 90cm long cell filled with different gases, CO_2, N_2, Ar, Kr, Xe at high pressure (up to a few tens of atmospheres) and got a continuum spanning at least 400nm. The irradiance used was right above the continuum generation threshold and the divergence of the continuum was larger than the divergence of the input beam, thus, the generated WLC beam was not a self-trapped one. For self-trapped filaments to occur a process halting the self-focusing and allowing the pulse to propagate without spreading must be involved.

Two mechanisms were proposed to explain self-trapped filaments. The first assumes self-channeling of high peak power pulses as a result of a balance between two competing nonlinear effects: self-focusing induced by the Kerr effect and self-defocusing induced by plasma generation once the multiphoton ionization threshold of the gas is reached [68, 71]. The second interpretation is based on the moving-focus model [72]. In its simplest version assuming an instantaneous Kerr effect, different time slices of the pulse have different irradiance and are self-focused at different points along the axis [56,72]. Plasma generation halts the self-focusing in this model too, but the mechanism is explained differently from the previous model. In this model, an apparent intense confined mode corresponds to the time-integrated detection of the different focal points along the propagation axis [69]. It has been shown [56, 72] that the beam pattern consists of a strong tiny spot (the filament) surrounded by a weaker background with a much larger diameter. The filament itself contains about 10% of the total energy, while most of the energy is located in the background. *Mlejeck et al.* were the first to introduce the

background/energy reservoir concept [73]. They predicted by theoretical simulations that the large-scale weak background extends the filament by providing energy to the central spot at different positions along the focus [72, 73]. *Liu et al* [74] then demonstrated the existence of the background reservoir and its role in long distance propagation of femtosecond pulses in gases. In a simple experiment they blocked the background using a pinhole and let only the central filament to pass through. The filamentation was immediately stopped after the pinhole indicating that the filament cannot survive without the background reservoir. This is the most accepted explanation for filamentation in air/gases, so far. There are two important issues regarding the filamentation. The first one concerns the generation of the filament (details about mechanisms explaining it were mentioned above) while the second one regards its propagation distance. It has been shown that a filament generated by a collimated beam would propagate over a distance comparable with the Rayleigh range [68, 72] while a filament generated by a loosely focused beam propagates over much longer distances [69].

As a conclusion drawn from the literature published so far on the subject, a powerful femtosecond laser pulse propagating in air/gases self-transforms into a chirped whitelight laser pulse because of self-focusing, filamentation, self-phase modulation, and self-steepening [56]. The maximum distance over which such a pulse will propagate as a high peak intensity beam could possibly be of the order of many kilometres. Measurement of that distance is a current experimental challenge with interesting applications [75].

Details on the WLC generated in a chamber filled with noble gas will be presented later in this chapter along with the experimental results using this WLC source.

5.2. Experiments

The laser source we use in all the following experiments is our Ti:Sapphire laser system producing ~0.8mJ, ~150 fs, 775nm pulses at 1kHz repetition rate as described in Chapter 3.

We focus the femtosecond laser pulses provided by this system in different nonlinear media for continuum generation. The main purpose is to obtain a stable, broad, high energy, and good spatial quality WLC source for nonlinear material characterization. WLC generation using different nonlinear media and experiments using this source will be presented in the next sections.

5.2.1. WLC Z-scan using WLC generated in distilled water

In the first WLC Z-scan experiment we performed [76], we used WLC generated in distilled water.

For WLC generation, we focused ~10μJ of the 775nm, 150fs beam with an f=15 cm lens into a 3 cm long cell filled with distilled water. This generated a WLC with sufficient energy at many wavelengths suitable for performing Z-scans. A short-pass filter was used to remove the 775 nm pump and the infrared part of the continuum. The spectrum of the WLC after passing through the low-pass filter is shown in Fig.5-1.

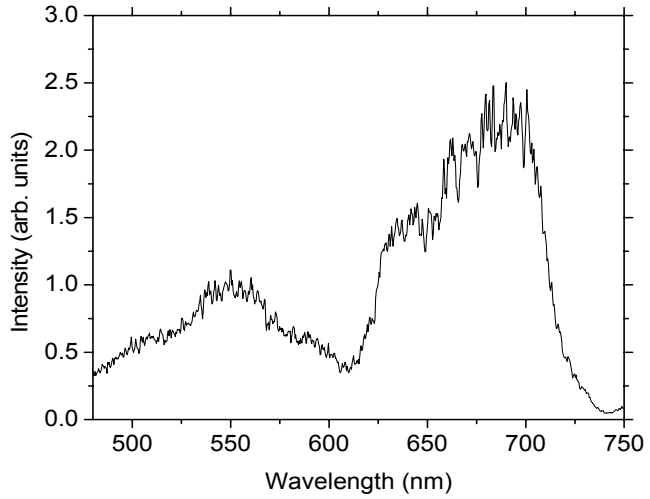

Figure 5-1: WLC spectrum after passing through the low-pass filter

As mentioned previously, for performing a Z-scan experiment, we need to make sure the WLC generation is in the single filament regime; multi-filament generation would make a Z-scan experiment impossible due to a poor and unpredictable spatial profile. We checked for this experimentally by translating a CCD camera through the focal point where we performed the Z-scan experiment. We found the white light to be in a single beam for the power levels at which we performed the Z-scans. However, at much higher powers we did notice that the white light was composed of multiple beams.

Knowledge of the energy, beam waist, and pulse duration for each spectral component of the WLC source is necessary for a Z-scan experiment.

We used narrow band filters (NBF) of ~10 nm full-width at half maximum (FWHM) bandwidth to characterize the energy in the continuum as a function of wavelength. The energies measured were in the range of 10 pJ/nm-25 nJ/nm over the range 650 nm - 900 nm.

To determine the spatial characteristics of the WLC, a knife-edge technique was used to measure the beam waist of different wavelengths in the continuum. These wavelengths were selected by using NBF in the WLC path.

To ascertain temporal features of the WLC, we performed an Optical Kerr Gate measurement (OKG) [47,77]. OKG is a pump-probe experiment in which an instantaneous nonlinear effect (Optical Kerr effect in our case) is used to generate a cross-correlation signal. A strong beam (pump) is used to induce anisotropy of the refractive index of a sample (Kerr medium); the induced anisotropy changes the polarization of the WLC beam (probe); and the probe transmittance through a crossed polarizer/analyzer pair is monitored by a detector system. The pump and the probe are delayed with respect to each other such that at different delays the pump will interact with different "colors" of the continuum. Different cross-correlation signals for each continuum spectral component (~10nm window) are measured this way. From the width of the cross-correlation traces, the pulsewidth for different spectral components of the continuum can be estimated. A detailed description of OKG experiments for WLC characterization can be found in Reference 32.

With knowledge of the energy, beam waist, and pulse duration for each spectral component of the WLC source, we were ready to proceed with the Z-scan experiments.

In order to confirm the validity of the WLC Z-scan technique we chose to measure the 2PA spectrum of ZnSe. ZnSe was selected since its 2PA spectrum has been well documented in the literature [18,78]. The thickness of the sample was 0.5mm which along with the fact that relatively low irradiance was used, guaranteed that the thin sample approximation was valid [18]. In order to make the distinction between degenerate and nondegenerate nonlinearities, the 2PA spectrum of ZnSe was measured at specific wavelengths in the presence of and in the absence of the entire broadband WLC source.

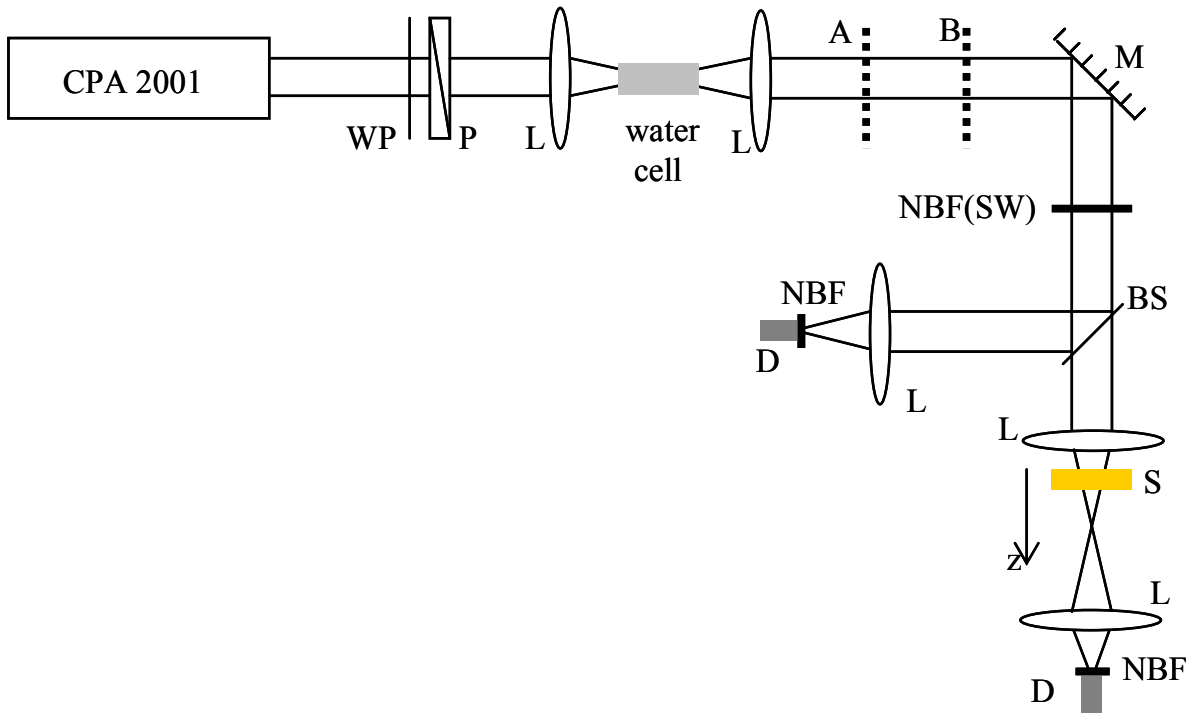

Figure 5-2: WLC Z-scan experimental setup. CPA-2001-femtosecond source; WP-waveplate; P-polarizer; L-lens; GP-glass prism; M-mirror; NBF-narrow band filter; BS-beamsplitter; S-sample; D-detector. A and B denote the positions of additional elements inserted in the set-up. NBF(SW) is used only in the single wavelength configuration discussed in the text with the other two NBF's removed

The experimental setup is depicted in Fig. 5-2. In the first experiment, we used the WLC without any external dispersive elements in the beam. As in a single wavelength Z-scan, the WLC beam is focused and the transmittance of the nonlinear sample is monitored as it is scanned along the beam axis through the focal region while the energy in the WLC is held constant. The WLC was stable, but to avoid any possible fluctuations we used an "energy window" on the reference detector (i.e. accepted data only if the reference energy was within a specified energy range-usually an energy window of ±5% being used). However, the difference between data taken with and without this window was not significant. We took data averaging over 500 shots. Since we

are interested first in measurements of NLA only, the transmission detector collected the entire beam. The transmittance of the WLC through the sample was monitored at different wavelengths by placing a narrow band filter (NBF) at a particular wavelength in front of each detector. The Z-scan was then repeated for additional wavelengths in order to build up the 2PA spectrum. Figure 5-3 (a) shows a Z-scan trace and the corresponding value of the effective 2PA coefficient (β) [18, 78] obtained for one of the wavelengths, 650nm, i.e. this fit assumes that the only effect responsible for the NLA is frequency degenerate 2PA. The fitted curve uses the focused beam size measured by the knife-edge scans. The curve appears narrower than the experimental data and the value of β obtained is much larger than extrapolated from prior measurements at other wavelengths [78].

The most likely reason for these discrepancies is that since the entire WLC is passing through the sample, other wavelengths can affect the transmission of the detected wavelength through nondegenerate processes such as nondegenerate 2PA, resulting in measurement of an erroneously high 2PA coefficient. The large width of the Z-scan curve may again be due to the nondegenerate 2PA along with chromatic aberration which causes different wavelengths to focus in different planes. We also found considerable variation in focal spot size at different wavelengths from the knife-edge scans.

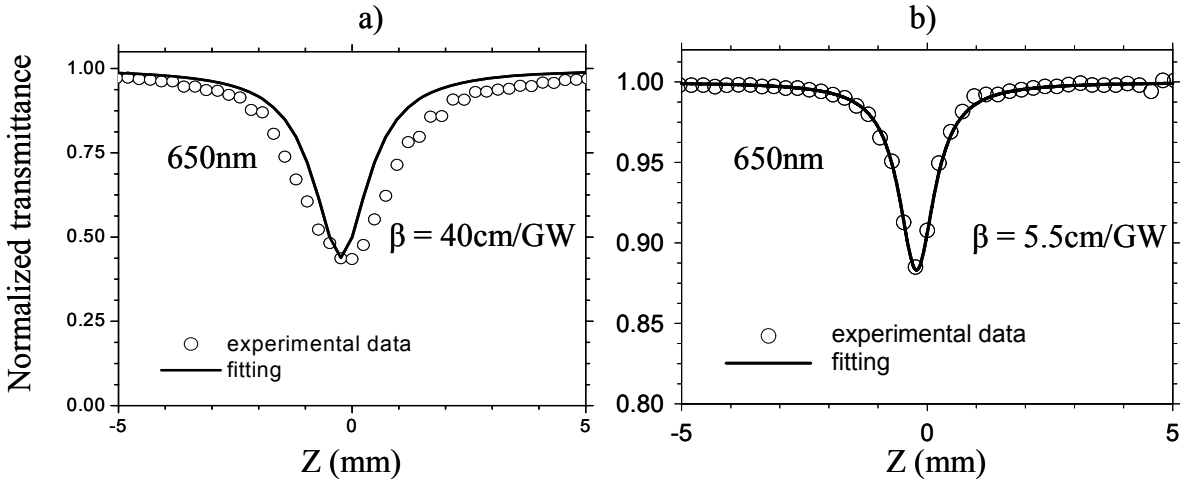

Figure 5-3: Normalized Z-scan transmittances of ZnSe measured at 650nm for a) the WLC configuration and b) the SW configuration. The solid lines represent fittings used to extract β values

To verify that nondegenerate 2PA was occurring, we compared the values of the 2PA coefficients extracted from Z-scan curves in the WLC configuration with those obtained from single-wavelength Z-scan experiments performed at the same wavelengths. For the single wavelength Z-scan experiments a narrow band filter was placed in the WLC path before the sample, creating a quasi-monochromatic beam. Again, by changing the narrow-band filters and repeating the Z-scan, a spectrum of 2PA could be obtained. Because a NBF placed in the WLC path before the sample infers a single wavelength (SW) experiment, denoted as NBF(SW) in Fig. 5-2. This experimental arrangement will be referred to as the "SW configuration" while the one for which the NBFs are placed in front of the detectors is referred to as the "WLC configuration". Figure 5-3 (b) shows the experimental data and the corresponding β for the SW Z-scan configuration using the same wavelength as in Fig. 5-3 (a). This data gives a better fit and a 2PA coefficient in close agreement with values previously reported in the literature [78].

From the comparison of Fig. 5-3(a) and 5-3(b), we attribute the discrepancy between the two values of β to the nondegenerate 2PA processes induced in the WLC configuration due to the spatial and partial temporal overlapping between adjacent wavelengths. The temporal overlap is only partial because of the temporal dispersion of frequency components of the WLC caused by the group velocity dispersion GVD induced by the generating medium, here water.

5.2.1.1 Spatial and Temporal Separation of the WLC wavelengths

To avoid these nondegenerate nonlinearities, wavelengths need to be either temporally or spatially dispersed prior to entering the sample.

To temporally disperse the WLC, we placed a thick piece of ZnSe (7 mm) in the WLC at the position labeled A in Fig. 5-2. ZnSe possesses large GVD in the visible which imposes a large temporal dispersion on the WLC. The GVD also increases the pulsewidth but for our 180 fs input pulsewidths (determined from an OKG experiment as previously mentioned), the effect of pulsewidth broadening is less significant than the temporal separation of the wavelengths. However, we had to account for this pulse broadening, which resulted in 211 fs at 800 nm to 247 fs at 670 nm, in order to calculate the irradiance needed to fit the 2PA coefficient to the data at each wavelength. The broadenings were estimated by using the formula for GVD broadening of a Gaussian pulse [65]:

$$\tau(L) = \tau_0 \sqrt{1 + \frac{L^2}{L_D{}^2}}$$

where τ_0 is the initial pulsewidth, L is the propagation distance (7mm-the length of the ZnSe sample in our case) and $L_D=\tau_0^2/k_2$ the dispersion length ($k_2 = \frac{\lambda^3}{2\pi c}\frac{d^2n}{d\lambda^2}$ -the GVD parameter).

Figures 5-4 (a) and 5-4 (b) show Z-scan traces taken in both WLC and SW Z-scan configurations respectively, at a wavelength of 670 nm. The discrepancy between the value of the 2PA coefficient extracted from the WLC experiment and the one obtained in the SW Z-scan experiment is less severe than in the first experiment but it is still significant, implying that the temporal dispersion imposed by the 7-mm ZnSe was insufficient, i.e., multiple wavelengths still overlap in time leading to nondegenerate 2PA.

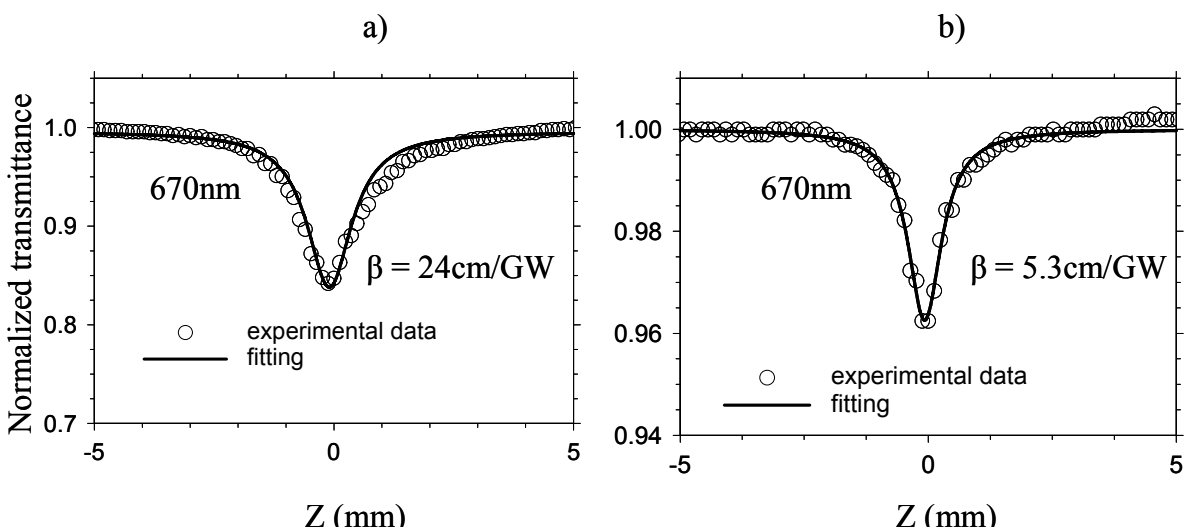

Figure 5-4: Normalized Z-scan transmittance of ZnSe measured at 670nm with the WLC beam temporally dispersed. The solid lines represent fittings used to extract β values a) WLC configuration, b) SW configuration

In the next experiment the wavelengths in the WLC were spatially dispersed by a glass prism [45] at position B in Fig. 5-2. We repeated the same experiment for different wavelengths and in both configurations. This time, the values of the 2PA coefficients obtained from the fittings for the two configurations were even closer than before (within a factor of 3), suggesting that the spatial separation is more effective than its temporal counterpart in this particular configuration but nonetheless the separation is still insufficient.

Finally, we combined both the ZnSe for temporal dispersion and the glass prism for spatial dispersion in one experiment. Figure 5-5 (a) and 5-5 (b) show Z-scan curves taken at 670nm in the WLC and the SW configurations.

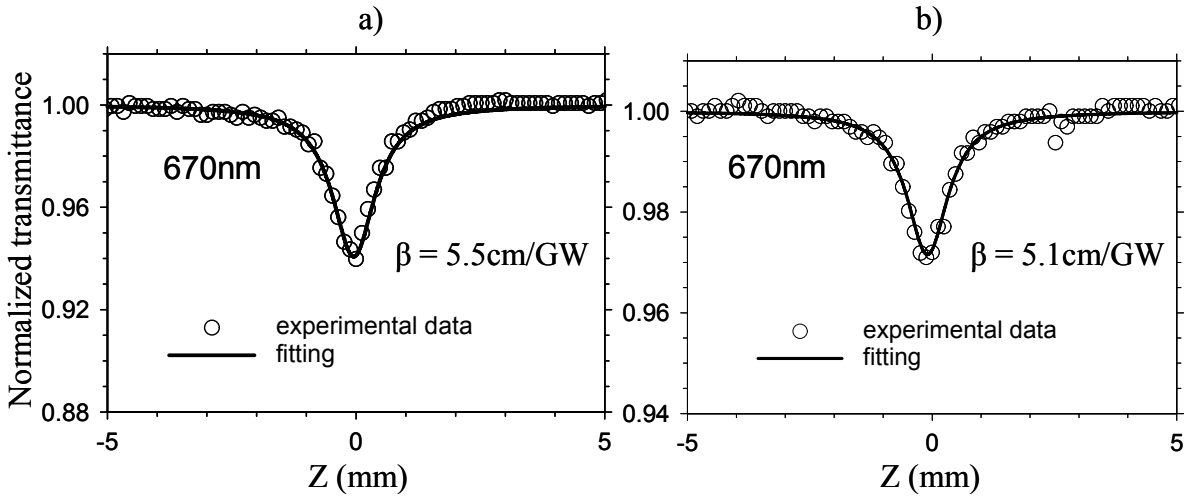

Figure 5-5: Normalized Z-scan transmittance of ZnSe measured at 670nm with the WLC beam temporally and spatially dispersed. The solid lines represent fittings used to extract β values a) WLC configuration, b) SW configuration

This time, we obtained agreement within experimental uncertainties between the values of β in the two experiments. We interpreted this to show that the wavelength separation was

sufficient to make the contributions from nondegenerate 2PA negligible such that the WLC Z-scan truly measures the degenerate 2PA spectrum. Figure 5-6 shows Z-scan curves taken for this experimental arrangement in the WLC configuration for different wavelengths. The transmission curves correspond to five different wavelengths sampled by the narrow band filters placed directly before the detectors. The solid lines represent fittings [18] of the experimental curves used to extract values of β.

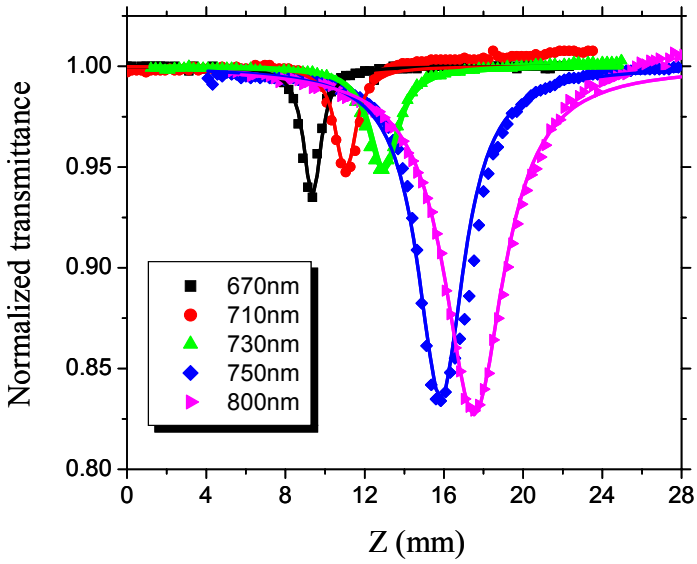

Figure 5-6: Normalized Z-scan transmittance of ZnSe measured at different wavelengths with the WLC beam temporally and spatially dispersed. The solid lines represent fittings used to extract β values. Z-scan traces are shifted from their original positions for an easier view

These values show reasonable agreement with the values obtained from theory [78] as presented in Fig. 5-7, further confirming the validity of our method for obtaining degenerate nonlinearities.

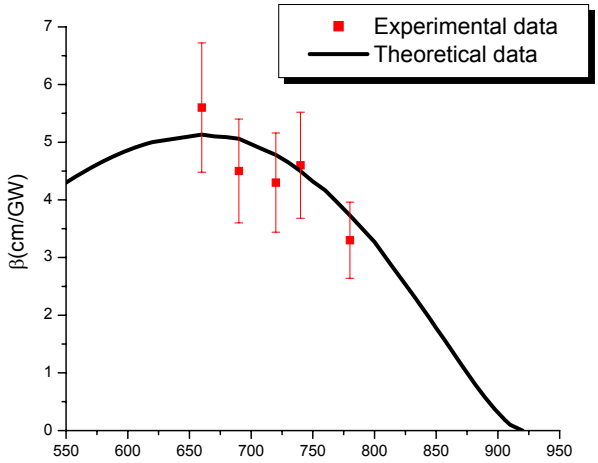

Figure 5-7: 2PA coefficient, β, values obtained from theory and from the experimental data fittings

This experiment demonstrated the potential of this technique for rapidly determining the degenerate nonlinear absorption spectrum of a sample.

Next, we demonstrated that the method can be extended to the "closed aperture" Z-scan for NLR measurements. As in the previous 2PA measurements, simultaneous NLR measurements at all wavelengths would also require separation of the wavelengths to minimize nondegenerate nonlinearities. However, spatial separation presents difficulties in using the aperture needed for closed aperture Z-scans. Temporal dispersion of the continuum can broaden the pulses and may significantly reduce the irradiance, thus weakening the nonlinear signal. We used an alternative approach for both NLA and NLR, where we spectrally separated the WLC wavelengths prior to the sample [79].

5.2.1.2 Spectral Separation of the WLC wavelengths

To achieve the spectral separation prior to the sample we used a narrow band linear variable filter (LVF) manufactured by Ocean Optics, Inc.[80]. This acts as a bandpass filter with spatially-varying center wavelength. The bandpass width can also be varied. Ocean Optics made this filter by fastening together a spatially varying low-pass and high-pass filters (interference coatings applied on quartz substrates) as Fig.5-8 shows.

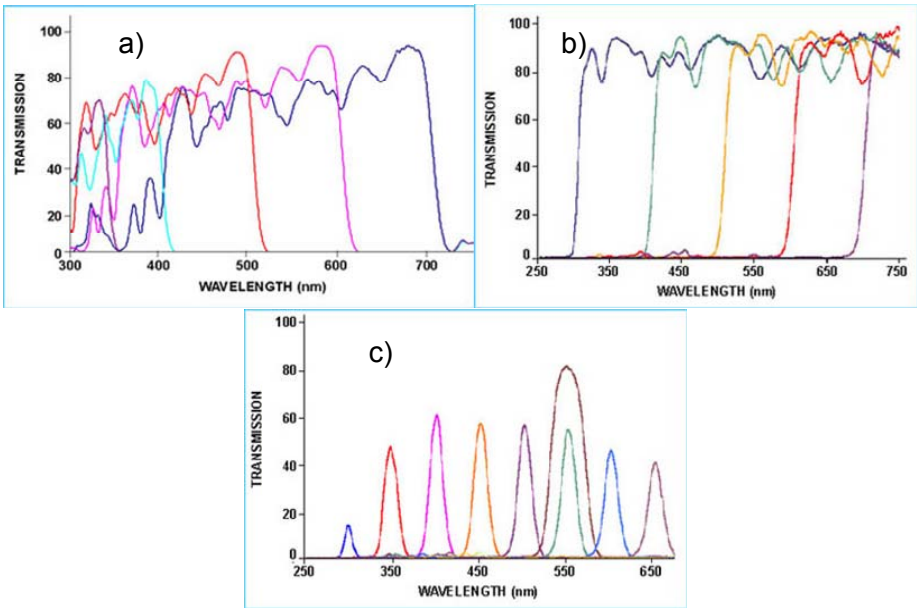

Figure 5-8: a) low-pass filter spectra at different position along its length b) high pass filter spectra at different position along its length c) spectra obtained by fastening together a low-pass and high-pass filter taken at different position along its length

Figure 5-9 shows an image of these linear variable filters.

Figure 5-9: Linear variable filters manufactured by Ocean Optics

By focusing the white-light beam on the LVF we were able to obtain a transmitted beam having a spectral bandwidth of 12-15 nm (FWHM) over the wavelength range 500 to 710 nm.

To obtain Z-scans over this wavelength range, we scanned the full wavelength range at each Z-position by translating the LVF through the beam. The sample was translated along Z after each wavelength scan, and the process was repeated until the entire Z-scan was obtained. In practice, we used two computer driven translation stages and, at the 1 kHz laser pulse repetition rate, averaging 500 pulses per data point, a single experiment took ~8 minutes to give the full spectrum of NLA and full dispersion of NLR. The experimental setup is shown in Fig. 5-10.

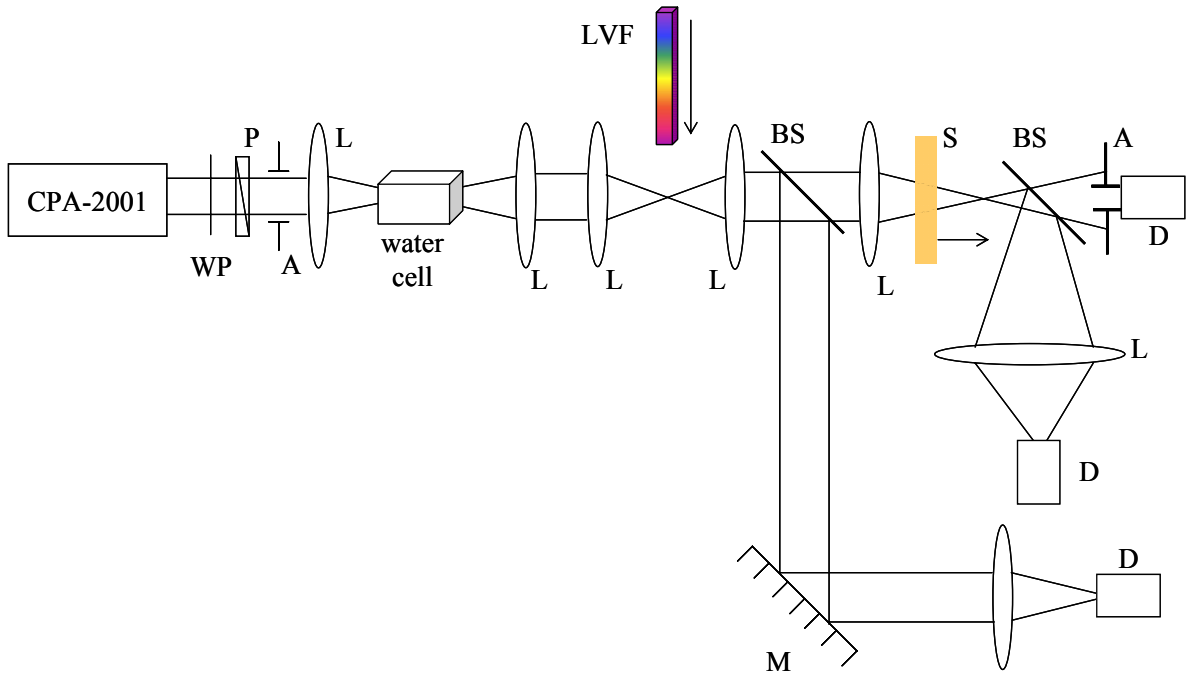

Figure 5-10: WLC Z-scan experimental setup. CPA-2001-femtosecond laser source; WP-waveplate; P-polarizer; L-lens; LVF-linear variable filter; M-mirror; BS-beamsplitter; S-sample; A-aperture; D-detector

After the WLC beam was focused onto the LVF, the single wavelength beam transmitted by the LVF was approximately recollimated, then divided by a beamsplitter into a reference arm and a signal arm. After focusing the beam through the sample, we used a second beamsplitter, to split the transmitted beam into two arms. On one arm, we used a lens to collect all the energy on the detector ("open aperture" Z-scan). On the other arm we placed an aperture for partial collection of the energy ("closed aperture" Z-scan). Nonlinear absorption coefficients are extracted from the transmission curves obtained in the open aperture experimental arm. The experimental curves obtained in the closed aperture arm contain information about both nonlinear absorption and nonlinear refraction. As shown in reference [18] and discussed in Chapter 4, for small signals,

the separation of the nonlinear refraction from 2PA can be done by dividing the closed aperture normalized Z-scan by the open aperture one.

As mentioned previously, to fit the Z-scan transmission curves corresponding to open [18] and closed [81] apertures, we need to know the energy, the beam waist and the pulsewidth for each spectral component. The energies measured were in the range of 0.3 -2 nJ over the range 500 nm - 710 nm. We determined the beam waist for different wavelengths transmitted by the LVF by using the knife-edge scanning technique. For pulsewidth measurements we used an OKG experiment [32,77]. The Kerr medium used in our experiment was a 1mm thick cell filled with CCl_4 (CCl_4 was chosen because it is a symmetric molecule for which the "instantaneous" response that follows the intensity profile of the laser pulse cross-correlation dominates [82]). From the width of the cross-correlation traces we were able to determine the pulsewidth for different wavelengths transmitted by the LVF. The value determined was ~165 fs FWHM in the range 500 nm – 750 nm.

In order to test this technique we measured the 2PA spectrum and the associated bound electronic n_2 dispersion in ZnSe. Again, we chose ZnSe since it is well documented in the literature [18,78,83]. The thickness of the sample was 2.0 mm for which the thin sample approximation for diffraction is valid [18]. However, ZnSe has large group velocity dispersion (GVD) and we must account for GVD-induced pulsewidth broadening as the pulse passes through the ZnSe sample. To measure the effect of the GVD on the pulsewidth in the ZnSe, we repeated the OKG experiment with the sample placed in the WLC path. This revealed that the broadening was significant, increasing the pulsewidth from 165 fs FWHM to 260 fs at 710 nm and from 165 fs to 400 fs at 560 nm.

To analyze the Z-scan we used the average of the pulsewidths measured without and with the ZnSe (corresponding respectively to the pulsewidths at the front and the back of the sample). We compared the experimental values of pulsewidth after the ZnSe sample with those obtained from the following theoretical calculation. Considering the pulse entering the sample to be linearly up-chirped (as the pulse travels through optics' materials of normal dispersion), we can calculate the chirp parameter from its spectral width (determined from the spectrometer) and its pulsewidth (obtained from the OKG measurements). The value of the pulsewidth within the sample corresponding to each wavelength was calculated by taking into account the GVD induced pulse broadening. This was used to calculate the average pulsewidth within the sample, which agrees with the experimental result within ~7% but always smaller. Hence for the Z-scan data analysis, we used the calculated average pulsewidth multiplied by 1.07 for all wavelengths.

The experimental Z-scan curves (open aperture and its corresponding divided closed aperture Z-scan) are shown in Fig.5-11 for two different wavelengths.

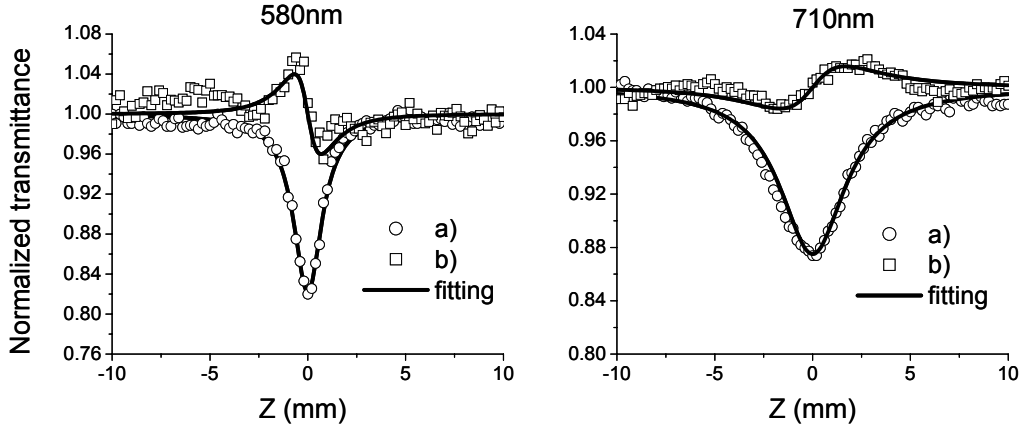

Figure 5-11: Z-scan data at 580nm and 710nm a) open aperture and b) closed aperture (the result of the division with open aperture). Here each data point is the average of 500 pulses

The solid lines represent fits [18, 81] to the experimental curves used to extract values of the 2PA coefficient, β (from the open-aperture Z-scan curves) and the values of the nonlinear refractive index, n_2 (from the closed-aperture Z-scan curves). We notice that n_2 changes sign from negative at 580 nm to positive at 710 nm, as predicted by theory in Reference 83. To our knowledge, this is the first time the sign change of n_2 around 0.7 of the energy bandgap has been demonstrated for a single material by tuning the wavelength. The values of β and n_2 obtained from fits at different wavelengths are presented in Fig. 5-12 along with the theoretical predictions of references 78 and 83. The β values have an estimated experimental error of approximately ±20%. The errors for n_2 values are between ±30% and ±80%, the larger errors corresponding to the n_2 values close to zero.

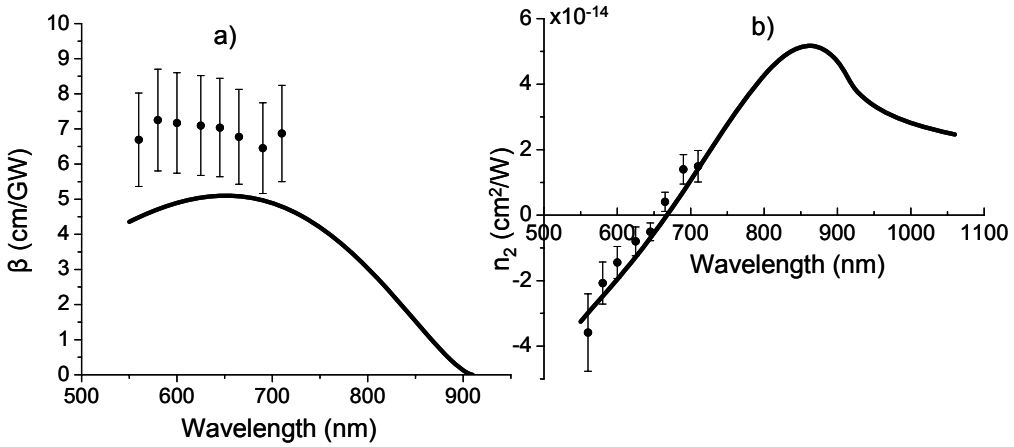

Figure 5-12: a) 2PA coefficient and b) nonlinear refractive index coefficient obtained from theory and from the experimental data fittings

These results demonstrate the WLC Z-scan is a rapid method for characterization of a material's degenerate nonlinear absorption spectrum and the dispersion of its nonlinear refraction. Extension of this technique to materials with considerably smaller nonlinearities requires higher spectral energy densities for the WLC. High energy WLC sources generated in condensed media have already been demonstrated [84], but unfortunately, above a certain threshold, the beam breaks into small filaments making a Z-scan experiment impossible. An example of filaments generated by propagating 775 nm fs pulses, 140μJ (the output of our Ti:Sapphire laser) in a 10cm long BaF_2 crystal is shown in Fig. 5-13. We were unable to obtain high energy single filaments in this material.

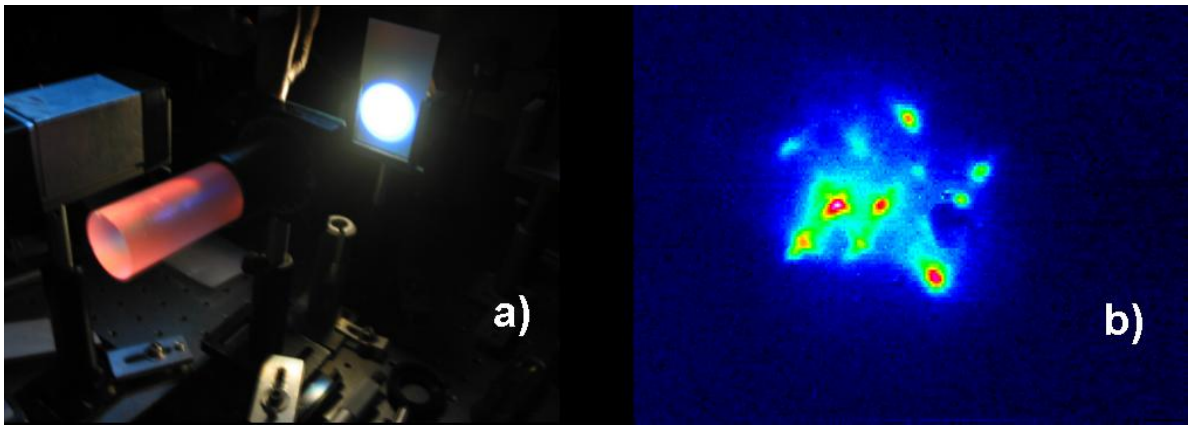

Figure 5-13: a) WLC generated in 10cm long BaF_2 crystal b) filaments generated by focusing 140 μJ, 775nm beam into the BaF_2 crystal

As explained in the previous section, a promising possibility to obtain a WLC source exhibiting both high spectral energy densities and good spatial properties was to use hollow fibers filled with noble gas for continuum generation [60].

5.2.2. WLC Z-scan using WLC generated in hollow fiber filled with noble gases

In our experiment, we used a 45cm long hollow fiber (a thick wall flexible fused silica capillary tubing made by Polymicro Technologies) with 150 μm inner diameter and 665 μm outer diameter. The thick wall is coated with a polyamide. Figure 5-14 shows an image of the hollow fiber taken under the microscope.

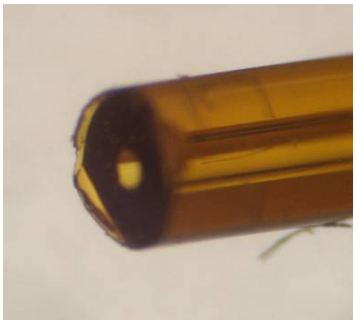

Figure 5-14: Thick wall capillary tubing made by Polymicro Technologies

A high pressure stainless steel gas chamber was prepared with a V-groove made in an aluminum bar in which the fiber was placed. The gas chamber was built with fused silica windows on each end. The chamber was filled with noble gases (argon and krypton) at different pressures. The beam was focused into the hollow fiber by a 35 cm focal length lens which gave a beam waist of ~ 50 μm (HW1/e^2M of intensity). This size was used to best match the size of the fiber as discussed in section 5.1.2. Figure 5-15 shows a picture of the chamber holding the fiber and the schematic representation of the hollow glass capillary inside the fiber.

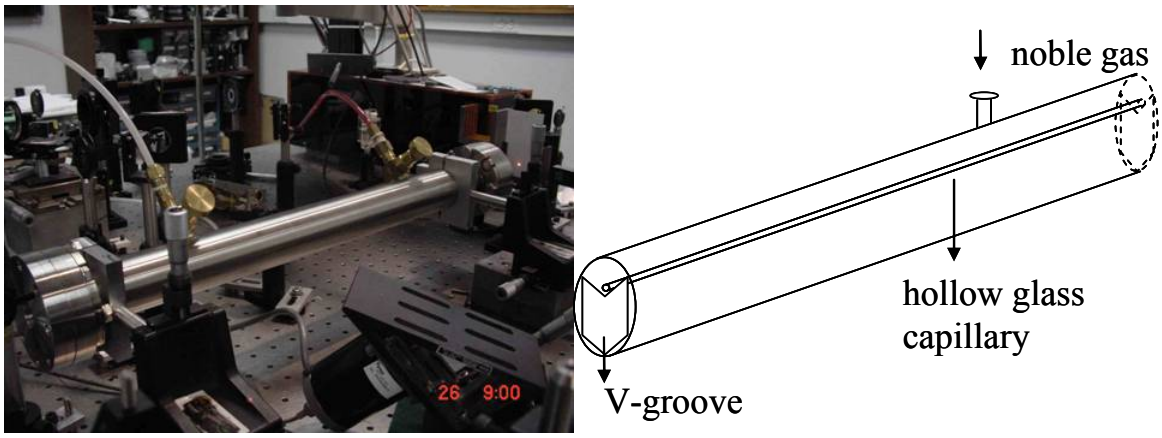

a) b)

Figure 5-15: a) Stainless steel chamber holding the hollow fiber; b) schematic representation of the hollow glass capillary tubing inside the chamber

We used argon and krypton as noble gases for WLC generation. Xe could have been another choice. We did not have it available at the time these experiments were performed as it took several months to get it. We will use it later in experiments described in Section 5.2.3. The corresponding output spectra obtained by using these gases are showed in Fig. 5-16, below.

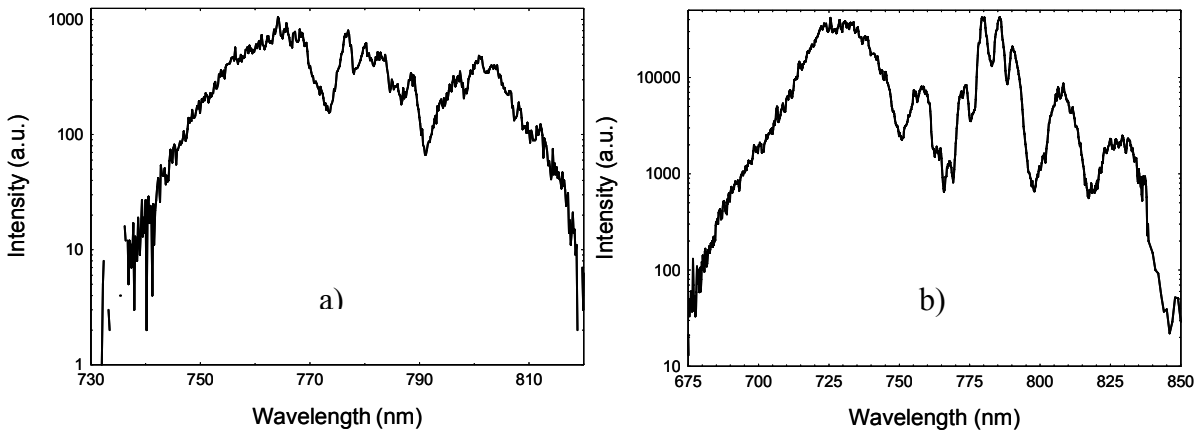

Figure 5-16: Output spectrum from a hollow fiber filled with a) Ar and b) Kr

The spectra exhibit amplitude modulations which are characteristic of a pure self-phase modulation process. The peak powers used were 1.3 GW for Ar and 1.1 GW for Kr. If we assume the nonlinear index coefficients for Ar and Kr to be $n_2/p=9.8\cdot10^{-24}$ $m^2/W\cdot atm$ and respectively, $n_2/p=2.78\cdot10^{-23}$ $m^2/W\cdot atm$ [85], the critical powers for self-focusing ($P_{cr}=0.15\lambda^2/n_2$) turn out to be 2.3 GW for Ar at 4 atm and 1.2 GW for Kr at 2.7 atm. The peak powers used were kept below the self-focusing critical powers to avoid the transfer of energy from fundamental mode to higher order modes along the fiber [63].

In the absence of dispersion and self focusing the maximum broadening δ_{max} after a length l, for Gaussian pulses, is given by [65]: $\delta\omega_{\max} = 0.86\gamma P_0 z_{eff} / \tau_0$ as mentioned previously in Section 5.1.2 (equation 5.3) where τ_0-the pulsewidth (HW1/eM in irradiance), z_{eff}=[1-exp(-αl)]/α (α given by equation 5.1, Section 5.1.2), P_0 -the peak power and $\gamma=n_2\omega_0/cA_{eff}$, n_2-the nonlinear refractive index, ω_0-the laser central frequency, A_{eff}-the effective mode area. For the particular values of the input peak power and pressure used, the maximum broadening $\delta\omega_{max}$ is approximately 90nm for Ar and 150nm for Kr which agrees reasonably well with the measured values from the spectra.

We used the WLC generated in Kr for further Z-scan experiments. The usable wavelength range was approximately 650-850nm. Unfortunately, we didn't find a commercial LVF to work for this wavelength range without beam distortion. To separate the WLC wavelengths we used narrow bandwidth filters mounted on a wheel which was attached to a computer controlled motor. As the motor rotated the wheel different narrow bandwidth filters were placed on the WLC path. Each filter transmitted a different spectral component of the WLC source. The transmitted bandwidth was approximately 10nm. Figure 5-17 shows the experimental set-up.

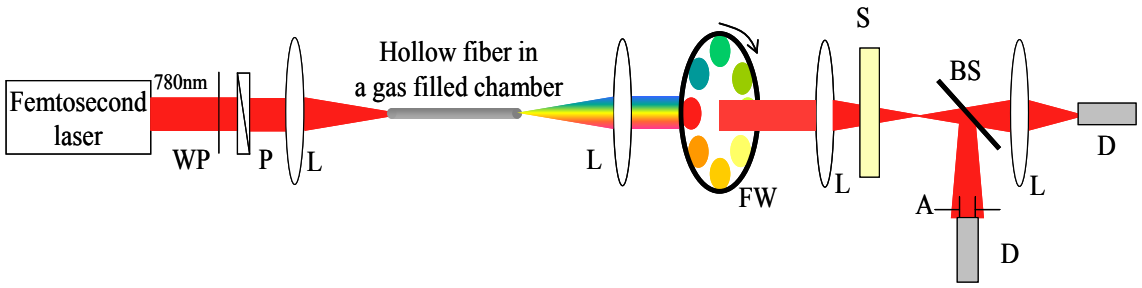

Figure 5-17: Experimental set-up for Z-scan using a WLC source: WP-waveplate; P-polarizer; A-aperture; L-lens; FW-filter wheel; S-sample; D-detector

We used a commercial Grenouille set-up [31,86] to measure the pulsewidth corresponding to each spectral component transmitted by the narrow band filter. The pulsewidths measured for different wavelengths were between 100-130fs (FWHM in irradiance). The beam waists corresponding to different wavelengths were determined by knife-edge scans. The energies for different wavelengths across the spectrum were measured and their values are shown in the graph of Fig. 5-18; they were at least two orders of magnitude larger than the ones corresponding to the wavelengths in the WLC source generated in water.

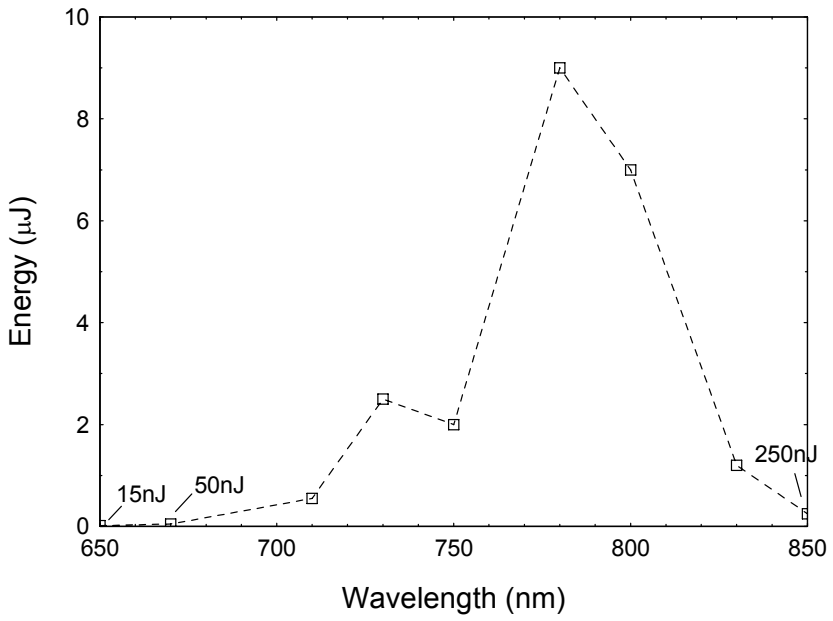

Figure 5-18: Energies for different wavelengths in the continuum measured after the corresponding narrow band filter

Beam images and their corresponding Gaussian profiles measured by a CCD for different wavelengths after the narrow band filters are shown in Fig. 5-19.

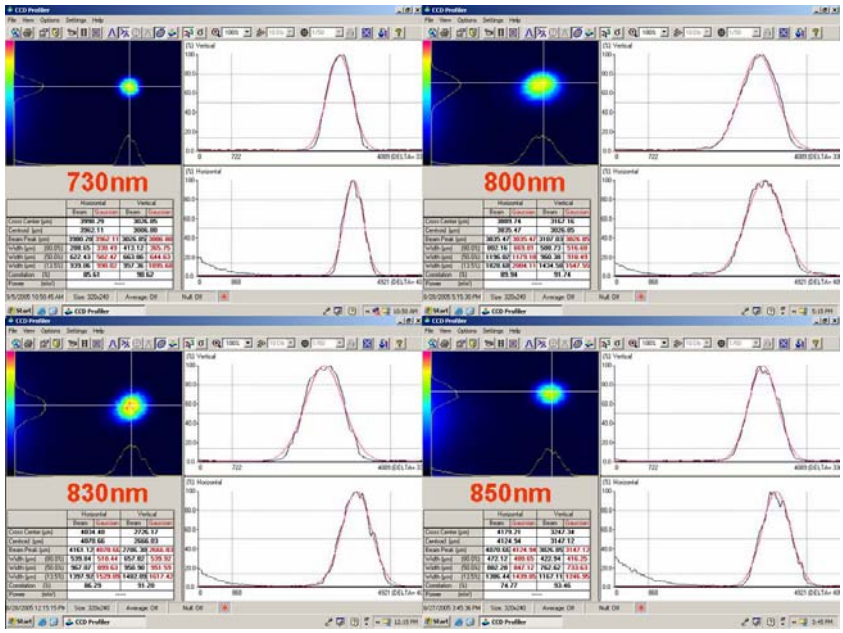

Figure 5-19: Beam images and their Gaussian profiles measured by a CCD for different wavelengths

Values of the measured 2PA coefficient β of ZnSe obtained from fits at different wavelengths are presented in Figure 5-20 along with the theoretical predictions [78].

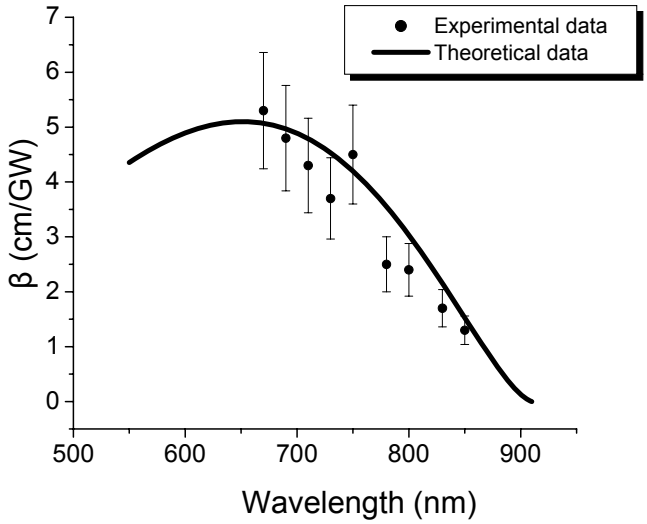

Figure 5-20: 2PA coefficients obtained from theory and from the experimental data fittings

This time, by using this experimental set-up with much larger spectral irradiance, we were able to measure the two-photon absorption cross-section of organic materials. The 2PA cross-section measured values are shown in Figure 5-21 and Figure 5-22 for two different organic dye solutions along with the values obtained by using single wavelength Z-scan [87] or two-photon fluorescence (2PF) measurements [88].

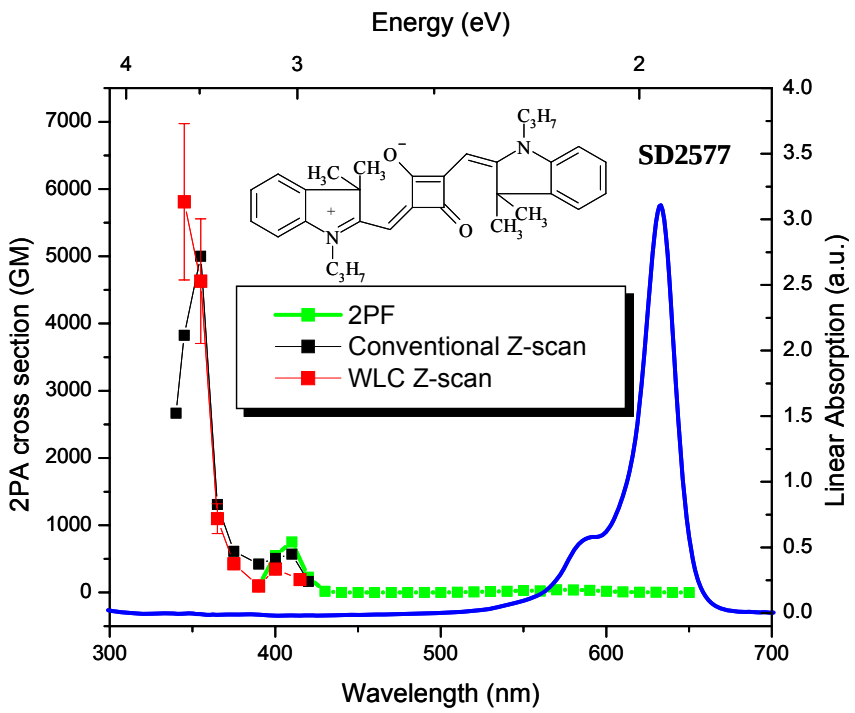

Figure 5-21: 2PA cross-section spectrum for SD2577 compound obtained from WLC Z-scan experiment and comparison with spectra obtained from Single Wavelength Z-scan and 2PF experiments

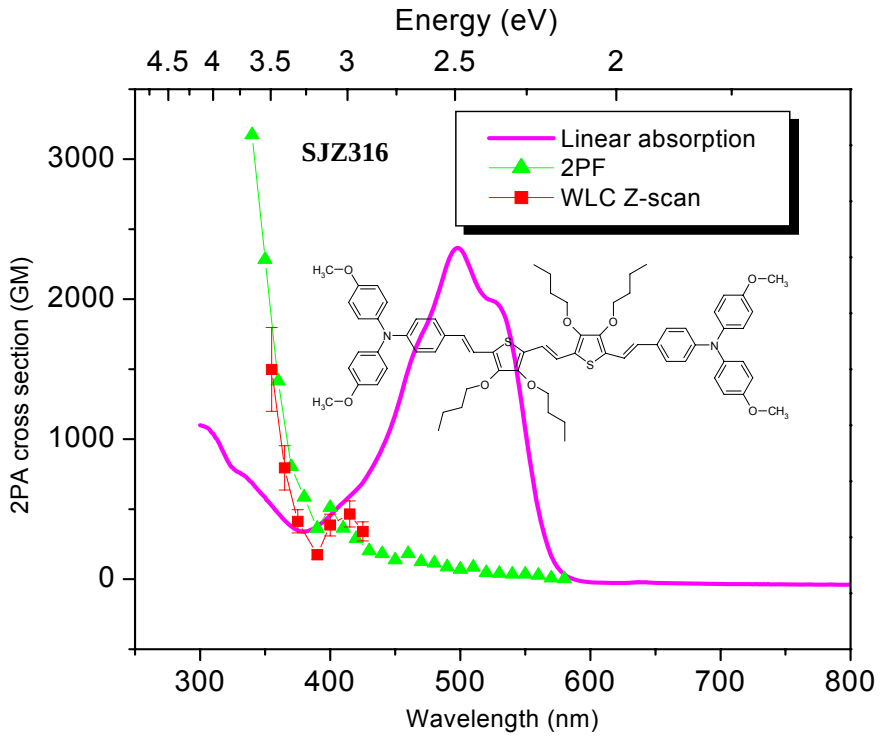

Figure 5-22: 2PA cross-section spectrum for SJZ316 compound obtained from WLC Z-scan experiment and comparison with spectra obtained from 2PF experiments

Except the discrepancy corresponding to one short wavelength for one of the organics (Fig. 5-21) which we have no explanation yet, there is, in general, a reasonable agreement between the WLC Z-scan measurements and the values predicted theoretically (ZnSe) or the values obtained by using 2PF and/or single wavelength Z-scan (organics) which illustrates the validity of the new method.

At this point our WLC source has high energy and good spatial quality but is still not as broad as we would need it to be. Reference 48 showed that broadband WLC spectra can be obtained by propagating short pulses through high pressure gas without a guiding element. We

therefore removed the hollow fiber from the chamber and let the beam propagate through the noble gas filled-chamber. The details about this experiment are presented in the next section.

5.2.3. WLC Z-scan using WLC generated in noble gases

We used our Ti:Saphire femtosecond laser to focus the 140fs, 775nm into a chamber filled with noble gas. In a first experiment, an 80 cm long stainless steel chamber and Kr gas were used. We used different focusing geometries and different gas pressures. The first observation we could make concerned the white-light continuum stability. The continuum generated using a 30cm focal length lens was very unstable, i.e. the energy fluctuated wildly from pulse to pulse as the pressure was varied between 2 and 4atm (above the atmospheric pressure). As the diffraction length was increased by increasing the focal length of the focusing lens, the continuum became more and more stable. There was a limit for the focal length used imposed by the damage threshold of the chamber windows. We used longer chambers to be able to generate continuum by using lenses with focal lengths as long as 200cm. It appears that there was a limit for the continuum stability, which we reached for the longer focal lengths, determined by the fluctuations of the input beam. From one point using a longer chamber with a longer focal length lens did not help (e.g. a 180cm long chamber and a 200 focal length lens). Besides its stability, we were interested in three other characteristics of the continuum: broadening, high energy and good quality spatial profile. We would also expect the loose focusing geometry to favor a larger spectral broadening of the continuum as the interaction length is increased [89,90]. Using the maximum of the energy available from our Ti:Sapphire

system of ~0.8 mJ, the only parameters available to adjust for optimizing the generated continuum were the type of gas, the gas pressure, the focusing geometry and the length of the pressurized chamber. The gases we used were Argon, Krypton and Xenon. We focused the 775nm laser beam into the pressurized chamber with lenses of 100cm, 150cm and 200cm focal lengths. We focused into chambers of lengths 80cm, 125cm and 180cm. We noticed the generated continuum was unstable if a long chamber would be used with a short focal length, for example, if we used the 180cm long chamber with the 100cm focusing lens (corresponding to beam waist of ~100μm, z_0=4cm). On the other hand, when a short chamber-long focusing length lens combination was used, a ring pattern was noticed in the beam profile for some of the wavelengths in the continuum. An example is shown in Fig. 5-23 and Fig. 5-24. In Fig.5-23 the final experimental configuration used is presented. Figure 5-24 shows an example of a ring pattern of the beam profile for wavelengths in the continuum when two types of gases were used.

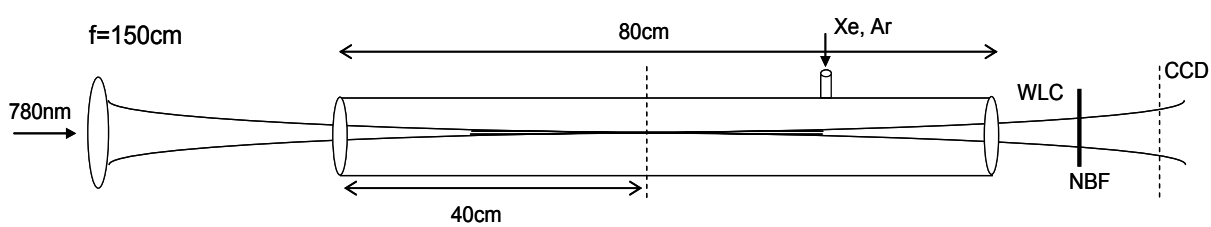

Figure 5-23: Experimental configuration used for observing ring pattern in the beam profile of wavelengths in the continuum

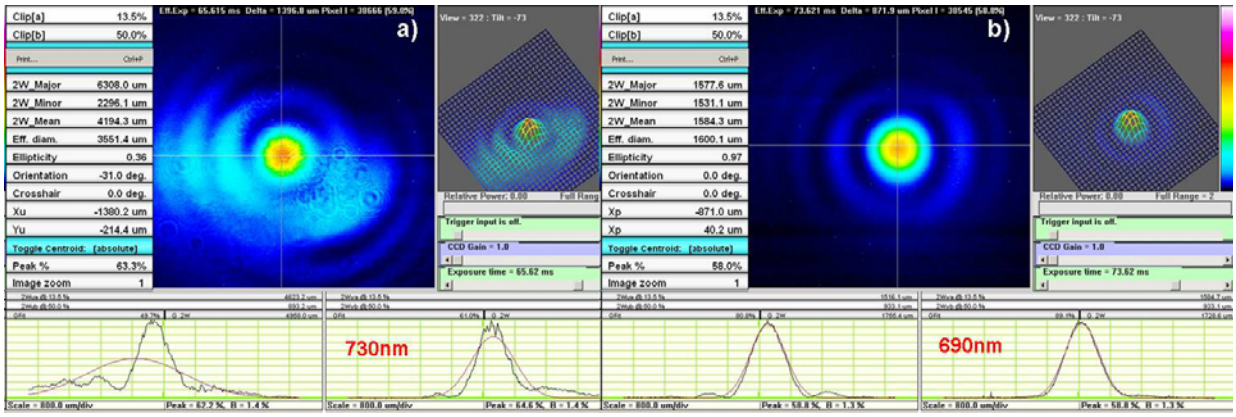

Figure 5-24: Beam profiles corresponding to wavelengths in the continuum for different gases used in the pressurized chamber a) Xe (0.35 atm); b) Ar (5.4 atm); pressures quoted are above atmospheric pressure

The configuration set-up for which we obtained the best characteristics for the continuum is depicted in Fig. 5-25. This gave us the best WLC in terms of stability, spectral width, energy density and spatial profile. The chamber used was 125cm long and the focusing length f=150cm corresponding to a beam waist of 145 μm (HW1/e^2M of intensity) and a Rayleigh range of approximately 8.5cm. The gas used was Krypton at 1.4 atm above atmospheric pressure, i.e. total pressure of 2.4 atm. Similar broadening for the continuum was obtained by using Ar and Xe instead of Kr. We preferred Kr because giving its nonlinearity a reasonable pressure was needed for a stable and broadband continuum. Ar, for example, exhibiting the lowest nonlinearity from these three gases, needed to be pressurized at approximately 5atm (above atmospheric pressure) for stable continuum generation. We were not sure our chamber windows would have withstood this pressure on a long time basis. Besides this, Kr was much less expensive than Xe.

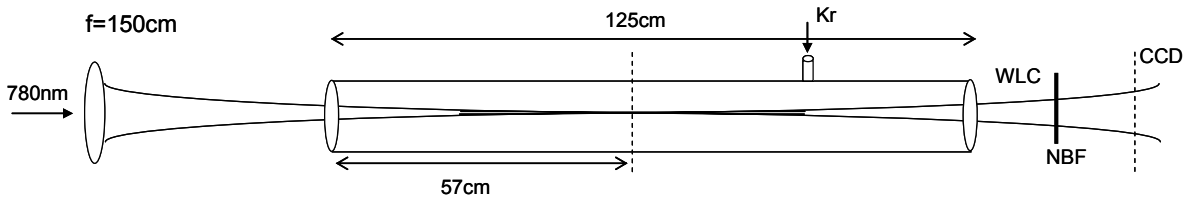

Figure 5-25: Experimental configuration used for generating a stable, high energy, broadband, good beam profile WLC source

The energy used for the 775nm beam was 710μJ which for our 145 fs (FWHM in irradiance) pulses resulted in a peak power of 4.9GW, above the critical power of 1.35GW for self-focusing in Kr at 1.4atm above atmospheric pressure (if $n_2/p=2.78\cdot10^{-23}$ $m^2/W\cdot atm$ for Kr is assumed [85]). The corresponding beam irradiance at focus was around $10^{13}GW/cm^2$.

The continuum had a white center surrounded by a ring which was reddish on one half and bluish on another half. This is not a typical appearance of the WLC beam, usually the white spot in the middle is surrounded by a single color rim giving that the beam is spatially symmetric [44]. A picture of the continuum is shown in Fig. 5-26.

Figure 5-26: White-light continuum image

The spectrum (log scale) of the continuum spectrum is presented in Fig. 5-27.

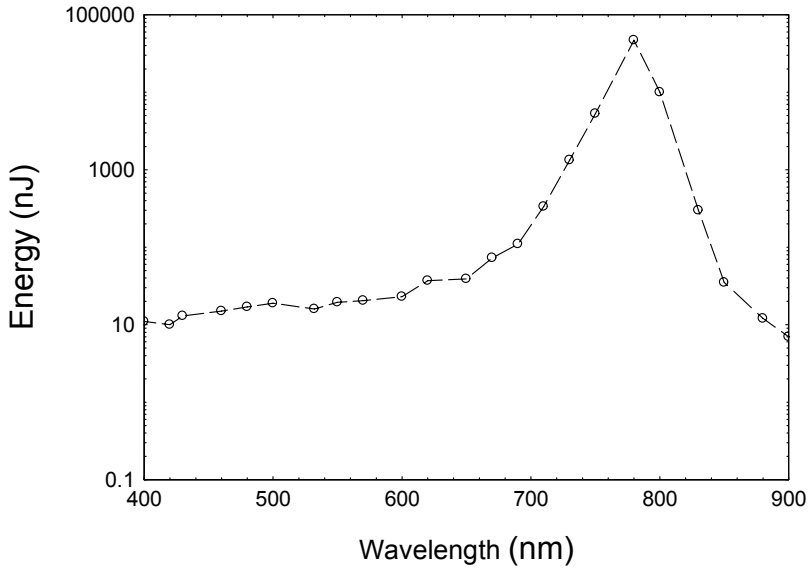

Figure 5-27: White-light continuum spectrum

The picture in Fig. 5-26 was taken outside the chamber filled with Kr gas. We discussed previously, in paragraph 5.1.3, the filamentation generated by the short pulses propagation in gases. Most probably, the filamentation conditions are created inside the chamber in our experiment as the pulses' peak power exceeds the critical peak power corresponding to self-focusing, as mentioned above and also the spectrum shown in Fig. 5-27 is comparable with the simulated ones under similar conditions used in Reference 90. Nevertheless, a detailed analysis inside the chamber could determine the nature/characteristics of the generated WLC. As far as our experiment goes, we used the WLC beam as it exited the chamber and diverged.

The continuum had a usable wavelength range of ~400nm, from 400nm to 800nm. To separate the WLC wavelengths for degenerate measurements, we used narrow bandwidth filters

(~12-15nm FWHM). We had NBFs available for each 20nm. We characterized both spatially and temporally the beams transmitted by each NBF on the range 400-800nm.

The beam images transmitted through three different narrow band filters are shown in Fig.5-28.

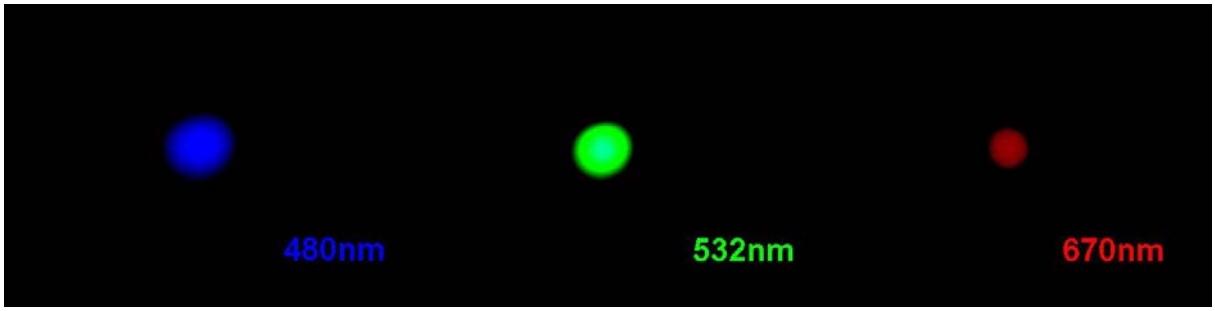

Figure 5-28: The transmitted WLC beam through three different narrow band filters

The spatial profiles for several wavelengths in the continuum are shown in Fig. 5-29. The images were taken by a CCD placed after the gas chamber.

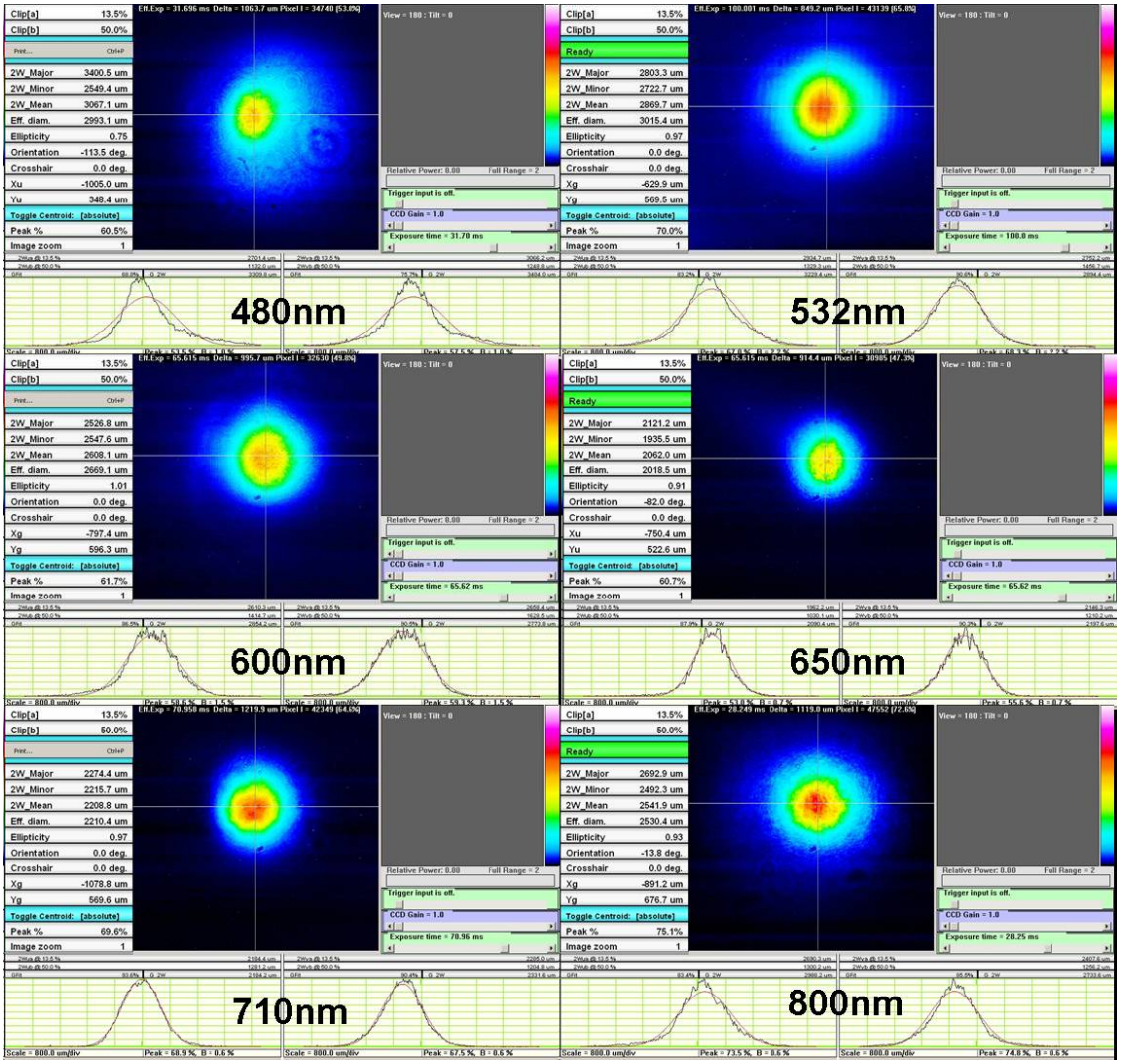

Figure 5-29: Beam profiles corresponding to different wavelengths of the continuum

Energies within ~10nm bandwidths, as obtained by transmission through the NBFs, are sufficient for NLA and NLR characterization (from a few nJ to 100's of nJs).

To determine the pulsewidth for different wavelengths transmitted by NBFs we used a commercial Grenouille set-up for the NIR wavelengths [31, 86] and an intensity autocorrelator for the visible wavelengths. For the intensity autocorrelation we used the 2PA as the nonlinear process (we used either a detector with a two-photon absorbing element, GaP, or a ZnSe sample in front of a Si detector) . The results are shown in Fig. 5-30.

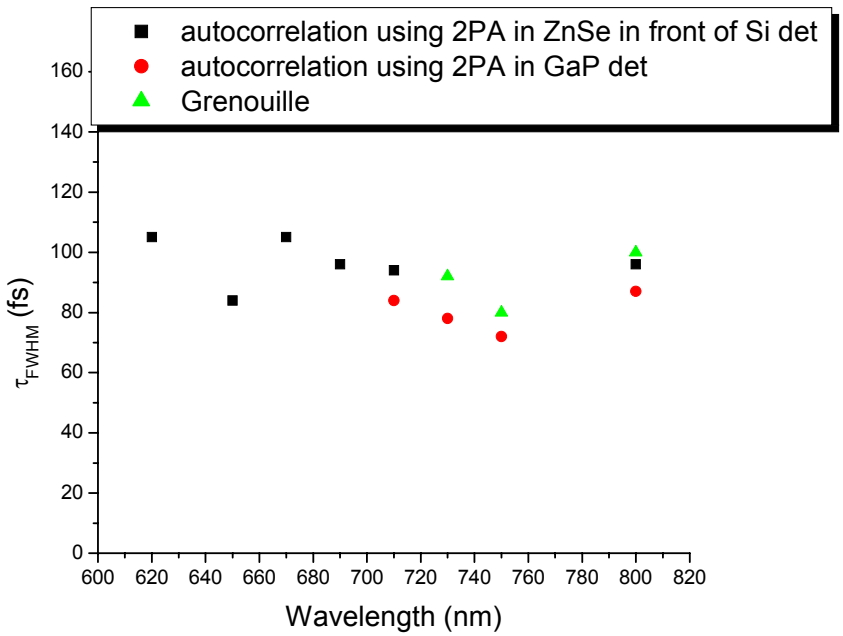

Figure 5-30: Pulsewidth measurements results for different wavelengths in the continuum transmitted by NBFs

We notice the pulsewidths have an average value around 90-100fs (FWHM in irradiance) for all the wavelengths transmitted by NBFs. This pulsewidth and its corresponding ~10nm bandwidth transmitted by the NBF, results in a time-bandwidth product around 0.44, indicating nearly transform-limited pulses.

We determined the beam waist for different wavelengths transmitted by the NBF by using the knife-edge scanning technique.

With knowledge of the energy, pulse duration and beam waist for each spectral component of the WLC source, we were able to fit the Z-scan transmission curve [18, 81] corresponding to each wavelength. Figure 5-31 shows the WLC Z-scan experimental set-up which uses the WLC described above as a source.

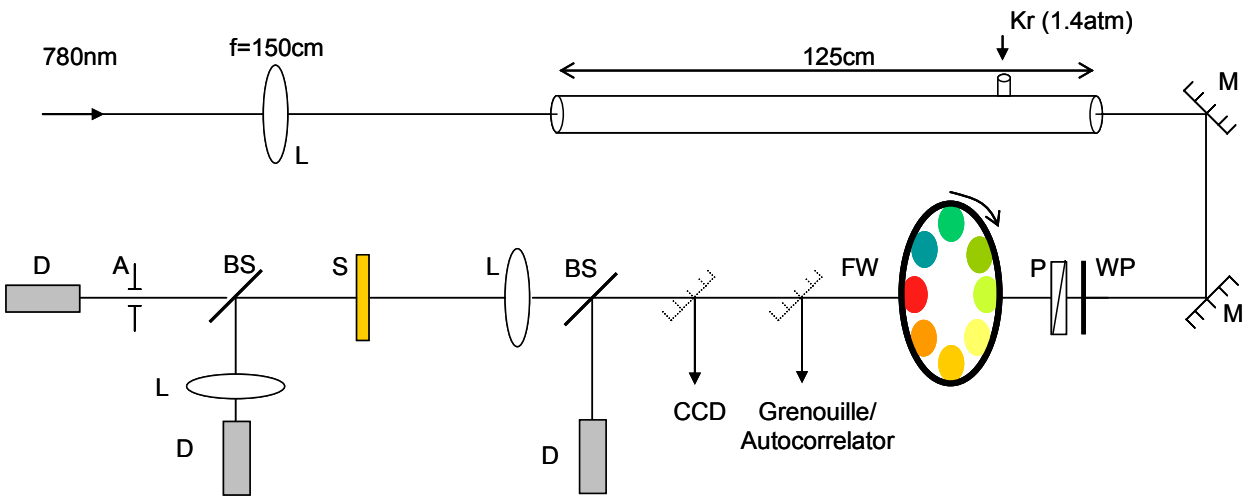

Figure 5-31: WLC Z-scan experimental set-up: L-lens; M-mirror; WP-half-waveplale; P-polorizer; FW-filter wheel; BS-beamsplitter; D-detector; A-aperture; S-sample

We used a ZnSe reference sample, to test our set-up every time we tried a different continuum source, since it is a well characterized material [18, 78, 83]. This time, besides ZnSe we used also ZnS as it has a larger bandgap (Eg=3.54eV) than ZnSe (Eg=2.7eV) which allowed us for 2PA measurements at shorter wavelengths (towards 400nm where our WLC spectrum ends). We measured the ZnSe's and ZnS' 2PA and their corresponding nonlinear refractive index

by taking data at the same time for “open” and “closed” aperture Z-scans for each spectral component transmitted by the filter wheel.

The thickness of the ZnSe sample was 0.5mm and of ZnS 1mm. An f=30cm focal length lens for focusing into the sample was used. The diffraction lengths correponding to this focusing geometry varied on a range from 1.5mm to 4mm for the wavelengths between 400nm and 800nm.

The values of z_0 for different wavelengths assured a low limit for the linear diffraction in the sample required by the “thin sample approximation” condition [18]. A low limit for the nonlinear refraction in the sample, also required by the mentioned condition, was kept by using low energies for the short wavelengths where n_2 has a large value. The thickness of the samples was also important to decide if the GVD-induced pulsewidth broadening as the pulse passes through the ZnS/ZnSe sample needed to be taken into account. It was found the pulsewidth broadening needed to be accounted for at short wavelengths (shorter than 550nm for ZnSe and shorter than 480nm for ZnS). The largest GVD-induced broadening corresponded to 480nm for ZnSe (from 100fs to 128fs) and to 400nm for ZnS (from 100fs to 123fs). 480nm and 400nm represent the shortest wavelengths measurements were done at for each of the sample.

Z-scan experimental curves for the ZnSe sample, along with their corresponding fittings [18, 81] are presented in Fig.5-32 for several wavelengths. For this sample, on the blue side of the spectrum we were limited by the linear absorption of the sample while on the red side by the continuum range.

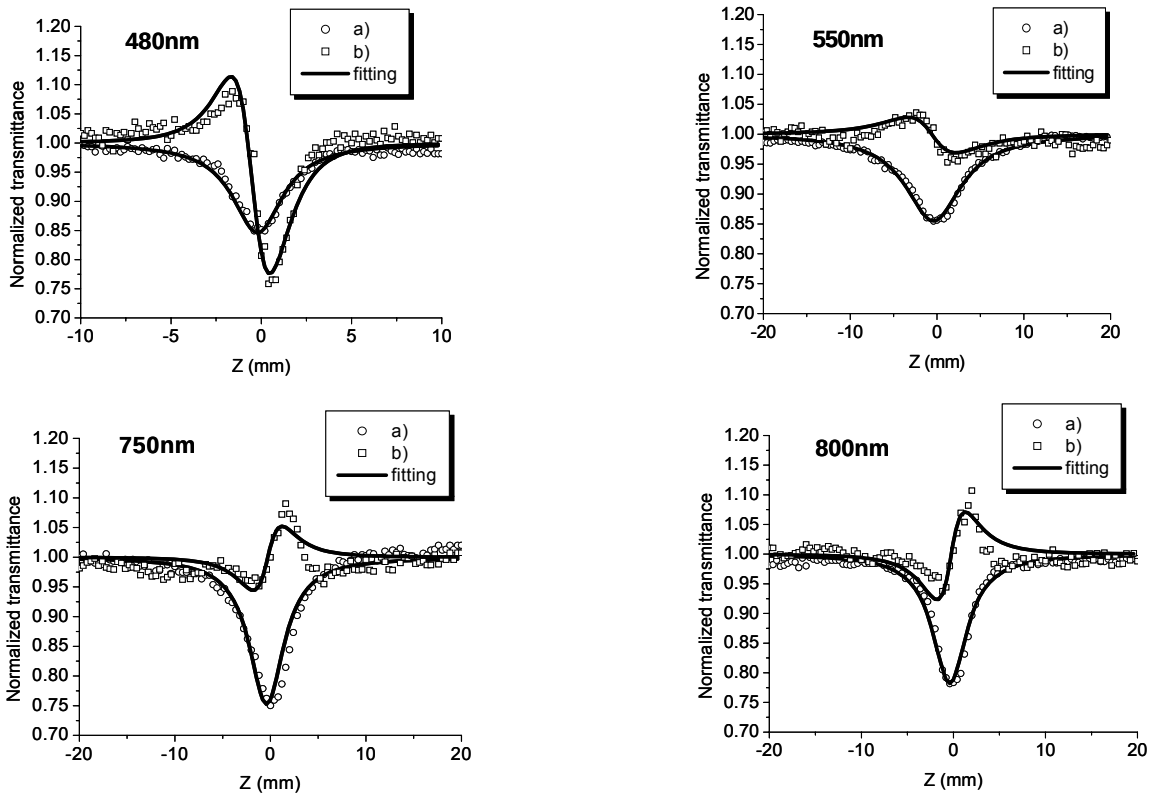

Figure 5-32: Z-scan data at 480nm, 550nm, 750nm and 800nm a) open aperture and b) closed aperture (the result of the division with open aperture)

The values of β and n_2 corresponding to ZnSe obtained from fits at different wavelengths are presented in Fig. 5-33 along with the theoretical predictions of references 78 and 83.

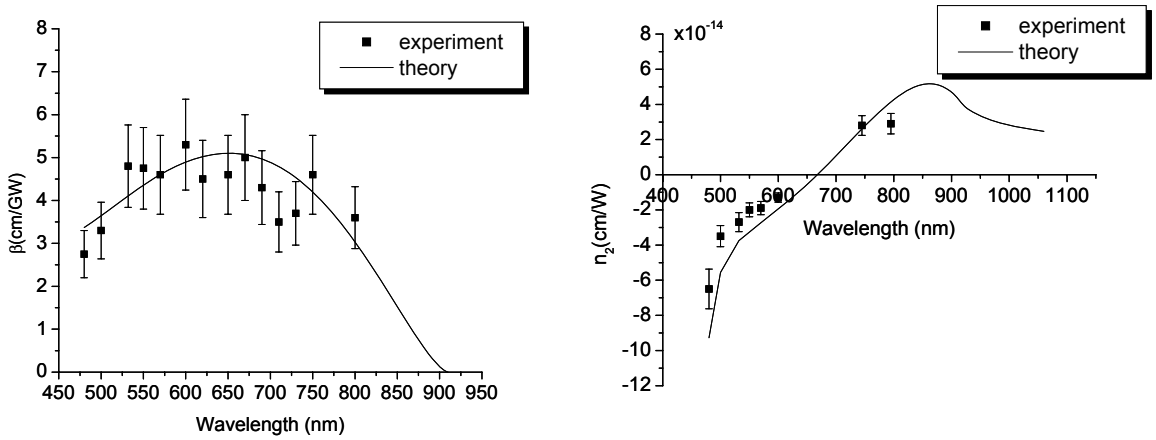

Figure 5-33: 2PA and n_2 coefficients of ZnSe obtained from theory and from the experimental data fitting

As mentioned above, we chose to measure a larger bandgap semiconductor also which allows us 2PA and n_2 measurements over the whole spectrum (400nm-800nm) of the continuum. Z-scan experimental curves for the ZnS sample, along with their corresponding fittings [18, 81] are presented in Fig.5-34 for several wavelengths.

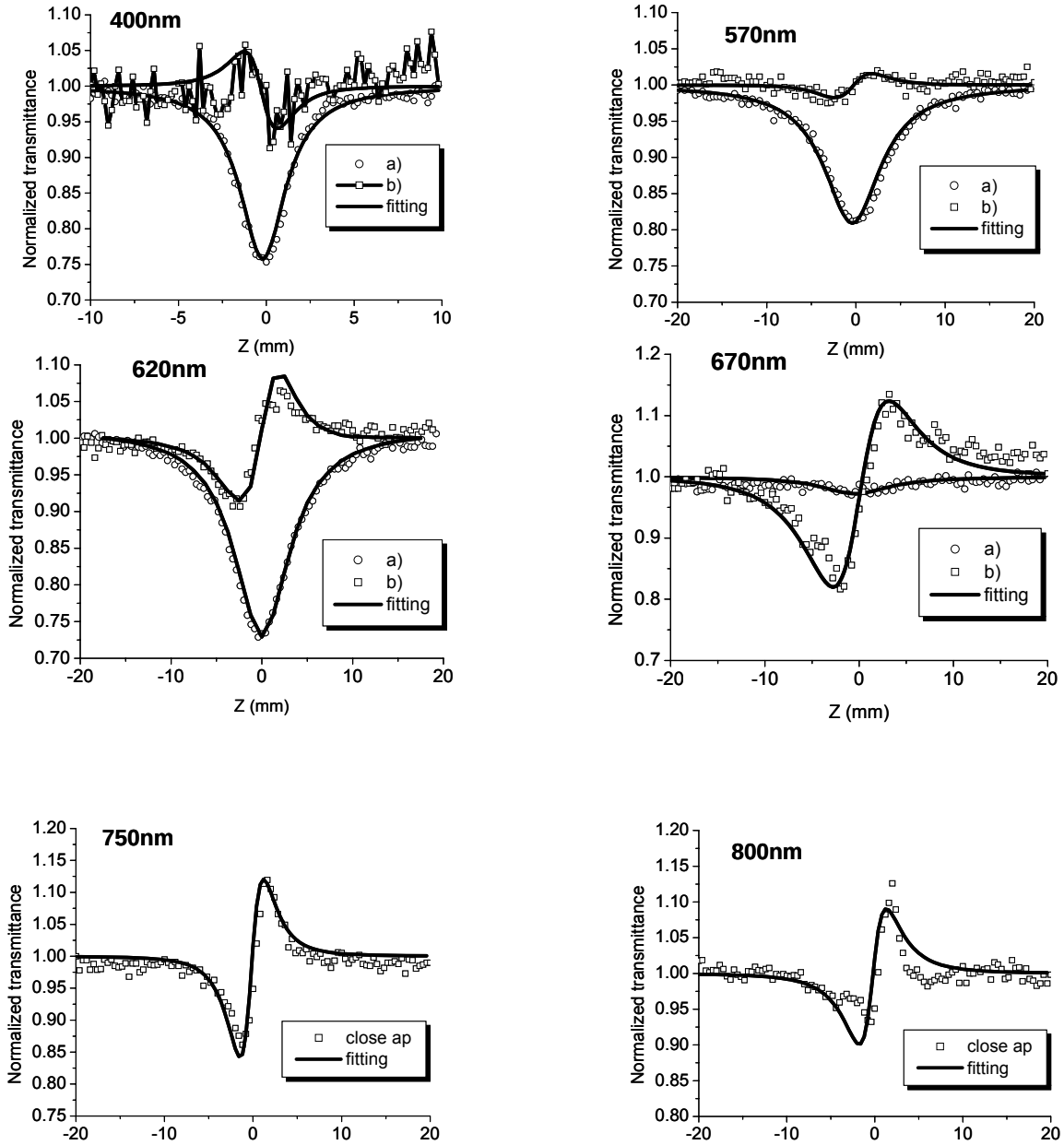

Figure 5-34: Z-scan data at 400nm, 570nm, 620nm, 670nm, 750nm and 800nm a) open aperture b) close aperture (the result of the division with open aperture). The last two graphs do not show open aperture curves as 2PA was not present at those particular wavelengths

The values of β and n_2 corresponding to ZnS obtained from fits at different wavelengths are compared with the theoretical predictions of references 78 and 83 and presented in Fig. 5-35.

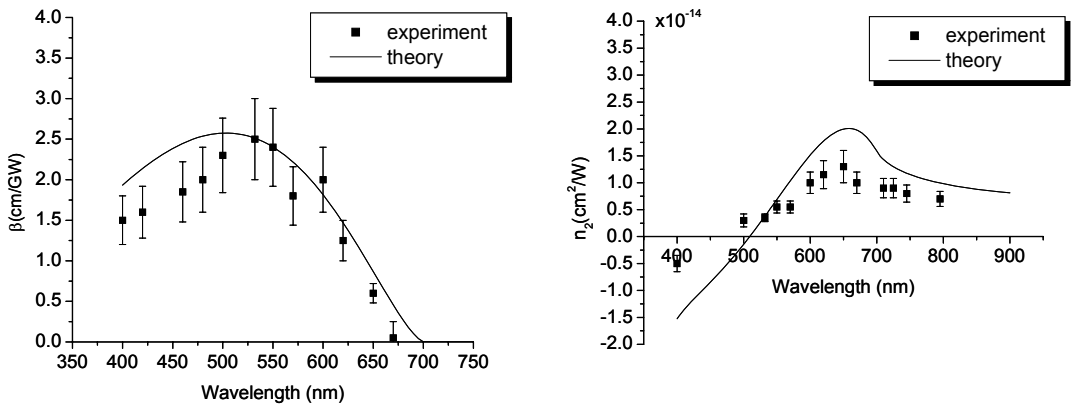

Figure 5-35: 2PA and n_2 coefficients of ZnS obtained from theory and from the experimental data fitting

We notice a reasonable agreement between experimental results and theoretical calculations for the 2PA spectrum and n_2 dispersion [18,78,82] corresponding to both ZnSe and ZnS as showed in Figures 5-33 and 5-35 above, attesting to the potential of this technique.

CHAPTER 6: CONCLUSION

6.1. Summary

In this dissertation, WLC pump-probe and Z-scan techniques were used to measure the peak 2PA cross-sections for a number of commercially available photoinitiators. The results of the two methods agree within experimental error. It is expected that the field of two-photon absorbing photopolymerization and microfabrication will benefit from new photoinitiators that exhibit high 2PA.

The main goal of this dissertation was to introduce and demonstrate a sensitive method for rapid characterization of a material's degenerate nonlinear absorption spectrum and the dispersion of its nonlinear refraction: WLC Z-scan. In this technique, the single wavelength in a typical Z-scan experiment was replaced by a WLC source. It was shown there were two important requirements regarding this technique:

1) Minimization of nondegenerate nonlinear effects due to the spatial and partially temporal overlap of different wavelengths in the WLC source
2) Generation of an intense, stable, good spatial quality, broadband WLC

The first requirement was fulfilled by using different dispersive elements for minimizing the nondegenerate nonlinear effects. First, a glass prism for spatial dispersion and a thick GVD material for temporal dispersion were used. Then, the spectral separation by using a linear variable filter or a filter wheel with narrow band filters was found to be more convenient for our experiments.

Different transparent media were used for WLC generation in an effort to meet the second requirement.

The advantages and disadvantages of WLC generated in different nonlinear media and also a review of different mechanisms proposed so far in the literature to explain the WLC generation were presented.

The WLC generated in distilled water was broad, stable, had good spatial quality but the low spectral energy densities would not allow for measuring samples with low nonlinearities (e.g. low concentration organic solutions). An increase of the incident beam energy above a certain threshold would cause the WLC beam to break into filaments which makes it impossible to be used in a Z-scan experiment. The filamentation is due to self-focusing balanced by plasma generation once the multiphoton ionization threshold has been reached. The multiphoton ionization threshold and the critical power corresponding to self-focusing are much larger for noble gases than for solids/liquids [91]. This allows a higher energy to be used for single filament WLC generation in a gas than in a solid/liquid medium. Therefore, we tried to increase the spectral energy densities corresponding to our WLC source by using a gas as the nonlinear medium for WLC generation. The WLC generated in a noble gas-filled hollow fiber was stable, having good spatial quality, high energy but only ~200nm broad. Finally, we removed the hollow fiber and generated WLC by loosely focusing the input beam in a stainless-steel chamber filled with a noble gas. Different focusing geometries, chamber lengths, gases and gas pressures were used. The best result was obtained by focusing the 145fs, 775nm from our Ti:sapphire laser down to 145μm into a 125cm long chamber filled with ~2.5atm of Kr. The resulting WLC single filament beam was stable, had good spatial quality, high energy and approximately had ~400nm bandwidth (from 400 to 800nm).

We experimentally verified the method on the well-characterized semiconductors ZnSe and ZnS. The good agreement between experimental results and theoretical calculations for the 2PA spectrum and n_2 dispersion attests to the potential of this technique. We also showed the method can be used for materials exhibiting lower nonlinearities than semiconductors (i.e. organic solutions).

The new technique introduced in this dissertation opens the way for rapid nonlinear material characterization. We expect this nonlinear spectrometer to be a beneficial tool for samples' rapid characterization required by the projects our lab is involved in.

6.2. Future Work

Rick Trebino says in his "FROG" book: "The first goal in developing a measurement technique is to make it work. Once that's done, the next step is to make it simple." [31]. There are still ways to simplify/improve our WLC Z-scan technique:

1) A complete automatization (which would imply a single pushed button for recording a nonlinear absorption/refraction spectrum) is now difficult to realize as the energy in the WLC source is lower for short wavelengths than for longer ones (almost 3 orders of magnitude) while the NBFs have approximately the same transmission for all the wavelengths in the WLC. This requires energy adjustments for different wavelengths during the experiment. Designing a spectral filter with higher transmission for shorter wavelengths than for longer ones would assure the same order of magnitude energies for different wavelengths. This way the entire spectrum would be able to be measured without need to increase/decrease the energy for different wavelengths during the experiment.

2) The usable wavelength range for our WLC Z-scan is 400nm-800nm. Extension of the WLC spectrum in the IR region would be desirable. Increasing the pump energy for the WLC generation might slightly broaden the WLC spectrum but would result in beam filamentation too, which, as we discussed in the previous chapter, is not convenient for our experiments. Recently, a circular phase mask has been used to control the WLC broadening while still keeping the single filament regime [92]. Similarly, we tried to add chirp on the pump pulse to check on how the variation of the temporal phase affects the broadening of the WLC. We were able to quickly check this in Dr. Richardson's lab whose facilities include a Ti:Sapphire laser (2mJ/pulse, 1kHz, 40fs) and a pulse shaper (Dazzler) [93] which allows for temporal phase variation. We noticed an extension of the WLC spectrum towards the IR when chirp was added to the pump pulse. Therefore, future research work should involve attempts of modifying the temporal phase pump pulse for obtaining a larger broadening of the WLC source.

Besides the experimental improvements, a better understanding of the continuum generation by femtosecond pulse propagation through gases would be also desirable. We already sent several images corresponding to different wavelengths in our WLC source to Dr. Wright's group at the University of Arizona to be used as a comparison with their theoretical modeling of the continuum generation in gases.

LIST OF REFERENCES

[1] R. W. Boyd, "Nonlinear Optics", *Academic Press*, 2nd edition, 2003

[2] T. H Maiman, "Stimulated optical radiation in ruby", *Nature*, Vol. 187, 493 (1960)

[3] P. A. Franken, A. E. Hill, C. W. Peters, and G. Weinreich, "Generation of optical harmonics", *Phys. Rev. Lett.*, Vol. 7, 118 (1961).

[4] W. Kaiser, C. G. B. Garrett, "Two-photon excitation in CaF_2:Eu^{2+}", *Phys. Rev. Lett.*, Vol. 7, 229 (1961).

[5] M. Göppert-Mayer, "Uber Elementarakte mit zwei Quantensprungen (About elementary events with two quantum jumps)", *Ann. Physik*, Vol. 9, 273 (1931).

[6] E. W. Van Stryland and D. J. Hagan, "Nonlinear absorption", *Encyclopedia of Optical Engineering,* 1475-1481 (2003).

[7] W.Denk, J.H. Strickler and W.W. Webb, "Two-photon laser scanning fluorescence microscopy", Science, Vol. 248, 73 (1990).

[8] P.T.C So, C. Y. Dong, B. R. Masters and K. M. Berland, "Two-photon excitation fluorescence microscopy", *Annual Review of Biomedical Engineering*, Vol. 2, 399 (2000).

[9] S. Maruo, O. Nakamura and S. Kawata, "Three-dimensional microfabrication with two-photon-absorbed photopolymerization", *Opt. Lett.,* Vol. 22, 132-135 (1997).

[10] K. D. Belfield, X.Ren, D. J. Hagan, E. W. Van Stryland, V. Dubikovsky, E. J. Miesak, "Microfabrication via two-photon photoinitiated polymerization", *Abstr. Papers Amer. Chem. Soc.,* Vol. 218 (2001).

[11] J. H. Strickler and W. W. Webb, "Three-dimensional optical data storage in refractive media by two-photon point excitation", Opt. Lett., Vol. 16, 1780 (1991).

[12] E. W. Van Stryland, Y. Y. Wu, D. J. Hagan, M. J. Soileau, K. Mansour, "Optical limiting with semiconductors", *JOSA B*, Vol. 5 1980 (1988).

[13] G. S. He, H. L. Song and K S Ho, *Physics of Nonlinear Optics*, World Scientific Pub Co Inc, (200).

[14] P. Delfyett, "High Speed Photonics" class notes (2005)

[15] A. Samoc, M. Samoc, M. Woodruff and B. Luther-Davies, "Tunning the properties of poly (p-phenylenevinylene) for use in all-optical switching", Opt. Lett., Vol. 20, 1241-1243 (1995).

[16] C. Tai, J. Wilkinson, N. Perney, M. Netti, F. Cttaneo, C. Finlayson and J. Baumberg, "Determination of nonlinear refractive index in a Ta_2O_5 rib waveguide using self-pahse modulation", *Opt. Express*, Vol. 12, 5110 (2004).

[17] R. Negres, J. Hales, A. Kobyakov, D. J. Hagan, E. W. Van Stryland, "Experiment and Analysis of Two-photon Absorption Spectroscopy Using a White-Light Continuum Probe", *IEEE Journal of Quantum Electronic*s, Vol. 38, 1205 (2002).

[18] M. Sheik-Bahae, A. A. Said, T. H. Wei, D. J. Hagan, E. W. Van Stryland, "Sensitive Measurement of Optical Nonlinearities Using a Single Beam", *IEEE Journal of Quantum Electronics*, Vol. 26, 760 (1990).

[19] D. J. Hagan, "Optical properties of materials", *class notes,* (2001).

[20] D. J. Hagan, "Fundamentals of Optical Science", *class notes,* (2003).

[21] Y. R. Shen, *The principles of nonlinear optics*, John Wiley & Sons, New York, (1984).

[22] G. Stegeman, "Nonlinear Optics", *class notes,* (2002).

[23] A. A. Said, C. Wamsley, D. J. Hagan, E. W. Van Stryland, B. A. Reinhardt, P. Roderer and A. G. Dillard, "Third- and fifth- order optical nonlinearities in organic materials", Chem. Phys. Lett., Vol. 228, 646 (1994).

[24] A. A. Said, M. Sheik-Bahae, D. J. Hagan, T. H. Wei, J. Wang, J. Young and E W. Van Stryland, "Determination of bound-electronic and free-carrier nonlinearities in ZnSe, GaAs, CdTe and ZnTe", J. Opt. Soc. Am B, Vol. 9, 405 (1992).

[25] D. C. Hutchings, M. Sheik-Bahae, D. J. Hagan, and E. W. Van Stryland, "Kramers-Kronig relations in Nonlinear Optics," *Optical and Quantum Electronics,* vol. 24, 1-30, (1992).

[26] M. A. Woodall, "Nonlinear absorption techniques and measurements in semiconductors", *PhD Dissertation*, North Texas State University, 1985.

[27] M. Cha, "Third order nonlinear optical spectroscopy of organic materials", *PhD Dissertation*, University of Central Florida, 1994.

[28] D. Strickland and G. Mourou, "Compression of amplified chirped optical pulses", Opt. Commun., 56, 219 (1985).

[29] K. R. Tamura, E. P. Ippen, H. A. Haus, L. E. Nelson and C. R. Doerr, "Stretched-pulse fiber laser", *U.S. Patent*, No. 5,617,434 (1997).

[30] W. T. Silfvast, "Laser Fundamentals", *Cambridge University Press*, (1996).

[31] R. Trebino, "Frequency resolved optical gating: The measurement of ultrashort laser pulses", *Kluwer Academic Publishers* (2000).

[32] R. Negres, "Ultrafast nonlinear spectrometer for nonlinear material characterization" *PhD Dissertation*, University of Central Florida, Orlando, Fl, (2001).

[33] http://www.physics.gatech.edu/gcuo/UltrafastOptics/index.html#8803 (R. Trebino class website)

[34] H. Kogelnik and T. Li, "Laser beams and resonators", *Appl. Opt.,* Vol. 5, 1550 (1966)

[35] F. Yoshino, "Multiphoton effects in the polydiacetylene poly bis(p-toluenesulfonate) of 2,4-hexadiyne-1,6-diol (PTS) ", *PhD Dissertation*, University of Central Florida, Orlando, Fl, (2003); F. E. Hernandez et al., "Three- and four-photon absorption of a multiphoton absorbing fluorescent probe", *Appl. Opt.,* Vol. 43, 5394 (2004)

[36] M. Sheik-Bahae, A. A. Said, D. J. Hagan, M. J. Soileau and E. W. Van Stryland, "Nonlinear refraction and optical limiting in thick media", *Optical Engineering*, Vol. 30, 1228 (1991).

[37] D. Weaire, B. S. Wherrett, D. A. B. Miller and D. Smith, "Effect of low-power nonlinear refraction on laser-beam propagation in InSb", *Opt. Lett.,* Vol. 4, 331 (1979).

[38] Matlab code written by Claudiu Cirloganu

[39] K. J. Schafer, J. M. Hales, M. Balu, K. D. Belfield, E. W. Van Stryland and D. J. Hagan, "Two-photon absorption cross-sections of common photoinitiators", *Journal of Photochemistry and Photobiology A: Chemistry*, 162:2-3:497-502 (2004).

[40] W.H. Zhou, S.M. Kuebler, K.L. Braun, T.Y. Yu, J.K. Cammack, C.K. Ober, J.W. Perry, S.R. Marder, *Science,* Vol 296, 1106 (2002).

[41] K. D. Belfield, K.J. Schafer, Y.U. Liu, J. Liu, X.B. Ren, E.W. Van Stryland, "Multiphoton-absorbing organic materials for microfabrication, emerging optical applications and non-destructive three-dimensional imaging", *J. Phys. Org. Chem.,* Vol 13, 837 (2000).

[42] K. D. Belfield, X.B. Ren, E.W. Van Stryland, D.J. Hagan, V. Dubikovsky, E.J. Miesak, "Near-IR Two-Photon Photoinitiated Polymerization Using a Fluorene/Amine Initiating System", *J. Am. Chem. Soc.,* Vol. 122, 1217(2000).

[43] R. R. Alfano and S. L. Shapiro, "Emission in the region 4000 and 7000 Å via four-photon coupling in glass", *Phys. Rev. Lett.*, Vol. 24, 584-587 (1970).

[44] A. Brodeur and S. L. Chin, "Beam filamentation and the white-light continuum divergence", *Opt. Comm.,* Vol. 129, 193-198 (1996).

[45] G. S. He, T. C. Lin, P. N. Prasad, R. Kannan, R. A. Vaia and L. S. Tan, " New technique for degenerate two-photon absorption spectral measurements using femtosecond continuum generation" *Opt. Express,* Vol. 10, 566 (2002).

[46] L. De Boni, A. A. Andrade, L. Misoguti, C. R. Mendoca and S. C. Zilio, "Z-scan measurements using femtosecond continuum generation," *Opt. Express,* Vol. 12, 3921 (2004).

[47] R. L. Fork, C. V. Shank, C. Hirlimann and R. Yen, "Femtosecond white-light continuum pulses", *Opt. Lett.,* Vol. 8, 1-3 (1983).

[48] P. B. Corkum and C. Rolland, "Supercontinuum generation in gases", *Phys. Rev. Lett.,* Vol. 57, 2268-2271 (1986).

[49] R. H. Stolen and C. Lin, "Self-phase-modulation in silica optical fibers", Phys. Rev. A, Vol. 17, 1448-1453 (1978)

[50] M Nisoli, S. D. Sivestri and O. Svelto, "Generation of high energy 10fs pulses by a new pulse compression technique", *Appl. Phys. Lett.,* Vol. 68, 2793 (1996).

[51] R. R. Alfano and S. L. Shapiro, "Observation of self-phase modulation and small-scale filaments in crystal and glasses", *Phys. Rev. Lett.*, Vol. 24, 592-594 (1970).

[52] N. Bloembergen, "The influence of electron plasma formation on superbroadening in light filaments", *Opt. Commun.,* Vol. 8, 285-288 (1973).

[53] G. Yang and Y. R. Shen, "Spectral broadening of ultrashort pulses in a nonlinear medium", *Opt. Lett.,* Vol.9, 510-512 (1984).

[54] G. S. He, G. C. Xu, Y. Cui and P. N. Prasad, "Difference of spectral superbroadening behavior in Kerr-type and non-Kerr-type liquids pumped with ultrashort laser pulses", *Appl. Opt.,* Vol.32, 4507-4512 (1993).

[55] A. Brodeur and S. L. Chin, "Ultrafast white-light continuum generation and self-focusing in transparent condensed media", *J. Opt. Soc. Am. B,* Vol. 16, 637-650 (1999).

[56] S. L. Chin, S. A. Hosseini, W. Liu, Q. Luo, F. Théberge, N. Aközbek, A. Becker, V. P. Kandidov, O. G. Kosareva and H. Schroeder, "The propagation of powerful femtosecond laser pulses in optical media: physics, applications and new challenges", *Can. J. Phys.*, Vol. 83, 863-905 (2005).

[57] P. Chernev and V. Petrov, "Self-focusing of light pulses in the presence of normal group-velocity dispersion", *Opt. Lett.,* Vol. 17, 172-174 (1992).

[58] J. Rothenberg, "Pulse splitting during self-focusing in normally dispersive media", *Opt. Lett.,* Vol. 17, 583-585 (1992).

[59] M. K. Reed, M. K. Steiner-Shepard and D. K. Negus, "Widely tunable femtosecond optical parametric amplifier at 250 kHz with a Ti:sapphire regenerative amplifier", *Opt. Lett.,* Vol. 19, 1855-1857 (1994).

[60] K. Sokolowski-Tinten, K. Werner, M. Zhou and D. Von Der Linde, "Femtosecond continuum generation using a gas-filled hollow fiber", CLEO Conference, Baltimore, May 23-28, (1999).

[61] B. Schenkel, " Supercontinuum generation and compression" PhD Dissertation, Swiss Federal Institute of Technology Zurich, 2004.

[62] R. L. Abrams, "Coupling losses in hollow waveguide laser resonators", *IEEE J.Quan.Elec.,* Vol.QE-8, No.11, 838-843 (1972).

[63] G. Tempea and T. Brabec, "Theory of self-focusing in a hollow waveguide", *Opt. Lett.,* Vol. 23, 762-764 (1998).

[64] C. Vozzi, M. Nisoli, G. Sansone, S. Stagira and S. De Silvestri, "Optimal spectral broadening in hollow-fiber compressor systems", *Appl. Phys. B,* Vol. 80, 285-289 (2005).

[65] G. P. Agrawal, Nonlinear Fiber Optics, Academic, San Diego, 1995.

[66] R. Y. Chiao, E. Garmire and C. H. Townes, "Self-trapping of optical beams", *Phys. Rev. Lett.,* Vol. 13, 479-482 (1964).

[67] M. M. T. Loy and Y. R. Shen, "Study of self-focusing and small-scale filaments of light in nonlinear media", *IEEE J.Quan.Elec.,* Vol.QE-9, No.3, 409-422 (1973).

[68] A. Braun, G. Korn, X. Liu, D. Du, J. Squier and G. Mourou, "Self-channeling of femtosecond laser pulses in air", *Opt. Lett.,* Vol. 20, 73-75 (1995).

[69] H. R. Lange, G. Grillon, J.-F. Ripoche, M. A. Franco, B. Lamouroux, B. S. Prade and A. Mysyrowicz, "Anomalous long-range propagation of femtosecond laser pulses through air: moving focus or pulse self-guiding?", *Opt. Lett.,* Vol. 23, 120-122 (1998).

[70] P. B. Corkum and C. Rolland, "Femtosecond continua produced in gases", *IEEE J.Quan.Elec.,* Vol.25, No.12, 2634-2639 (1989).

[71] R. Rankin, C. E. Capjack, N. H. Burnett and P. B. Corkum, "Refraction effects associated with multiphoton ionization and ultrashort-pulse laser propagation in plasma waveguides", *Opt. Lett.,* Vol.16, 835-837 (1991).

[72] A. Brodeur, C. Y. Chien, F. A. Ilkov and S. L. Chin, "Moving focus in the propagation of ultrashort laser pulses in air", *Opt. Lett.,* Vol.22, 304-306 (1997).

[73] M. Mlejnek, E. M. Wright and J. V. Moloney, "Dynamic spatial replenishment of femtosecond pulses propagating in air", *Opt. Lett.,* Vol.23, 382-384 (1998).

[74] W.Liu, J.-F. Gravel, F.Théberge, A. Becker and S. L. Chin, "Background reservoir: its crucial role for long-distance propagation of femtosecond laser pulses in air", *Appl. Phys. B.,* Vol.80, 857-860 (2005).

[75] M. Rodriguez, R. Bourayou, G. Méjean, J. Ksparian, J. Yu, E. Salmon, A. Scholz, B. Stecklum, J. Eislöffel, U. Laux, A. P. Hatzes, R. Sauerbrey, L. Wöste and J. P. Wolf, "Kilometer-range nonlinear propagation of femtosecond laser pulses", *Phys. Rev. E,* Vol. 69, 036607 (2004).

[76] M.Balu, J.Hales, D.J.Hagan, E.W. Van Stryland, "White-light continuum Z-scan technique for nonlinear material characterization," *Opt. Expres.* Vol. 12, 3820 (2004).

[77] S. Yamaguchi and H. Hamaguchi, "Convenient method of measuring the chirp structure of femtosecond white-light continuum pulses," *Appl. Spectrosc.,* Vol. 49**,** 1513 (1995).

[78] E.W.Van Stryland, M.A. Woodall, H.Vanherzeele and M.J.Soileau, "Energy band-gap dependence of two-photon absorption", *Opt. Lett.,* Vol.10, 490 (1985).

[79] M.Balu, J.Hales, D.J.Hagan, E.W. Van Stryland, "Dispersion of nonlinear refraction and two-photon absorption using a white-light continuum Z-scan", Opt. Express, Vol. 13, 3594 (2005)

[80] http://www.oceanoptics.com/Products/linearvariablefilters.asp

[81] M.Sheik-Bahae, A.A.Said and E.W. Van Stryland, "High-sensitivity, single-beam n2 measurements," *Opt.Lett.,* 14, 955 (1989).

[82] D. McMorrow, W. T. Lotshaw and G. A. Kenney-Wallace, "Femtosecond optical Kerr studies on the origin of nonlinear response in simple liquids", *IEEE J.Quantum Electron.,* Vol. 24, 443 (1988).

[83] M.Sheik-Bahae, D.C.Hutchings, D.J.Hagan, E.W.Van Stryland, "Dispersion of bound electronic nonlinear refraction in solids," *IEEE J.Quantum Electron.,* Vol. 27, 1296 (1991).

[84] A. K. Dharmadhikari, F. A. Rajgara, N. C. S. Reddy, A. S. Sandhu and D. Mathur, "Highly efficient white light generation from barium fluoride" *Opt. Express,* Vol. 12, 695-700 (2004).

[85] H.J. Lehmeier, W. Leupacher and A. Penzkofer, "Nonresonant third order hyperpolarizability of rare gases and N_2 determined by third harmonic generation", *Opt. Commun.,* Vol. 56, 67 (1985).

[86] P. O'Shea, M. Kimmel, X. Gu and R. Trebino, "Highly simplified device for ultrashort-pulse measurement", *Op. Lett.* Vol. 26 932-934 (2001)

[87] Measurements performed by Lazaro Padhila in our group.

[88] Measurements performed by Jie Fu in our group.

[89] J. Ashcom, C. Schaffer, R. Gattass and E. Mazur, "Numerical aperture dependence of damage and white light generation from femtosecond laser pulses in bulk fused silica", *JOSA B* (2006), to be published.

[90] M. Kolesik, E. M. Wright, A. Becker and J. V. Moloney, "Simulation of third-harmonic and supercontinuum generation for femtosecond pulses in air" *Appl.Phys.B,* (2006), to be published.

[91] B. Schenkel, "Supercontinuum generation and compression", *PhD Dissertation,* Swiss Federal Institute of Technology Zürich (2004)

[92] T. Pfeifer, L. Gallmann, M. J. Abel, D. M. Neumark and S. R. Leone, "Circular phase mask for control and stabilization of single optical filaments", *Opt. Lett*., to be published (also presented at CLEO conference Long Beach, CA, 2006)

[93] C. Vicario, A. Ghigo, M. Petrarca, I. Boscolo, S. Cialdi, A. Flacco, M. Nisoli, G. Sansone, S. Stagira and C. Vozzi, "Laser temporal pulse shaping experiment for SPARC photoinjector", *Proceedings of EPAC*, Lucerne, Switzerland (2004)